ABSTRACT

Title of dissertation: DEGENERATE MIXTURES OF RUBIDIUM
                                      AND YTTERBIUM FOR ENGINEERING
                                      OPEN QUANTUM SYSTEMS

                                      Varun Dilip Vaidya, Doctor of Philosophy, 2015

Dissertation directed by: Professor Steven L. Rolston and
                                      Adjunct Professor James V. Porto
                                      University of Maryland Department of Physics and
                                        National Institute of Standards and Technology

In the last two decades, experimental progress in controlling cold atoms and ions now allows us to manipulate fragile quantum systems with an unprecedented degree of precision. This has been made possible by the ability to isolate small ensembles of atoms and ions from noisy environments, creating truly closed quantum systems which decouple from dissipative channels. However in recent years, several proposals have considered the possibility of harnessing dissipation in open systems, not only to cool degenerate gases to currently unattainable temperatures, but also to engineer a variety of interesting many-body states.

This thesis will describe progress made towards building a degenerate gas apparatus that will soon be capable of realizing these proposals. An ultracold gas of ytterbium atoms, trapped by a species-selective lattice will be immersed into a Bose-Einstein condensate (BEC) of rubidium atoms which will act as a bath. Here we describe the challenges encountered in making a degenerate mixture of rubidium and ytterbium atoms and present two experiments performed on the path to creating a controllable open quantum system.

The first experiment will describe the measurement of a tune-out wavelength where the light shift of ^{87}Rb vanishes. This wavelength was used to create a species-selective trap for ytterbium atoms. Furthermore, the measurement of this wavelength allowed

us to extract the dipole matrix element of the $5s \rightarrow 6p$ transition in ^{87}Rb with an extraordinary degree of precision. Our method to extract matrix elements has found use in atomic clocks where precise knowledge of transition strengths is necessary to account for minute blackbody radiation shifts.

The second experiment will present the first realization of a degenerate Bose-Fermi mixture of rubidium and ytterbium atoms. Using a three-color optical dipole trap (ODT), we were able to create a highly-tunable, species-selective potential for rubidium and ytterbium atoms which allowed us to use ^{87}Rb to sympathetically cool ^{171}Yb to degeneracy with minimal loss. This mixture is the first milestone creating the lattice-bath system and will soon be used to implement novel cooling schemes and explore the rich physics of dissipation.

Degenerate mixtures of rubidium and ytterbium for engineering open quantum systems

by

Varun Dilip Vaidya

Dissertation submitted to the Faculty of the Graduate School of the
University of Maryland, College Park in partial fulfillment
of the requirements for the degree of
Doctor of Philosophy
2015

Advisory Committee:
Professor Steven. L Rolston, Chair/Co-advisor
Adjunct Professor James V. Porto Co-chair/Advisor
Adjunct Professor Gretchen K. Campbell
Professor Luis Orozco
Professor Mario Dagenais

Table of Contents

List of Figures

Chapter 1:   Engineering many-body dark-states in degenerate gases

Ultracold atoms have drawn immense interest in precision metrology [1], condensed matter [2,3] and quantum information [4] due to their ability to realize isolated, defect-free quantum systems. Experiments with ultracold atoms and ions remain the hallmark of quantum coherence with the stability of atomic clocks and coherence times of qubits being continually improved [5]. While much of the work performed with atomic clocks and quantum gates relies on creating *isolated* quantum systems, dissipation into an environment is necessary for cooling and can even be used to create interesting many-body states such as supersolids [6]. Just as dissipation into a photon bath allows for Doppler or resolved-sideband cooling, several proposals [7,8] have considered using phonon excitations in a Bose-Einstein condensate to carry away energy and entropy from a gas of lattice-trapped atoms, to cool the lattice to currently unattainable temperatures. More generally, the concept of engineering open many-body quantum systems has recently garnered significant theoretical interest [9,10] due to possibility of using a bath to create many-body "dark" states with interesting properties. This thesis will describe progress towards engineering a degenerate mixture capable of performing these open quantum-system experiments.

1.1   Open quantum systems

Before the formulation of quantum mechanics, some of the earliest works addressing closed, many-body systems were provided by Hamilton and Liouville. The dynamics of such systems were described by the Liouville equation which governs the time-evolution of the phase-space density $\rho(\mathbf{p}, \mathbf{q}, t)$ of a system under a Hamiltonian $H(\mathbf{p}, \mathbf{q})$.

$$\frac{\partial \rho}{\partial t} = -\{\rho, H\} \qquad (1.1)$$

1

where **p** and **q** represent the canonical co-ordinates and momenta of each of the particles in the many-body system. The Heisenberg equation was formulated as a natural extension of this concept to a quantum system, where the phase-space density is replaced by the density matrix $\hat{\rho}$ representing the state of the system and the Hamiltonian $\hat{H}$ is a Hermitian operator.

$$\frac{\partial \hat{\rho}}{\partial t} = -\frac{i}{\hbar}\left[\hat{\rho}, \hat{H}\right] \tag{1.2}$$

Time evolution under Eqn. 1.2 is described by the action of a unitary operator $\hat{U}(t) = \exp\left[-i\hat{H}t/\hbar\right]$.

In contrast, the evolution of an open system interacting with a bath cannot be described through unitary evolution. Interactions between the system and bath create correlations between the two subsystems and generate an inseparable entangled state,

$$\hat{\rho}_s(t=0) \otimes \hat{\rho}_b(t=0) \longrightarrow \hat{\rho}_{sb}(t) \neq \hat{\rho}_s(t) \otimes \hat{\rho}_b(t)$$

where the evolution of the system can no longer be determined independently of the bath. As an example, the spontaneous decay of a two-level atom (the system) entangles the sate of the atom with the state of the electromagnetic field (the bath),

$$|e\rangle |0\rangle \longrightarrow |e\rangle |0\rangle + |g\rangle |1\rangle$$

where $|0\rangle$ ($|1\rangle$) represent the absence (presence) of an emitted photon in the field.

While, the emitted photon carries away information about the full state $\hat{\rho}_{sb}(t)$, the evolution of a reduced system density matrix $\hat{\rho}_S(t) = \text{Tr}_b[\hat{\rho}_{sb}(t)]$ can still be determined by a non-unitary version of the Eqn. 1.2,

$$\frac{\partial \hat{\rho}_S}{\partial t} = -\frac{i}{\hbar}[\hat{\rho}_S, \hat{H}_s] + \mathcal{L}[\hat{\rho}_S] \tag{1.3}$$

which makes no reference to the state of the bath. The second term of Eqn. 1.3 (the Liouvillian), arises from dissipation into the bath and results in non-unitary evolution of $\hat{\rho}_S(t)$. Under certain conditions, it is possible to find "dark" states of the the system that does not evolve under $\mathcal{L}[\hat{\rho}_S]$. Such dark states have two important properties,

- The dark state is a pure state $\hat{\rho}_D = |\psi_D\rangle \langle\psi_D|$

- It decouples from the dissipative channel of the bath. $\mathcal{L}[\hat{\rho}_S] = 0$

and have been studied exhaustively in the context of coherent population trapping and stimulated Raman adiabatic passage (STIRAP). The existence of a dark-state can be illustrated in the case of a three-level atom driven by two lasers with Rabi frequencies Ω_1 and Ω_2, as shown in Fig. 1.3(a). The Hamiltonian describing this system may be expressed as,

$$\hat{V} = \omega_{g_2} |g_2\rangle \langle g_2| + \omega_e |e\rangle \langle e| + \Omega_1(|e\rangle \langle g_1| + \text{h.c.}) + \Omega_2(|e\rangle \langle g_2| + \text{h.c.}) \tag{1.4}$$

When $\Omega_2 = 0$, the atom is driven out of $|g_1\rangle$ and spontaneous emission drives it into $|g_2\rangle$, which remains unaffected by $\hat{V}$. In other words, $|g_2\rangle$ is a dark state. Conversely, when $\Omega_1 = 0$, the dark state is $|g_1\rangle$. In general for an arbitrary Ω_1 and Ω_2, the dark state is a superposition of $|g_1\rangle$ and $|g_2\rangle$. For example, in the case $\Omega_1 = \Omega_2 = \Omega$ one can trivially show that the state $(|g_1\rangle - |g_2\rangle)/\sqrt{2}$ does not get excited to $|e\rangle$ by the two lasers, and is therefore dark.

1.2 Engineering dissipation in ultracold atoms

The concept of dark states has been extended in several proposals [8–10] to many-body systems, particularly to degenerate Bose and Fermi gases. These proposals rely on creating a system of lattice-trapped atoms (hereby referred to as the system), immersed in a Bose-Einstein condensate (the bath) of another species (See Fig. 1.3(b)). Collisions between the lattice atoms and the BEC provide a way for lattice atoms to shed energy and create an open system. The remainder of this section will briefly discuss two such proposals, one with lattice-trapped bosons and another with fermions.

1.2.1 Cold atoms in lattices

The energy of a single, atom with mass m is simply the quadratic dispersion relation of the Hamiltonian,

$$\hat{H} = \frac{\hat{\mathbf{p}}^2}{2m}$$
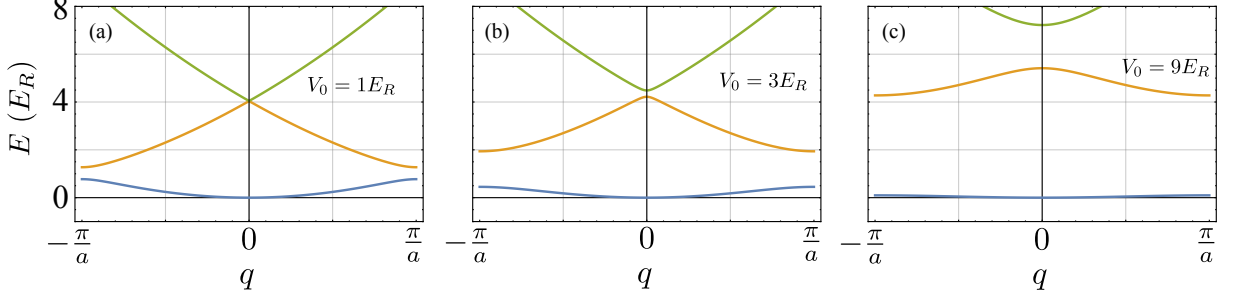
Figure 1.1: The bandgap spectrum of a single atom trapped in a sinusoidal lattice potential of different depths V_0. All energy units are stated in recoil energies $E_R = h^2/8ma^2$. The band structure is periodic in quasimomentum space q with periodicity of $2\pi/a$.

which displays a continuous spectrum as a function of the momentum $\mathbf{p}$. However, in the presence of a deep sinusoidal lattice potential, with spacing a and depth $V_0 \gg h^2/ma^2$, the energy spectrum becomes discrete displaying energy levels similar to those of a harmonic oscillator located at each lattice. More generally, in the intermediate regime the lattice displays a band gap spectrum, with bands of energy where the spectrum is continuous, and gaps where no energy levels exist, as shown in Fig. 1.1.

As an example, we calculate the spectrum for a lattice in one dimension by solving Schrodinger's equation with a sinusoidal lattice potential,

$$\hat{H}\psi(x) = \left(-\frac{\hbar^2}{2m}\frac{d^2}{dx^2} + \frac{V_0}{2}\cos(2kx)\right)\psi(x) = E\psi(x) \tag{1.5}$$

where $k = \pi/a$. The first term of Eqn. 1.5 is simply the free particle Hamiltonian with plane-wave eigenfunctions e^{iqx} and eigenenergies $\hbar^2 q^2/2m$. Since the second term (the lattice potential) only couples plane-waves that differ in momentum by $2k$, we can use an ansatz wavefunction of the form,

$$\psi(q,x) = \sum_{n=-\infty}^{+\infty} c_n e^{iqx} e^{i2nkx} \tag{1.6}$$

to solve Eqn 1.5 and find the eigenstates. Substituting Eqn. 1.6 into Eqn. 1.5 and simplifying, we get set of linear equations for c_n that must be simultaneously satisfied for an eigenstate.

$$\frac{\hbar^2}{2m}(q+2nk)^2 c_n(q) - \frac{V_0}{4}(c_{n+1}(q) + c_{n-1}(q)) = E(q)c_n(q) \tag{1.7}$$

4

Eqns. 1.7 represent an eigenvalue problem that is solved efficiently by matrix diagonalization, to get the eigenstates $\mathbf{c}(q) = [\cdots c_{-1}(q) \quad c_0(q) \quad c_{+1}(q) \cdots]$ and band energies $E(q)$. By diagonalizing this system of equations at each value of q, we can construct the energy spectra for a single particle on a lattice, which are shown in Fig. 1.1(a),(b) and (c) for three different lattice depths. For weak lattices, a small energy gap opens up at the edge ($q = \pm\pi/a$) of the lowest and first excited bands, and increases in size as the lattice depth is increased. For large lattice depths ($V_0 \gg E_R$), the width of the bands ($4J_0$) decreases, until the bands become flat and the spectrum becomes discrete as one would expect for a harmonic oscillator. In most degenerate gas experiments, all relevant temperatures are usually much smaller than the gap $4E_R$ and only the ground and first excited bands are of importance.

The lattice wavefunctions $\psi_q(x)$ (also known as the Bloch waves) can be calculated at each q using the eigenvectors $\mathbf{c}(q)$ which are found by solving the eigenvalue problem in Eqn. 1.7. The ground-band Bloch waves for $q = 0$ and $q = \pm\pi/a$ are shown in Fig. 1.2 and will be of particular importance to the two proposals that will be discussed later in this chapter. An noteworthy difference between the two Bloch functions is that while the phase of the $q = 0$ Bloch function does not change with position, the phase of the $q = \pm\pi/a$ Bloch functions varies by π over a distance a, and the sign of these wavefunctions alternates between neighboring lattice sites.

1.2.2   Driven dissipative preparation of a BEC

One of the driving forces behind research into degenerate lattice gases, has been to understand the magnetic exchange interactions that take place in real materials. Proposals to realize these interactions have considered a range of options, from using the superexchange interaction, to using dipolar atoms and polar molecules. However, realizing all of these proposals requires creating low-entropy lattice gases with temperatures much smaller than width of the ground band of the lattice, which in typical lattices can be as small at 5 nK. Hence a variety of cooling schemes, involving lattice gases immersed in a Bose-Einstein condensate, have been proposed to reach these low entropies and temperatures.
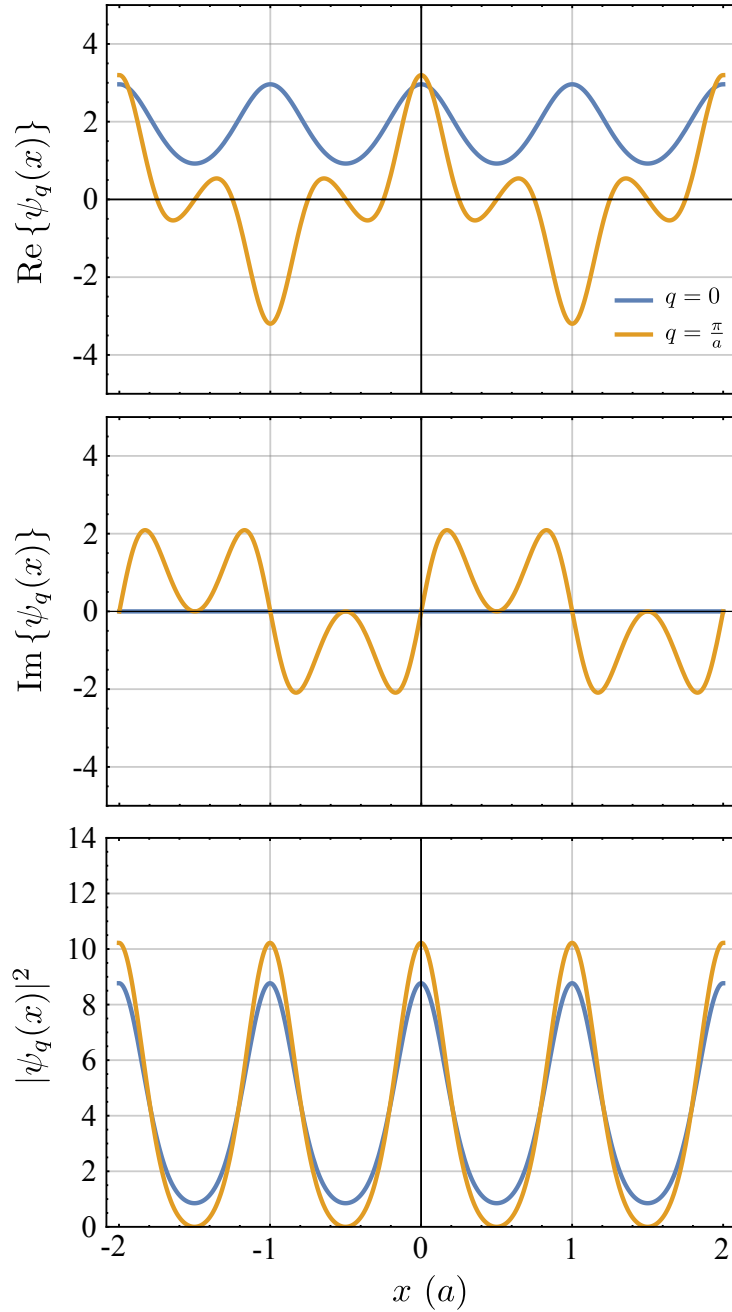
Figure 1.2: The real and imaginary components of the $q = 0$ (blue) and $q = \pi/a$ (yellow) Bloch waves in a $5E_R$ deep lattice. For $q = 0$, the sign of the wavefunction is the same over all lattice sites while for $q = \pi/a$, the wavefunction alternates in sign between lattice sites. Hence wavefunctions at the edge of the band have neighboring sites that are exactly out of phase while in the middle of the ground bad, neighboring sites are in phase. As a result $|\psi_{\pi/a}(x)|^2$ has a node between neighboring lattice sites while $|\psi_0(x)|^2$ does not.

One such scheme, presented in [8] considers using a low temperature bath to "phase-lock" bosonic atoms on neighboring sites of a lattice, thus creating a Bose-Einstein condensate in the $q = 0$ state of the lattice ground band. This scheme may be implemented by trapping lattice atoms on double-well lattice as shown Fig. 1.3(b). The two ground states of neighboring lattice sites can be considered as $|g_1\rangle$ and $|g_2\rangle$ in the three-level atom picture, while the ground state of the auxiliary lattice sites of the lattice can represent $|e\rangle$. Transitions between $|g\rangle$ and $|e\rangle$ on such a lattice may be driven using two-photon Raman processes. Spontaneous decays between $|e\rangle$ and $|g_1\rangle$ and $|g_2\rangle$ occur by the emission of a phonon into the bath. Analogous to the Λ-level scheme illustrated in Fig. 1.3(a), for any choice of Rabi frequencies Ω_1 and Ω_2, there exists a dark state which is a superposition of $|g_1\rangle$ and $|g_2\rangle$. In the special case where $\Omega_1 = -\Omega_2$ the dark state is the in-phase superposition,

$$|\psi_D\rangle = \frac{1}{\sqrt{2}}(|g_1\rangle + |g_2\rangle) \tag{1.8}$$

where the phase of the wavefunction between two neighboring sites is the same. For the case of N bosons on M lattice sites with a Rabi frequencies $\Omega_{m,m+1} = -\Omega_{m+1,m}$ the dark-state becomes,

$$|\psi_D\rangle = \left(\frac{1}{\sqrt{M}}\sum_{m=1}^{M}|g_m\rangle\right)^{\otimes N} \tag{1.9}$$

where the phase of the wavefunction is uniform over the entire lattice. In other words, this state consists of macroscopic occupation in the $q = 0$ state of the lattice and represents a BEC. Consequently in the presence of out-of-phase driving between neighboring lattice sites, the BEC becomes a dark-state and spontaneous emission of phonons drives the system into this state, thus cooling it.

For 51 bosons trapped in a $10E_R$ deep lattice, [7] claims that a similar lattice cooling scheme can reach temperatures as low as $10^{-3}J_0$. However, these and other calculations for similar proposals neglect the effect of interactions between the lattice bosons. In a lattice-trapped BEC, contact interactions between atoms dephase clouds trapped on neighboring lattice sites and drive the system out of the $q = 0$ dark-state, ultimately limiting the lowest temperatures accessible using this method of cooling. The
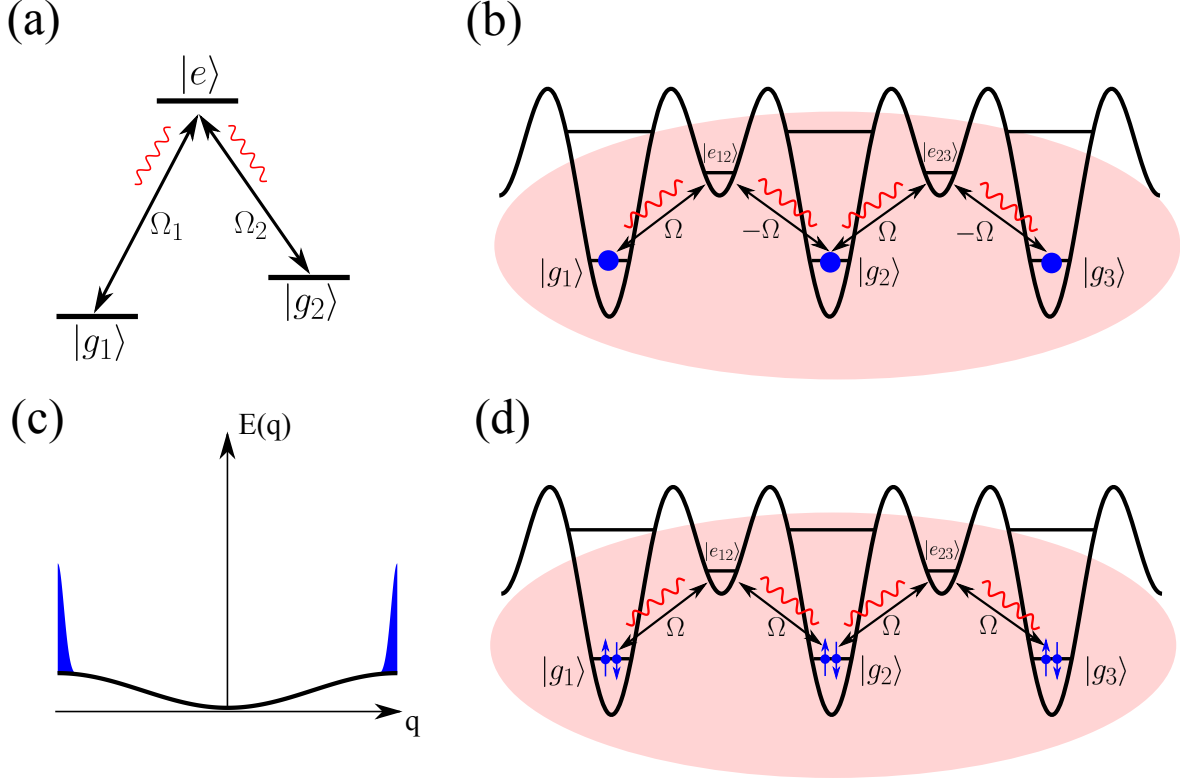
Figure 1.3: (a) Illustration of a 3-level atom in the λ-level configuration, coupled by lasers Ω_1 and Ω_2. The dark state is unaffected by the two drives and spontaneous emission of photons (red lines) populates this state. (b) Dissipative scheme for preparing BECs on a lattice. The anti-symmetric drive leaves the BEC state dark to the excitation while decays from the auxiliary sites populate this state. A similar scheme illustrated in (d) may be used to prepare the η-condensate with spin-1/2 fermions on a lattice, where the pair distribution of fermions peaks at the edge of the Brillouin zone as shown in (c).

energy scale of interactions is typically on the order of J_0 and we consequently do not expect to observe cooling significantly below this energy scale.

1.2.3 Dissipative preparation of η-condensates

At low temperatures, bosons undergo a phase transition to a BEC which displays long range order characteristic of superfluids and superconductors. However, the same phenomenon is not seen in not often seen in the ground state of Fermi gases. The η-condensate was first proposed in [11], as an excited eigenstate of the Fermi-Hubbard Hamiltonian that displays motional long-range order. It consists of *pairs* of lattice-

trapped spin-up and and spin-down fermions, whose center-of-mass momentum distribution is peaked at the $q = \pm\pi/a$ states of a lattice as shown in Fig. 1.3(c). Such a state may be prepared through dissipation using a scheme similar to the one presented in Fig. 1.3(b). Pairs of degenerate fermions in the ground band $|g_i, \uparrow\rangle \otimes |g_i, \downarrow\rangle$ of a lattice can be driven to the auxiliary band $|e\rangle$ using an *in-phase* drive ($\Omega_{m,m+1} = \Omega_{m+1,m}$), instead of the out-of-phase drive used to create a BEC. Such a drive results in a dark state of the form,

$$|\psi_D\rangle = \left(\frac{1}{\sqrt{M}} \sum_{m=1}^{M} (-1)^m |g_m, \uparrow\rangle \otimes |g_m, \downarrow\rangle \right)^{\otimes N} \tag{1.10}$$

where the phase alternates between 0 and π between neighboring lattice sites. Hence this wavefunction represents a distribution of N pairs of fermions that is peaked at $q = \pm\pi/a$ in the ground band of the lattice – in other words an η-condensate.

Unlike the proposal in the previous section where interactions would dephase the BEC dark-state, Yang argued in [11] that the η-condensate is stable to short-ranged two-particle interactions and creating this state is therefore a more promising experimental avenue.

1.3   Outline of thesis

This thesis will describe the apparatus built to conduct the aforementioned open quantum-system experiments. Chapter 2 will discuss the technical requirements for creating a mixture capable performing these experiments, and elaborate on our choice to use ytterbium and rubidium as the lattice and bath species respectively. Chapter 3 will provide an overview of the apparatus constructed over the last six years to create degenerate mixtures of rubidium and ytterbium. Finally, Chapters 4 and 5 will present two experiments performed on this apparatus – the first one being the precision measurement of tune-out wavelengths in ^{87}Rb and the second being the creation of the first Bose-Fermi mixture of rubidium and ytterbium.

Chapter 2: Degenerate gases of rubidium and ytterbium

Since the creation of the first BECs in 1995 [12, 13], the list of degenerate atomic gases has grown longer and begun encroaching on the farthest corners of the periodic table. While the alkali metals rubidium, sodium and lithium [14] have been workhorses for degenerate gas experiments, alkaline-earths such as strontium [15] and rare-earths like ytterbium [16, 17], have also been brought to degeneracy. More recently the degeneracy of strongly dipolar atoms such as chromium [18], dysprosium [19] and erbium [20] has opened the possibility of observing magnetic dipole-dipole interactions in ultracold gases.

At the same time, experiments with mixtures of degenerate gases have gained momentum, fueled by an interest in observing long-range interactions between polar molecules [21, 22], for example. However, creating a degenerate mixture requires simultaneously satisfying several stringent requirements regarding the stability, miscibility and collisions between the two gases:

- The single-species and interspecies inelastic collision rates must be low.

- The single-species and interspecies elastic collision rates must be large enough to allow for thermalization and evaporative cooling.

- The two gases must be stable to collapse, and miscible when degenerate.

This chapter is intended to provide an overview of the properties of rubidium and ytterbium, which make them an ideal choice for engineering the open quantum systems discussed in Chapter 1. The first section will provide an overview of the electronic structure of the two atoms, as it pertains to degenerate gas experiments. The second will provide a brief introduction to degenerate gases and the third will analyze the collisional properties of a rubidium-ytterbium mixture, in the context of the three requirements

10

stated previously. Finally the fourth section will describe details of the trap we have engineered to bring rubidium-ytterbium mixtures to degeneracy.

2.1 Electronic structure of Rb and Yb

2.1.1 Rubidium

Bose-Einstein condensation was first achieved in ^{87}Rb and it still remains the gold standard for degenerate gas experiments. Its popularity stems from a variety of factors such as its favorable scattering properties, low melting point and ease of laser cooling at commercially available laser wavelengths.

Being an alkali metal, its valence shell ($n = 5$) has one electron resulting in a $5S_{1/2}$ ground state as shown in 2.1(a). The two lowest energy transitions in the atom are to the $5P_{1/2}$ (795 nm) and $5P_{3/2}$ (780 nm) states, separated by the fine structure splitting Δ_F. In addition, the nuclear spin of the atom ($I = 3/2$ in ^{87}Rb and $5/2$ in ^{85}Rb) results in a hyperfine splitting Δ_{HF} of both the ground and excited states and the total angular momentum $F = I + J$ of either isotope is always an integer, causing both isotopes to obey Bose-Einstein statistics.

Over the years, techniques to create ^{87}Rb BECs have improved tremendously and a de facto standard exists within the JQI, for reliably producing large condensates of up to 2×10^6 atoms [23]. Hence rubidium was a natural choice to create a large degenerate bosonic bath for engineering open quantum systems.

2.1.2 Ytterbium

A remarkable property of ytterbium is its rich isotopic composition shown in Table 2.1(a), consisting of five stable bosonic isotopes with no nuclear spin and two stable fermionic ones - ^{171}Yb and ^{173}Yb - with nuclear spins of $I = 1/2$ and $5/2$ respectively. As a result it is an ideal choice for investigating Bose-Bose, Bose-Fermi and Fermi-Fermi mixtures, all three of which have been realized in Yb through various experiments conducted by the Takahashi group [24–26]. The ability to easily switch between bosonic

(a)

Yb Isotope		I	Natural abundance (%)	Yb −Yb a_s (a_0)	Yb − ^{87}Rb a_s (a_0)	Yb − ^{85}Rb a_s (a_0)
168 ★		0	0.13	252(3)	39(2)	230(12)
170 ○		0	3.04	64(2)	-12(3)	140(3)
171		1/2	14.28	-3(4)	-59(4)	117(2)
172 ●▲		0	21.83	-599(64)	-161(11)	100(2)
173 ●▲		5/2	16.13	199(2)	-626(88)	84(2)
174 ●■		0	31.83	105(2)	880(12)	70(2)
176 ■▲		0	12.67	-24(4)	217(5)	39(2)

(b)

Yb Isotope	$K_3^{(YbYb)}$ (cm^{6}s^{-1})	$K_3^{(RbYb)}$ (cm^{6}s^{-1})
168 ★	1.4×10^{-28}	4.3×10^{-32}
170 ○	5.7×10^{-31}	3.8×10^{-34}
171	2.7×10^{-36}	2.2×10^{-31}
172 ●▲	4.3×10^{-27}	1.2×10^{-29}
173 ●▲	5.2×10^{-29}	2.8×10^{-27}
174 ●■	4.0×10^{-30}	1.1×10^{-26}
176 ■▲	1.1×10^{-32}	4.0×10^{-29}

★ Abundance too low
○ γ_{el} too low
● γ_3 too high
▲ Unstable to collapse
■ Immiscible

Table 2.1: (a) The abundance and scattering lengths (a_0) of different isotopic combinations of Rb and Yb. The Rb-Yb scattering lengths were determined in [27] and the Yb-Yb lengths in [28]. (b) Three-body recombination constants K_3 for different isotopic combinations of ^{87}Rb and Yb. The symbols next to each isotope indicate why a degenerate mixture with ^{87}Rb would not work.

and fermionic isotopes, made ytterbium an attractive choice to use as a lattice gas in engineering open quantum systems.

The ground state of ytterbium has two valence electrons in the $6s$ orbital, resulting in an electronic structure that resembles alkaline-earth atoms such as strontium or calcium. Consequently, the electronic states of ytterbium can be sorted into singlet ($S = 0$) or triplet ($S = 1$) manifolds as illustrated in Fig. 2.1(b). While electric-dipole selection rules allow transitions within a given spin manifold (eg. $^1S_0 \rightarrow {}^1P_1$), an electric field cannot change electron spin and transitions between manifolds (eg. $^1S_0 \rightarrow {}^3P_1$) should be forbidden. However in heavy atoms like ytterbium ($Z = 70$), $j - j$ spin-orbit coupling introduces a small admixture of the $^1P_1$ state into the $^3P_1$ state, weakly allowing inter-manifold transitions such as the narrow intercombination transition at 556 nm in ytterbium. As a result, ytterbium atoms have both a broad principal transition at

399 nm useful for capturing atoms from a thermal gas, and a narrow intercombination transition at 556 nm with a laser cooling Doppler limit of 4.3 μK.

The $^1S_0$ ground state of Yb has no electronic angular momentum and is truly non-magnetic for the bosonic isotopes, which additionally lack a nuclear spin. Consequently, both the principal and intercombination lines of bosonic isotopes are $J = 0 \to 1$ transitions, as shown by Fig. 2.1(d). In contrast, the nuclear magnetic moment of the fermions ^{171}Yb and ^{173}Yb leads to magnetic structure in $^1S_0$ (see Fig. 2.1(e)). Furthermore the excited states, which do have an electron spin, experience a hyperfine splitting, leading to multiple hyperfine states in $^1P_1$ and $^3P_1$. Both the principal and intercombination transitions experience large differential Zeeman splittings, since the excited states have a magnetic moment proportional to the Bohr magneton μ_B while the ground states Zeeman shift is determined by the much smaller nuclear magneton μ_N.

2.2 Degenerate gases

2.2.1 Fermions

An unpolarized spin S Fermi gas at zero temperature will uniformly fill the single-particle eigenstates below the Fermi energy ϵ_F with an occupation of $2S+1$ while leaving those above the Fermi energy unoccupied (see Fig. 2.2(a)) . At a finite temperature T, the occupancy of a state with energy ϵ is given by the Fermi-Dirac distribution,

$$n(\epsilon) = \frac{2S+1}{e^{(\epsilon-\mu)/k_B T} + 1} \tag{2.1}$$

where the chemical potential μ is set by the normalization condition,

$$\int g(\epsilon)n(\epsilon)\mathrm{d}\epsilon = N \tag{2.2}$$

where $g(\epsilon)$ is the density of states. In the limit $T = 0$, the chemical potential μ is equal to the Fermi energy ϵ_F. The Fermi-Dirac distribution may be used to evaluate the energy, density and momentum distributions of a harmonically trapped Fermi-gas with a single particle energy,

$$\epsilon(\mathbf{p}, \mathbf{r}) = \frac{\mathbf{p}^2}{2m} + \frac{1}{2}m(\omega_x^2 x^2 + \omega_y^2 y^2 + \omega_z^2 z^2) \tag{2.3}$$
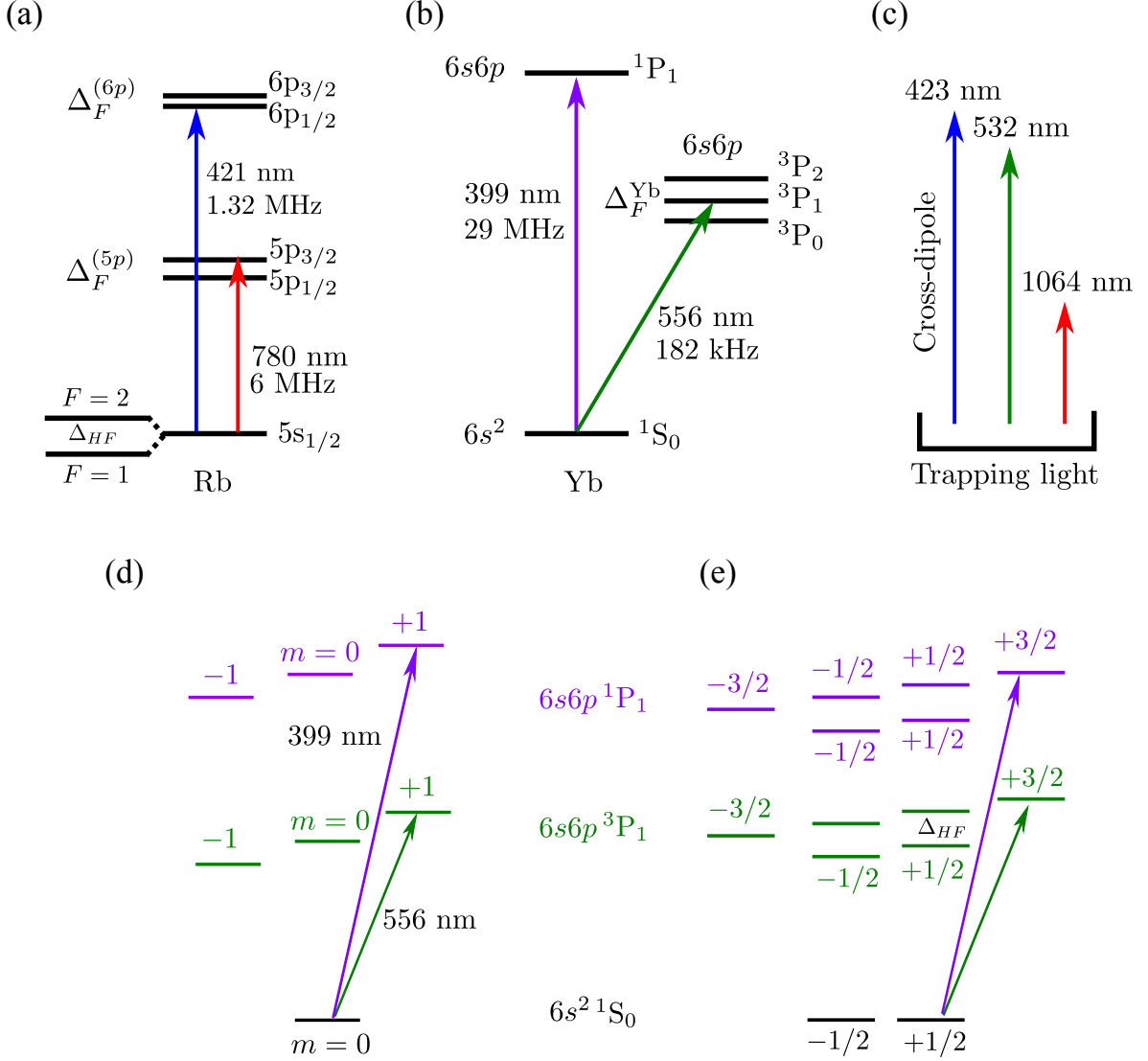
Figure 2.1: Electronic level structure of Rb and Yb atoms. (a) Electronic structure of Rb atoms. (b) Electronic structure of Yb atoms. (c) Dipole trap wavelengths used. (d) Magnetic structure of Yb bosons. (e) Magnetic structure of a Yb fermion (^{171}Yb). The ground state sublevels of Yb fermions experience a negligible Zeeman shift of (375 Hz/G for ^{171}Yb and 516 Hz/G for ^{173}Yb), arising solely from the magnetic moment of the nucleus.

Typically the Fermi energy ϵ_F is greater than the spacing between the harmonic oscillator eigenstates ω by at least an order of magnitude and in this regime the states may be enumerated by $\mathbf{p}$ and $\mathbf{x}$ instead of the harmonic oscillator numbers (n_x, n_y, n_z). The Fermi energy of a harmonically trapped gas is obtained by evaluating the normalization

condition in Eqn. 2.2 at $T = 0$.

$$\epsilon_F = \left(\frac{6N}{2S+1}\right)^{1/3} \hbar\bar{\omega} \tag{2.4}$$

where $\bar{\omega} = \sqrt[3]{\omega_x\omega_y\omega_z}$. The equilibrium density and momentum distributions may be obtained by integrating the Fermi-Dirac distribution (Eqn. 2.1) over momentum and position space respectively (see Appendix A for a detailed derivation),

$$n(\mathbf{r}) = -(2S+1)\left(\frac{2\pi}{\lambda_T}\right)^3 \Gamma(3/2)\mathrm{Li}_{3/2}\left\{e^{[\mu-V(\mathbf{r})]/k_BT}\right\} \tag{2.5}$$

$$n(\mathbf{p}) = -(2S+1)\left(\frac{\sigma_T}{h}\right)^3 \mathrm{Li}_{3/2}\left\{e^{[\mu-\mathbf{p}^2/2m]/k_BT}\right\} \tag{2.6}$$

where λ_T is the thermal deBroglie wavelength, $\sigma_T = \sqrt{k_BT/m\bar{\omega}^2}$ the thermal width of a trapped non-degenerate cloud, and $\mathrm{Li}_{3/2}$ is a polylogarithm of order $3/2$. Comparing the density distribution of a zero-temperature trapped Fermi-gas to that of a harmonic oscillator, we find that its size is much larger than than the harmonic oscillator length a_{ho}.

2.2.2 Bosons

As is well known from statistical mechanics, an ideal Bose gas trapped in a potential $V(\mathbf{r})$, undergoes a phase transition to a Bose-Einstein condensate (BEC) near degeneracy. The defining property of a BEC is a macroscopic occupation of the ground (zero-momentum) state, $|\mathbf{k} = \mathbf{0}\rangle$. The critical temperature for the BEC phase transition in a uniform gas with density n is given by,

$$T_c = \left(\frac{n}{2.614}\right)^{2/3} \frac{2\pi\hbar^2}{mk_B} \tag{2.7}$$

and in the more commonly used harmonic trap is,

$$T_c = \frac{\hbar\bar{\omega}}{k_B}\left(\frac{N}{\mathrm{Li}_3\{1\}}\right) \tag{2.8}$$

as derived in Appendix A. For $T \ll T_c$, since the many-body wavefunction $|\Psi\rangle$ we can assume that the many-body wavefunction $|\Psi\rangle$ consists of all particles in the same same

single-particle ground state $|\psi\rangle$ allowing us to write a Hartree-Fock approximation for the many-body wavefunction,

$$|\Psi\rangle = |\psi\rangle \otimes |\psi\rangle \otimes |\psi\rangle \otimes ... \qquad (2.9)$$

In this regime, the dyanmics of a BEC are well approximated by mean-field theory, with an order parameter $\psi(\mathbf{r})$ to represent the wavefunction of the entire BEC. The spatial wavefunction of the BEC $\psi(\mathbf{r})$ is normalized to the the total number of particles N in the condensate.

For a non-interacting, trapped BEC, $\psi(\mathbf{r})$ satisfies Schrodinger's equation. Weak contact interactions between bosons may be modeled by a psuedopotential of the form $V(\mathbf{r}_i - \mathbf{r}_j) = g\delta(\mathbf{r}_i - \mathbf{r}_j)$. These interactions introduce a non-linear, density-dependent term into the Hamiltonian resulting in the Gross-Pitaevskii equation,

$$-\frac{\hbar^2}{2m}\nabla^2\psi(\mathbf{r}) + V(\mathbf{r})\psi(\mathbf{r}) + g|\psi(\mathbf{r})|^2\psi(\mathbf{r}) = \mu\psi(\mathbf{r}) \qquad (2.10)$$

Vanishing interactions ($g \to 0$) reduce Eqn. 2.10 to Schrodinger's equation and the BEC wavefunction is simply the ground state of the trap $V(r)$. In the case of a harmonic trap, as is typically used in most BEC experiments, the wavefunction is the Gaussian ground state of a harmonic oscillator. While Eqn. 2.10 cannot always be solved analytically for repulsive interactions ($g > 0$), we can use the Thomas-Fermi approximation to estimate a BEC wavefunction. This approximation assumes that at low enough temperatures, the density $|\psi(\mathbf{r})|^2$ of the Bose gas is large enough that interactions dominate and the kinetic energy term of the Hamiltonian may be neglected. Under this condition Eqn. 2.10 is trivially solved for the Thomas-Fermi solution,

$$\psi_{TF}(\mathbf{r}) = e^{i\phi}\sqrt{\frac{\mu - V(\mathbf{r})}{g}} \qquad (2.11)$$

where the chemical potential μ is set by the normalization condition,

$$\int |\psi(\mathbf{r})|^2 \mathrm{d}^3\mathbf{r} = N$$

Eqn. 2.11 shows that the density distribution $|\psi_{TF}(\mathbf{r})|^2$ mirrors the trap potential. In a harmonic trap with frequencies $(\omega_x, \omega_y, \omega_z)$, the Thomas-Fermi density distribution

16
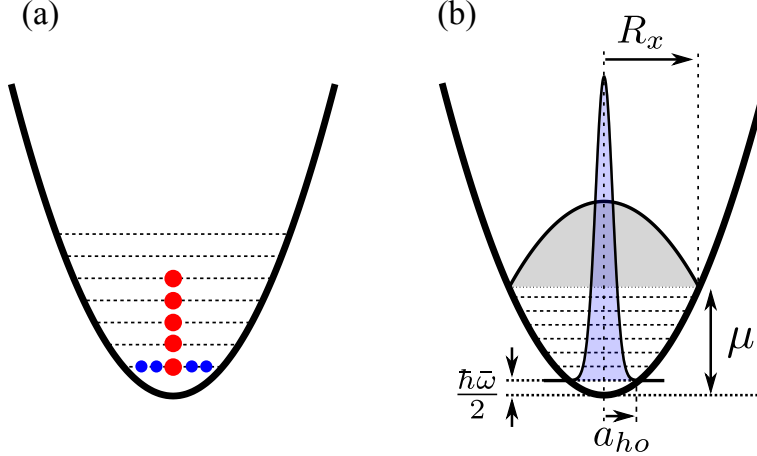
Figure 2.2: (a) Occupation of degenerate bosons (blue) and fermions (red) in a harmonic trap. (b) Comparison of the ground state harmonic oscillator wave function (blue) and the Thomas-Fermi solution (gray) for a BEC in a harmonic trap.

$|\psi_{TF}(\mathbf{r})|^2$ is given by,

$$|\psi_{TF}(\mathbf{r})|^2 = n_0 \left(1 - \frac{x^2}{R_x^2} - \frac{z^2}{R_y^2} - \frac{z^2}{R_z^2} \right) \qquad (2.12)$$

where the Thomas-Fermi radii R_i are determined by the atom number, trap frequency ω_i and interaction strength g. Qualitatively comparing the Thomas-Fermi solution to the ground state of a harmonic oscillator (see Fig. 2.2(b)), we can see that the Thomas-Fermi radii for repulsive interactions are typically much larger than than harmonic oscillator length a_{ho}. This is the result of an outward pressure against the trap potential caused by repulsive interactions between atoms. While this may qualitatively seem similar to behavior of a degenerate Fermi gas, it is important to note that this pressure arises from *real* interactions in bosons, while in fermions this is caused by the Fermi pressure. The case for attractive interactions is more complicated and will be discussed later in this chapter.

The density and momentum distributions of an *uncondensed* Bose gas near degeneracy may be evaluated using the Bose-Einstein distribution. The full derivation, presented in Appendix A, yeilds the results,

$$n(\mathbf{r}) = (2S + 1) \left(\frac{2\pi}{\lambda_T} \right)^3 \Gamma(3/2) \mathrm{Li}_{3/2} \left\{ -e^{-V(\mathbf{r})/k_B T} \right\} \qquad (2.13)$$

$$n(\mathbf{p}) = (2S + 1) \left(\frac{\sigma_T}{h} \right)^3 \mathrm{Li}_{3/2} \left\{ e^{-\mathbf{p}^2/2mk_B T} \right\} \qquad (2.14)$$
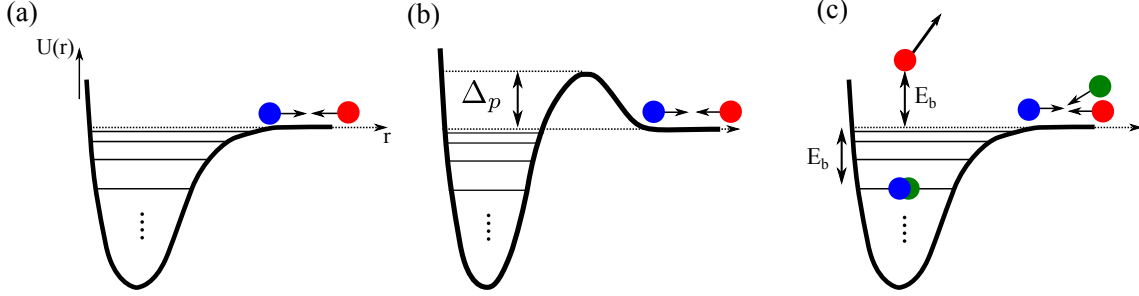
Figure 2.3: (a) An illustration of the van Der Waals' potential experience by two colliding atoms in their ground states. (b) The energy of colliding atoms at ultracold temperatures is typically well below the p-wave barrier Δ_p. (c) Three-body inelastic collisions. Two atoms bind of form a molecule and the binding energy E_b is carried away by the third.

analogous to those of fermions.

2.3 Collisional properties

Knowledge of the scattering amplitudes between two atoms is crucial to degenerate gas experiments as it determines the elastic collision rates, two and three-body inelastic rates, the stability of BECs and behavior of two-species mixtures. These amplitudes are determined by the molecular potential (illustrated in Fig. 2.3) between the two atoms which may be approximated by the van der Waals' potential,

$$V(r, l) = \frac{C_{12}}{r^{12}} - \frac{C_6}{r^6} + \frac{\hbar l(l+1)}{2\mu r^2} \tag{2.15}$$

where the first two terms represent the van der Waals' potential and the second term is the effective centrifugal potential for the scattering in the l-th partial wave. This section will discuss the self and interspecies scattering properties of Rb and Yb atoms that made them a good choice for satisfying the three requirements stated at the beginning of this chapter.

2.3.1 Elastic collision rates

The temperatures required to reach degeneracy are reached by evaporative cooling which relies on elastic collisions to thermalize a non-equilibrium gas. At the low temper-

atures typically encountered in degenerate gas experiments, the energy of two colliding atoms is well below the p-wave centrifugal barrier (Δ_p in Fig. 2.3) and elastic scattering is dominated by the s-wave channel. In this regime the scattering cross-section is given by the s-wave scattering length a_s,

$$\sigma_s = 4\pi a_s^2 \tag{2.16}$$

and the average elastic collision rate per atom in a gas with density n and temperature T is,

$$\gamma_{el} = n\sigma_s \langle v_r \rangle_T \tag{2.17}$$

with $\langle v_r \rangle_T$ representing the relative thermal velocity between two atoms in the gas.

The characteristic timescale for performing efficient evaporation is on the order of $2.8/\gamma_{el}$. For a trapped ^{87}Rb gas ($a_s = 98a_0$) at 10 μK with a typical density of 10 μm^{-3}, this timescale is on the order of 0.2 s, allowing for rapid production of BECs. The scattering lengths for different Yb isotopes, presented in Table 2.1, vary over a wide range as a function of the isotope mass. ^{168}Yb, ^{170}Yb, ^{173}Yb and ^{174}Yb have scattering lengths large enough to allow for efficient evaporation and have been brought to Bose or Fermi degeneracy [16,17,24]. The remaining isotopes have been sympathetically cooled to degeneracy using either ^{174}Yb or ^{173}Yb, with the exception of ^{172}Yb which we have not been able to condense for reasons that will be discussed later in this chapter.

During the construction of this project, the exact values of interspecies scattering lengths between Rb and Yb isotopes were unknown. However, choosing an atom with a large number of stable isotopes increased the probability of finding favorable scattering lengths and motivated ytterbium as a choice for a second species. Interspecies scattering lengths, first determined in 2011 in [27], are tabulated in Table 2.1(a) and plotted in Fig. 2.4. The Rb-Yb scattering lengths display behaviour analogous to a Feshbach resonance, which can be tuned by the reduced mass μ of the Rb-Yb isotopologue. The hollow circles in Table 2.1(a) indicate isotopes whose interspecies scattering length with ^{87}Rb is too low to conduct two-species experiments on a reasonable timescale.
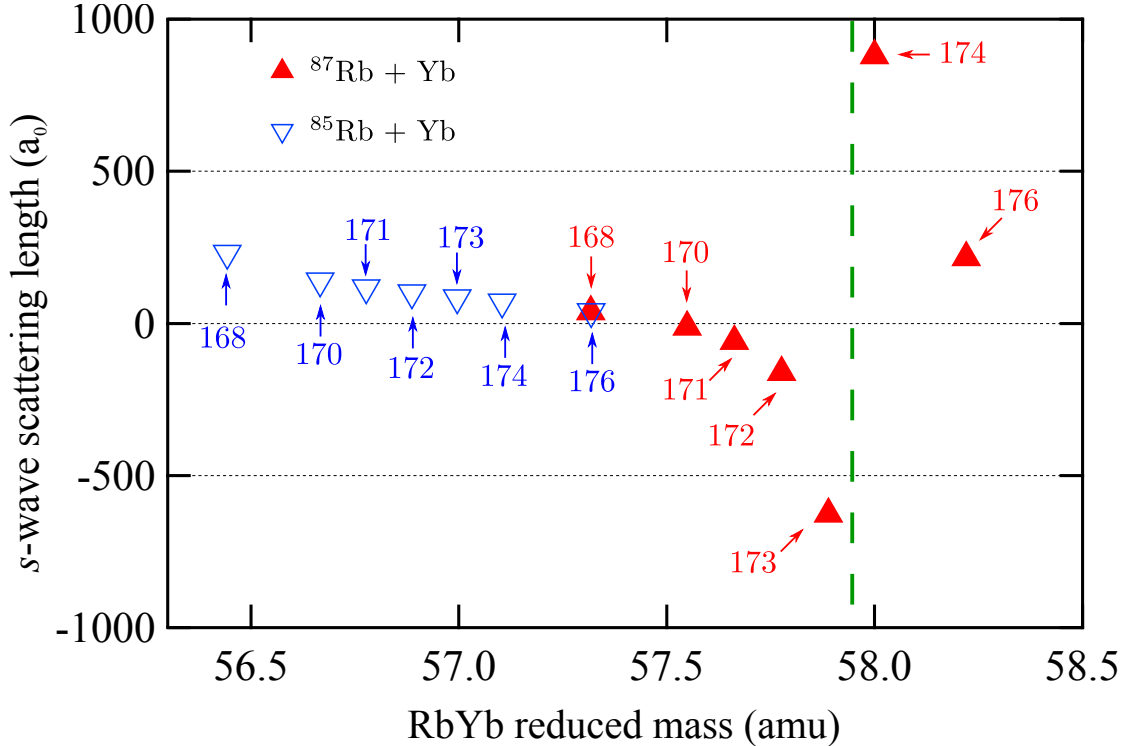
Figure 2.4:   s-wave scattering lengths of Rb-Yb isotopologues as a function of reduced mass μ [27].   The dotted vertical line indicates the reduced mass of the effective Feshbach resonance, where the scattering lengths diverge. Most isotopologues with [87]Rb lie near this resonance and consequently have a wide range of scattering lengths.

2.3.2   Inelastic collision rates

Inelastic collisions between atoms occur when the internal state of either atom changes during a collision, resulting in a release of kinetic energy. Typically, inelastic collisions are undesirable as they cause trap loss in a cloud, and care must be taken to minimize three-body inelastic rates which tend to be the dominant sources of atom loss in dilute, trapped gases.

Three-body recombination occurs when a pair of colliding atoms form a molecular bound state by releasing the binding energy through a third atom (see Fig. 2.3). These binding energies tend to be orders of magnitude larger the trap depth and all three atoms are typically lost from the trap. While the molecular branching ratios for three-body recombination are not well known in most atomic gases, one can nevertheless construct

a phenomenological expression of the three-body recombination rate per atom,

$$\gamma_3 = K_3 n^2 \tag{2.18}$$

where K_3 is the three-body constant in units of cm^{6}s^{-1}. In a spin polarized ^{87}Rb gas, the value of K_3 has been measured by several groups [29, 30] to be $4.3(1.8) \times 10^{-29}$ cm^{6}s$^-$1. At typical experimental densities of 10 μm^{-3}, the results in a thermal recombination rate of $\gamma_3^{(Rb)} = 0.0043$ s^{-1}, which is over four orders of magnitude slower than the elastic scattering rates necessary for efficient evaporation.

Through trap loss measurements done by the Takahashi group [16], the three-body recombination constant in ^{174}Yb was estimated to be 4×10^{-30} cm^{6}s$^-$1 resulting in favorable recombination rates of $\gamma = 4 \times 10^{-4}$ s^{-1}. Recombination constants for other Yb isotopes can be extrapolated from the ^{174}Yb value, using a simple scaling law that depends on a_s. The probability of any given atom in a gas colliding with a second atom is proportional to the elastic collision rate $P_{coll} \propto \gamma_{el} \propto a_s^2$ mentioned in the previous subsection. Three-body recombination occurs when a single atom collides with two other atoms, and the probability of such an event happening must be given by $P_{coll}^2 \propto a_s^4$ leading to the relation $K_3 \propto a_s^4$. A more rigorous derivation presented in [31] arrives at the scaling law,

$$K_3 \propto \frac{a_s^4}{\mu} \tag{2.19}$$

from which the three-body constants for isotopes other than ^{174}Yb were determined are are presented in Table 2.1(b). The interspecies three-body rate between ^{87}Rb and ^{174}Yb was inferred thorough phase separation measurements carried out in [32], to be $K_3 = 1.1 \times 10^{-26}$ cm^{6}s^{-1}. The approximate three-body constants for other isotopologues are extrapolated from this value using the scaling law in Eqn. 2.19 and are presented in Table 2.1(b).

Efficient evaporation or sympathetic cooling requires the elastic scattering rate between two gases to cause rethermalization well before inelastic collisions lead to trap loss. In other words, under typical densities of 10 μm^3 and temperatures of 10 μK, the condition

$$\gamma_{el} \gg \gamma_3 \tag{2.20}$$

must be satisfied for single-species and interspecies collisions. The red circles in Tables 2.1(a) and (b) indicate Yb isotopes that would undergo rapid three-body recombination, either with themselves or with ^{87}Rb, and Eqn. 2.20 cannot be satisfied. While the interspecies interactions with ^{85}Rb result in more favorable recombination rates, ^{85}Rb has a large negative self-scattering length of -400 a_0. While a magnetic Feshbach resonance was used in [33], to tune the s-wave scattering length ^{85}Rb and create a stable BEC, our apparatus uses a quadrupole magnetic trap with non-uniform magnetic fields. Consequently, creating an ^{85}Rb-Yb mixture would not be a trivial task and would require a significant overhaul of the experiment.

2.3.3 Miscibility of degenerate gases

The interactions in a degenerate Bose-Bose RbYb mixture can be characterized by three different s-wave scattering lengths – the two single-species lengths a_{rr} and a_{yy} for Rb and Yb respectively, and an interspecies one a_{ry}. The miscibility of the two gases is determined by the relative magnitudes and signs of the three scattering lengths. For $a_{ry} < 0$ miscibility is guaranteed since an Rb atom can always lower its energy by interacting with a Yb atom. For repulsive interspecies interactions, the miscibility condition may be estimated by a mean-field approach presented in [34]. This approach considers two interacting gases with numbers N_R and N_Y, mutually trapped in a square well with volume V. In this trap, the Thomas-Fermi solution (Eqn. 2.11) for the BEC wavefunction is a uniform cloud with density $N_{R(Y)}/V$. The kinetic energy of the two gases may be neglected and the ground-state energy E_0 will be dominated by the non-linear interaction term of the Gross-Pitaevskii equation,

$$E_0 \approx \langle \psi_{BEC} | g |\psi(\mathbf{r})|^2 |\psi_{BEC}\rangle = g\frac{N^2}{V} \tag{2.21}$$

where $g = 4\pi\hbar^2 a_s/m$ is the contact interaction strength. The contribution to this energy from Rb (Yb) cloud interacting with itself scales as $N_{R(Y)}^2$ and the contribution from the interspecies interaction scales as $N_R N_Y$.

In the absence of interspecies interactions ($a_{ry} = 0$), the two-species ground-state is miscible and homogeneous with a constant density N_i/V for each species i. Hence the

energy of the ground state can be written as,

$$E_0 = 4\pi\hbar^2 \left[\frac{a_{rr}}{m_R} \frac{N_R^2}{V} + \frac{a_{yy}}{m_Y} \frac{N_Y^2}{V} \right]$$

where the first and second term represent the Rb and Yb interaction energies. The energy of this homogeneous state with an interspecies interaction is,

$$E_{hom} = 4\pi\hbar^2 \left[\frac{a_{rr}}{m_R} \frac{N_R^2}{V} + \frac{a_{yy}}{m_Y} \frac{N_Y^2}{V} + \frac{2a_{ry}}{\mu_{RY}} \frac{N_Y N_R}{V} \right] \tag{2.22}$$

However if we consider an inhomogeneous state, with Rb atoms exclusively occupying a volume V_R and the Yb atoms occupying V_Y, the energy of this state becomes,

$$E_{in} = 4\pi\hbar^2 \left[\frac{a_{rr}}{m_R} \frac{N_R^2}{V_R} + \frac{a_{yy}}{m_Y} \frac{N_Y^2}{V_Y} \right]$$

which when minimized with respect to V_R and V_Y, under the constraint $V_R + V_Y = V$ results in,

$$E_{in} = 4\pi\hbar^2 \left[\frac{a_{rr}}{m_R} \frac{N_R^2}{V} + \frac{a_{yy}}{m_Y} \frac{N_Y^2}{V} + \frac{2\sqrt{a_{rr}a_{yy}}}{\mu_{RY}} \frac{N_Y N_R}{V} \right] \tag{2.23}$$

Comparing Eqns. 2.22 and 2.23, one can see that under the condition $\sqrt{a_{rr}a_{yy}} < a_{ry}$, the inhomogeneous state has a lower energy than the homogeneous one. Consequently, when the miscibility condition is violated, the Rb and Yb atoms can always lower their energy by phase-separating at different locations.

The Bose-Bose miscibility condition for Rb-Yb is not satisfied with [174]Yb and [176]Yb, leading to their elimination as possible candidates for a degenerate mixture. The fermionic isotopes [173]Yb and [171]Yb are guaranteed to be miscible since their interspecies scattering lengths with [87]Rb are negative. The purple squares in Tables 2.1(a) and (b) indicate isotopes of Yb that would be immiscible with an [87]Rb BEC.

2.3.4 Stability under interactions

In the absence of interactions a trapped Bose-gas will condense into the $\mathbf{k} = 0$ momentum state and its excitation spectrum is simply the quadratic spectrum of a free particle. The Bogoliubov spectrum of a weakly interacting BEC with density n is given by,

$$\epsilon(\mathbf{k}) = \sqrt{\frac{\hbar^2 k^2}{2m}(k^2 + 16\pi n a_s)} \tag{2.24}$$

Repulsive interactions ($a_s > 0$) result in a linear spectrum $\epsilon(\mathbf{k}) \approx ck$ at low momenta, which arises from phonon modes in the BEC. In contrast, attractive interactions ($a_s < 0$) cause an instability of the low energy modes as the energy becomes imaginary for $k^2 < 16\pi n|a_s|$. However in any trapped gas, k cannot be arbitrarily small and its minimum value $k_{min} \sim \pi/R_0$ is determined by the size - R_0 - of the ground state of the trap. An attractively interacting BEC is stable as long as the $\epsilon(k_{min})$ remains real, which sets an upper limit on BEC density n according to Eqn. 2.24. In a harmonic trap R_0 is on the order of the harmonic oscillator length a_{ho}, and this can be used to estimate a critical number, beyond which a BEC becomes unstable to collapse.

$$N_{max} \approx \frac{a_{ho}}{a_s} = \sqrt{\frac{2\hbar}{m\omega_0 a_s^2}} \tag{2.25}$$

In a typical 100 Hz trap, the attractively interacting bosons ^{172}Yb and ^{176}Yb would have critical numbers of 150 and 760 respectively, and do not form large stable condensates. Creating usable condensates ($\approx 10^4$ atoms) of these isotopes would require extremely loose traps (0.001 Hz for ^{172}Yb and 0.1 Hz for ^{176}Yb) which are extremely challenging to implement in practice. An alternative route to creating condensates of these isotopes would involve using an optical Feshbach resonance (OFR) [35] on the intercombination transition of Yb, as suggested in [36]. Such resonances rely on coupling the ground state motional wavefunction of two colliding atoms to an that of an electronically excited molecular state, in order to change the scattering length between the two atoms. Unfortunately, the excited molecular state can decay by imparting a large kinetic energy to both atoms, leading to trap loss characterized by a two-body loss coefficient K_2

$$\Gamma_2 = K_2 n \tag{2.26}$$

Resonant values of K_2 were calculated in [36] for promising OFRs in ^{172}Yb and ^{176}Yb to be 2.8×10^{-14} cm^{3}s^{-1} and 2.5×10^{-15} cm^{3}s^{-1} respectively. For a typical BEC atomic density of $n = 100$ μm^{-3}, the loss rates near the OFR would be 2.8 s^{-1} for ^{172}Yb, which would lead to a short lived BEC and 0.25 s^{-1} for ^{176}Yb. Hence while creating a ^{172}Yb BEC might not be possible, ^{176}Yb still remains a candidate for creating a Bose-Bose mixture with ^{87}Rb. However, this route was not pursued since it requires a second 556 nm laser to implement an OFR on the intercombination transition.

The stability condition for a Fermi-gas is slightly more complicated since the Fermi-energy is typically larger than the interactions by over an order of magnitude. As a result, the outward Pauli pressure stabilizes the Fermi sea against collapse even in the presence of attractive interactions. Consequently, both ^{171}Yb and ^{173}Yb are stable to collapse near degeneracy. However, in the presence of a high-density ^{87}Rb BEC, the strong attractive *interspecies* interaction between ^{173}Yb and ^{87}Rb can destabilize the Fermi sphere and cause collapse. The condition for interspecies collapse may be estimated by a variational principle similar to the one described in the previous section and explained in detail in [37]. At zero temperature, the total energy of the interacting RbYb Bose-Fermi mixture is given by,

$$E_0 = 8\pi\hbar^2 \left[\frac{1}{2} \frac{a_{rr}}{m_R} \frac{N_R^2}{V} + \frac{a_{ry}}{\mu_{RY}} \frac{N_R N_Y}{V} + \frac{3}{5} N_Y \epsilon_F^{(Y)} \right] \tag{2.27}$$

where the last term represent the total energy of the ytterbium Fermi sphere. For a minimum to exist for small variations in the densities $n_i = N_i/V$, the condition,

$$\frac{\partial \mu_R}{\partial n_R} \frac{\partial \mu_Y}{\partial n_Y} - \frac{\partial \mu_R}{\partial n_Y} \frac{\partial \mu_Y}{\partial n_R} \geq 0 \tag{2.28}$$

must be satisfied where μ_i are the chemical potentials for Rb and Yb.

$$\mu_R = 8\pi\hbar^2 \left[\frac{1}{2} \frac{a_{rr}}{m_R} \frac{N_R^2}{V} + \frac{a_{ry}}{\mu_{RY}} \frac{N_R N_Y}{V} \right]$$

$$\mu_Y = \epsilon_F^{(Y)} + 4\pi\hbar^2 \frac{a_{ry}}{\mu_{RY}} \frac{N_R}{V}$$

One can show that Eqn. 2.28 can only by satisfied under the condition,

$$n_Y^{1/3} \leq \frac{(6\pi^2)^{2/3}}{12\pi} \frac{\mu_{RY}^2}{m_R m_Y} \frac{a_{RR}}{a_{RY}^2} \tag{2.29}$$

which sets an upper limit on the density required to keep the attractively interacting mixture from collapsing. For the scattering lengths presented in Table 2.1, the upper limit for ^{173}Yb density is on the order of 1 μm^{-3}. The Fermi energy at these densities is 50 nK and reaching into the deeply degenerate regime would be challenging. Hence ^{173}Yb was eliminated as a candidate for a degenerate mixture. The yellow triangles in Tables 2.1(a) and (b) indicate the isotopes of Yb that would be unstable to collapse due interactions.

2.4 A tunable species-selective trap for Rb and Yb

Given the conditions presented in the previous three sections, the only isotope available for creating a stable, degenerate mixture with ^{87}Rb is the fermion ^{171}Yb. Unfortunately, due to its small s-wave scattering length of $-3a_0$ it cannot be evaporated using our procedures, and must be sympathetically cooled to degeneracy by ^{87}Rb. This requires that the trap depth for ^{171}Yb be larger than the trap depth of ^{87}Rb, and a three-color optical dipole trap (ODT) [38, 39] was developed to achieve this.

An ODT traps atoms by using the AC stark shift (light shift) $U(\mathbf{r}) = -\mathbf{d} \cdot \mathbf{E}(\mathbf{r})$ of an atom, in the presence of a laser beam with an oscillating electric field $\mathbf{E}(\mathbf{r})$. The light shift of the ground state of two-level atom driven by a laser with frequency ω and intensity I is,

$$U_{dip} = \frac{\hbar \Gamma^2}{8} \frac{I}{I_s} \left(\frac{1}{\omega - \omega_0} + \frac{1}{\omega + \omega_0} \right)$$

where Γ, I_s and ω_0 are the linewidth, saturation intensity and frequency of the transition. For any real atom with transitions to multiple excited states (indexed by i), the total light shift is the sum of contributions from all transitions,

$$U_{dip} = \frac{\hbar I}{8} \sum_i \frac{\Gamma^2_{i \to g}}{I_s^{(i \to g)}} \left(\frac{1}{\omega - \omega_i} + \frac{1}{\omega + \omega_i} \right) = \alpha I \tag{2.30}$$

where α is defined as the scalar polarizability of the atom [1]. The Gaussian transverse mode $I(\mathbf{r})$ of a laser beam focused with a waist w_0, gives rise to a spatially varying light shift,

$$U_{dip}(\mathbf{r}, \lambda) = \frac{U_0(\lambda)}{\sqrt{1 + (z/z_R)^2}} e^{-(x^2 + y^2)/w_0^2} \tag{2.31}$$

which can be used as a harmonic trap with a minimum at $(x, y, z) = (0, 0, 0)$ for $U_0 < 0$. The details of all transitions used in the calculation of the light shift U_0 for rubidium and ytterbium are presented in Appendix B and plotted in Fig. 2.5. From this we can see that there are very few wavelengths in the usable range (350–1200 nm) where the $U_0^{(Yb)}$ is negative and larger in magnitude than $U_0^{(Rb)}$. In fact, the only places where this

---

[1]Since we typically operate at detunings much larger than the hyperfine splittings of either atom, the tensor light shift can be neglected and since all our beams are linearly polarized, the vector light shift may also be neglected.
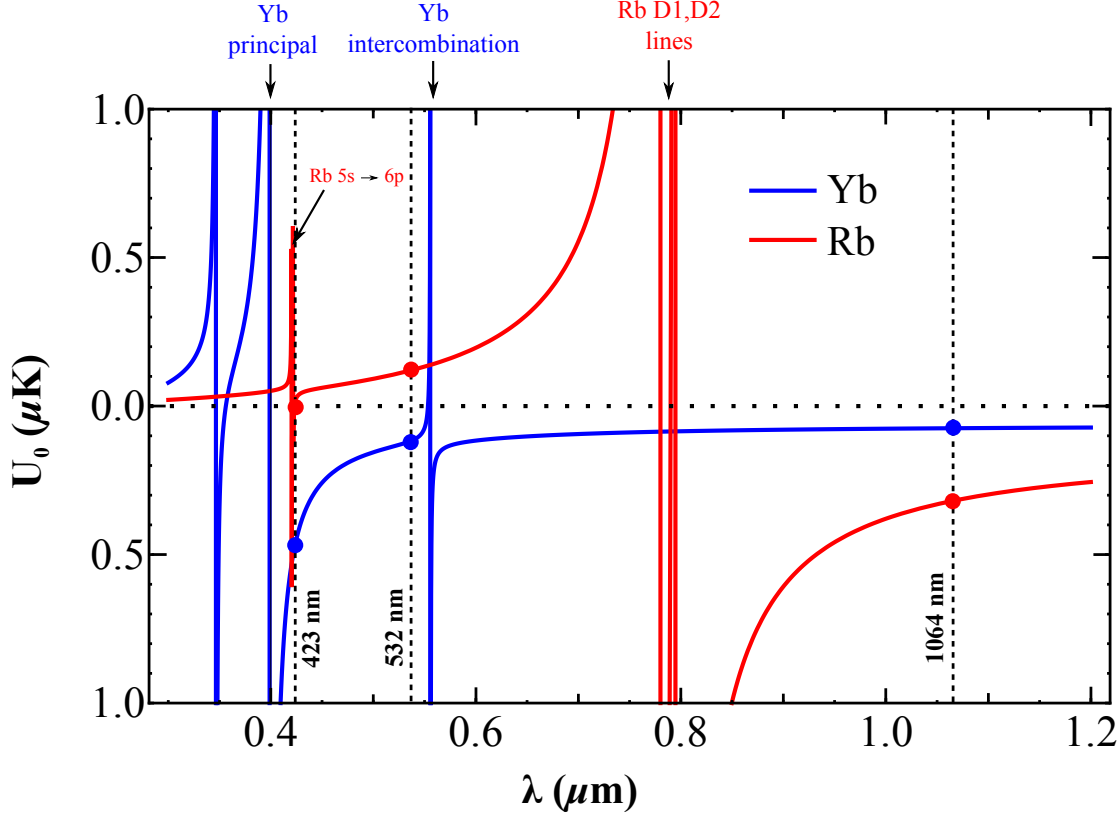
Figure 2.5: Scalar light shifts of the Rb and Yb atom as a function of wavelength. The vertical dotted lines indicate wavelengths of the dipole trap beams. The arrows indicate relevant atomic resonances.

condition is satisfied, is near the Yb atomic resonances where operating an ODT would cause severe heating of the Yb cloud from inelastic photon scattering.

As a result we decided to trap and cool the cloud using a bichromatic optical dipole trap (BIODT), consisting of two beams of 532- and 1064-nm light focused down to an identical and overlapped waists w_0. The 1064-nm (infrared) beam provides a negative light shift for both atoms, creating a trap for both species which is deeper for Rb by a factor of 4.5. However the 532-nm (green) beam provides a positive light shift for Rb, reducing its trap depth, but a negative one of Yb. Therefore by appropriately controlling the power of the green and infrared beam, the ratio of trap depths $U_0^{(\mathrm{Rb})}/U_0^{(\mathrm{Yb})}$ can be tuned over a wide range, allowing us to engineer a trap that will preferentially evaporate rubidium atoms, while sympathetically cooling ytterbium. The geometry of this trap is illustrated in Chapter 3.

In addition, a "tune-out" wavelength at 423 nm is used to provide a species-selective light shift for Yb, which allows us to implement a species-selective lattice potential for Yb as discussed in Chapter 1. The light shift of Rb at this wavelength vanishes due to opposing contributions from the $5s \to 5p$ and $5s \to 6p$ transitions and a precision measurement of this wavelength is presented in Chapter 4. In addition, this wavelength also acts as a crossed-dipole trap and allows us to provide additional confinement for the Yb cloud along the BIODT beams.

The nonmagnetic nature of Yb atoms, allows a quadrupole magnetic trap to provide species-selective confinement for Rb. Atoms pumped into the $|F = 1, m_F = -1\rangle$ state of ^{87}Rb have a magnetic moment $\mu = -m_F \mu_B/2$ and in a magnetic field B, experience a Zeeman shift,

$$U_z = -\mu \cdot \mathbf{B} = \frac{1}{2} m_F \mu_B |\mathbf{B}|$$

proportional to the magnitude of the field. A quadrupole magnetic field with a field gradient B' has a minimum with $|\mathbf{B}| = 0$, which can be used to trap magnetic atoms such as ^{87}Rb. The trap potential for a quadrupole magnetic trap is given by,

$$U_q(\mathbf{r}) = \frac{1}{2} m_F \mu_B B' \sqrt{\frac{x^2}{4} + \frac{y^2}{4} + z^2} \tag{2.32}$$

with the field minimum located at $(0, 0, 0)$. The quadrupole trap is used to provide confinement for Rb along the BIODT beams, and as an added benefit, can also be used to translate the rubidium cloud in order to control the overlap with ytterbium.

Using a combination of the BIODT, tune-out wavelength and quadrupole trap we create a fully tunable, species-dependent trap capable of bringing ^{87}Rb and ^{171}Yb to degeneracy. The following chapters will describe the apparatus used in the implementation of this trap and present data from two experiments - the creation of the degenerate mixture and the precision measurement of the ^{87}Rb $5s \to 6p$ matrix elements through the tune-out wavelength.

Chapter 3: Apparatus

This chapter describes the apparatus used to create degenerate mixtures of rubidium and ytterbium. The setup occupies three optical tables holding the vacuum chamber and the MOT, dipole trap and lattice lasers. The experiment table holds the vacuum chamber where all our experiments are conducted, along with the MOT lasers for ytterbium. Two separate laser tables house the lasers, from which light is sent over optical fibers to the experiment table. In addition, three high-current power supplies and water cooling pumps for the magnetic coils are placed in a closet 8 meters away from experiment chamber to prevent stray magnetic field noise from coupling to the atoms.

The first section will give an overview of the vacuum system consisting of the rubidium and ytterbium ovens, the rubidium slower and the experiment chamber. The second will describe the optics setup near the experiment chamber used for the MOTs, dipole traps and imaging. The third will present the frequency and intensity stabilization of all lasers used on this experiment and the fourth will describe how we control the magnetic fields for the quadrupole and bias coils.

3.1 Vacuum Chamber

The description of the vacuum system is be broken down into three separate sections: the ytterbium source, the rubidium source and the experiment chamber. The rubidium and ytterbium sources provide cold atomic beams to load their respective MOTs, while the preparation of the MOTs and degenerate cold gases takes place in the experiment chamber.

3.1.1 Ytterbium source

The design for the ytterbium source was derived from a similar lithium 2D-MOT source described in [40, 41], since a Zeeman slower for ytterbium would severely restrict the amount of space and optical access available near the experiment chamber. The principle of operation for a 2D-MOT is identical to that of a 3D-MOT with cooling and confinement along one of the three axes removed, resulting in a cold elongated cloud (see Figure 3.1). A cold atomic beam can be derived from a 2D-MOT by using a near-resonant push beam to accelerate atoms along the elongated axis of the MOT, into the experiment chamber. The velocity of atoms leaving the 2D-MOT can be controlled using both the detuning and intensity of the push beam.

The principal transition in ytterbium at 399 nm is used to make the 2D-MOT as its broad linewidth allows for a large capture velocity. Our push beam on the other hand, uses the much narrower intercombination transition at 556 nm which falls out of resonance once the atoms are accelerated to an approximate velocity of 10 m/s from their initial velocity. This allows us to produce a low velocity ytterbium beam that can be efficiently captured into the 3D-MOT operating on the intercombination transition of ytterbium at 556 nm.

The 2D-MOT chamber and ytterbium oven are constructed from a modified six-way Conflat cross shown in Figure 3.1, connected to the experiment chamber. In addition to four viewports for the 2D-MOT beams the cross includes a protruded section for an Ytterbium oven, a differential pumping tube to maintain a pressure differential between the Yb source and experiment chamber and a gate valve to isolate the source from the experiment chamber if needed. The Yb oven, typically operated at 390 °C, was positioned to eliminate line of sight to the 2D-MOT viewports as ytterbium is known to coat windows over time, making them opaque. A magnetic field gradient of 50 G/cm is provided by two pairs of permanent neodymium magnets attached to the sides of the 2D-MOT chamber.

Capture velocities for the 2D-MOT were estimated using standard Doppler cooling theory presented in [42]. The force on a two-level atom exerted by a laser beam with
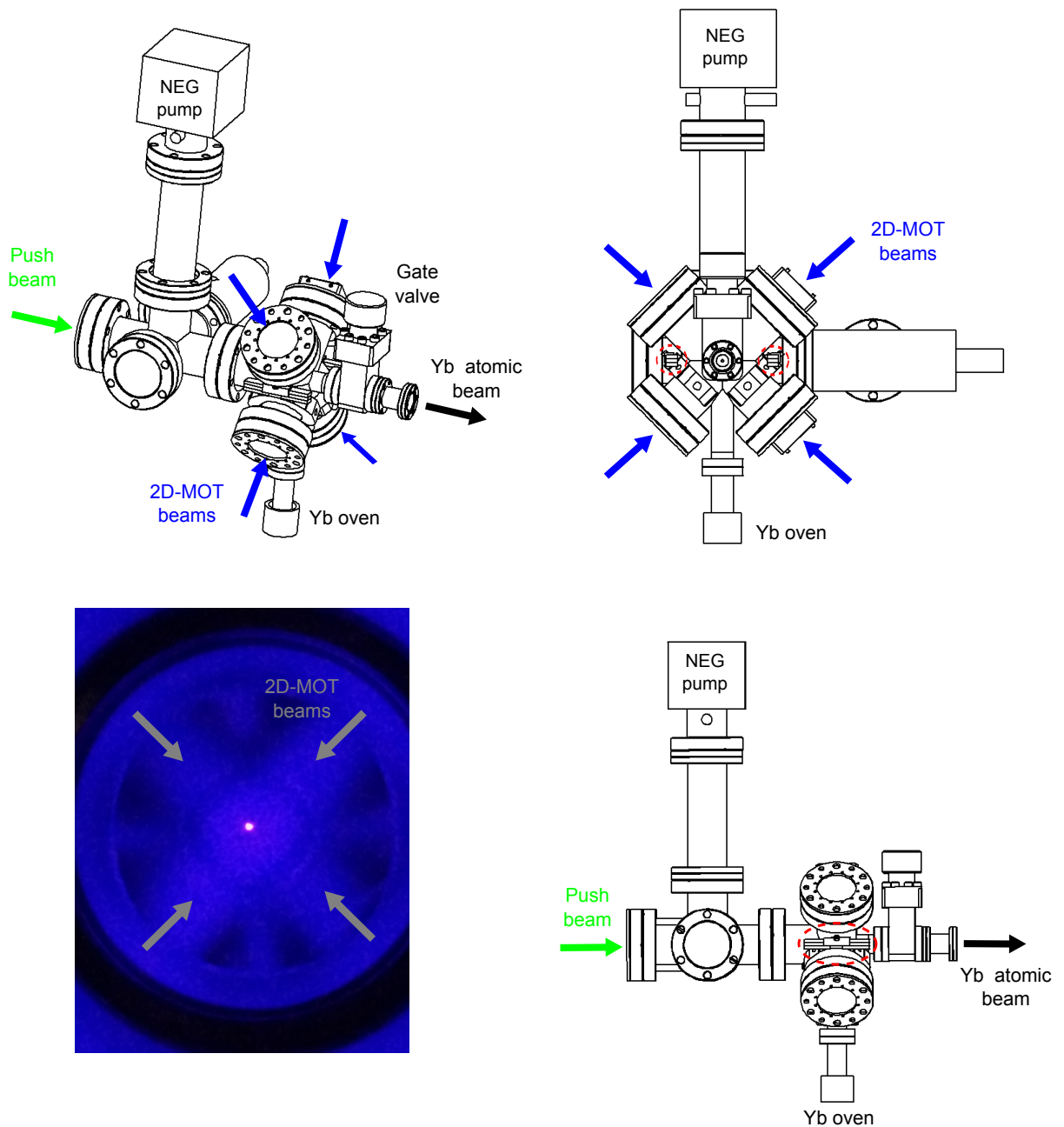
Figure 3.1: An illustration of the ytterbium 2D-MOT chamber. The 2D-MOT beams (blue) create an elongated MOT (bottom left) and the push beam accelerates atoms along the axis of the 2D-MOT, into the experiment chamber. The dotted red circles indicate the permanent magnets used to form the 2D-MOT field. The image on the bottom left shows a view of the 2D-MOT along the direction of the push beam. The bright spot in the center is the 2D-MOT while the diffuse glow is along the arrows is the fluorescence of the 2D-MOT beams.

momentum $\vec{k}$, intensity I and detuning δ is given by,

$$\vec{F} = \hbar \vec{k} \left(\frac{\Gamma}{2} \right) \frac{(I/I_s)}{1 + \frac{I}{I_s} + \left(\frac{2\delta}{\Gamma} \right)^2} \tag{3.1}$$

where Γ is the linewidth of the transition and I_s, the saturation intensity defined by

$$I_s = \frac{\pi \hbar \Gamma c}{3\lambda^3} \tag{3.2}$$

By including the Doppler shift $\delta_D = -\vec{k} \cdot \vec{v}$ of the laser beam and Zeeman shift $\delta_Z = -\mu_B \vec{B}(x)$ induced by the magnetic field gradient, the equations of motion for a ^{174}Yb atom in the 2D-MOT were integrated to estimate MOT capture velocities, shown in Figure 3.2. The calculations presented are for typical experimental parameters with MOT beam intensity of $1.3I_s$, field gradient of 50 G/cm and and a 2D-MOT beam detuning of -50 MHz. While these calculations were performed for ^{174}Yb, they hold true for most of the bosonic isotopes of ytterbium. The operation of the 2D-MOT for the fermions ^{171}Yb and ^{173}Yb, is complicated by the large differential Zeeman splitting between the ground and excited states shown in Fig. 2.1(e). Using ^{171}Yb as an example, a fixed detuning of δ of a σ_+ polarized MOT beam, results in significantly different detunings δ_+ and δ_- for atoms in the $m = +1/2$ and $-1/2$ states respectively, as illustrated in Fig. ??. Consequently, the $+1/2$ atoms feel a weaker trapping potential than the $-1/2$ atoms and the performance of the 2D-MOT degrades significantly for the fermionic isotopes.

An atomic beam produced from the 2D-MOT has a transverse velocity distribution with a calculated Doppler limited width of 0.18 m/s. The longitudinal velocity of the atomic beam can be controlled by the both the intensity and detuning of the 556 nm push beam and we observe efficient loading of the 3D-MOT over a wide range of push beam parameters, though we typically operate with a detuning of $+10$ MHz and intensity of $180I_s$. An atomic beam can be created for both red and blue detunings for push beams operating on both 556 nm and 399 nm transitions. Calculations for beam velocity as a function of push beam detuning are shown in Figure 3.3 for ^{174}Yb. Due to its narrower linewidth, the 556 nm push typically leads to a slower atomic beam velocity than the 399 nm push beam, which requires a very large detuning 150 MHz to be usable. An
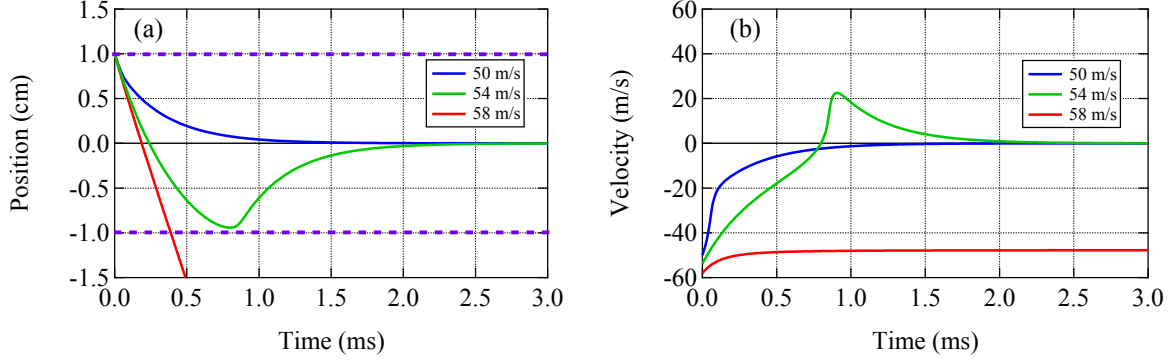
Figure 3.2: Calculated cooling curves for a 2D-MOT of ^{174}Yb operating on the 399 nm transition of Yb in a field gradient of 50 G/cm. In each case, the atom was assumed to start on one edge of a 2 cm MOT beam (dashed purple lines) and its evolution in the presence of two counter-propagating MOT beams was numerically evaluated using Equation 3.1. Note that atoms faster than 54 m/s do not get slowed sufficiently before escaping the MOT beam and hence are not cooled and trapped.

interesting point to note about Fig. 3.3(a) is the kink in the velocity curves for large blue detunings of the push beam. This is caused by the atoms being Doppler-shifted into resonance with the narrow intercombination transition, for a very short time as they are accelerated out of the 2D-MOT.

Typically the 2D-MOT, operating at a MOT beam intensity of $1.3I_s$ and detuning of -50 MHz, can be used to load a ^{174}Yb 3D-MOT in the experiment chamber at a rate of 6×10^7 s^{-1}. The 3D-MOT loading rate for the rest of the bosonic isotopes scales with their natural abundance, but the loading rate for the fermions ^{171}Yb and ^{173}Yb is significantly below what one would expect for their natural abundances, due to the poor performance of the 2D-MOT for these isotopes. With ^{171}Yb we achieve a loading rate of 2.4×10^6 s^{-1} which, while slow does not significantly affect the production of degenerate ^{171}Yb since we can cool it sympathetically, with minimal loss, using ^{87}Rb as a coolant.

3.1.2 Rubidium source

The rubidium source (shown in Figure 3.4) consists of a Zeeman slower which is fed by a rubidium oven heated to 110 °C. The design of the oven is identical to [23], with the exception that the nozzle is loaded with an array of 15 stainless steel hypodermic
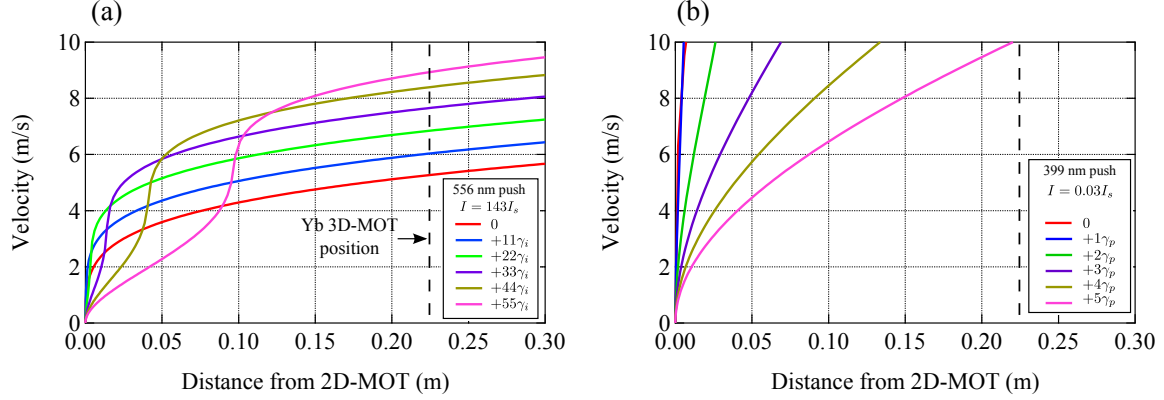
Figure 3.3: The velocity of as a function of position for a Yb atom accelerated from rest by a push beam of different detunings. The calculations for a 556 nm push beam are shown in (a), while those for a 399 nm push beam are shown in (b). The detunings are stated in units of the natural linewidth γ of the relevant transition and the intensisty in units of I_s. The vertical dotted line in both plots indicates the distance to the 3D-MOT, were a beam velocity of approximately 10 m/s is required for efficient loading. Due to the large acceleration provided by a 399 push beam a 556 nm push beam was used, although a 399 nm push with a lower intensity is feasible and has been used in [41].

needles to narrow the transverse velocity distribution of the Rb atomic beam. In order to prevent the needles from clogging during extended (2 days) operation of the oven, the nozzle is permanently held at a higher temperature (140 °C).

The atomic beam leaving the oven has a longitudinal velocity distribution peaked at 300 m/s and enters the Zeeman slower, where it is decelerated to 20 m/s during its 77 cm path to the experimental chamber. The magnetic field gradient along the slower is provided by a pair of opposing coils wound around the slower tube with a spatially varying pitch. The field profile of the slower is designed to allow a far-detuned (-126 MHz) slower laser beam to be used, in order to reduce scattering of the slower laser beam in the Rb MOT. The longitudinal field profile along the slower axis is shown in Figure 3.5 with the typical slowing performance shown in Figure 3.6. In addition to the slower coils, a compensation coil is wound with opposite helicity at the end of the Zeeman slower minimize the field gradient from the Zeeman slower at the position of the MOT.

The data in Figure 3.6 was taken by monitoring the fluorescence of a near-resonant 780 nm probe beam intersecting the Rb atomic beam at $\theta = 45°$, at the exit of the slower.

34

Heated Rb
ampoule

Nozzle

Gate
valve

30.71

⌀2.73

Zeeman slower tube

Rb beam

Collimation
nozzle

Copper
cold-cup

Hypodermic
needle array

Rb beam
shutter
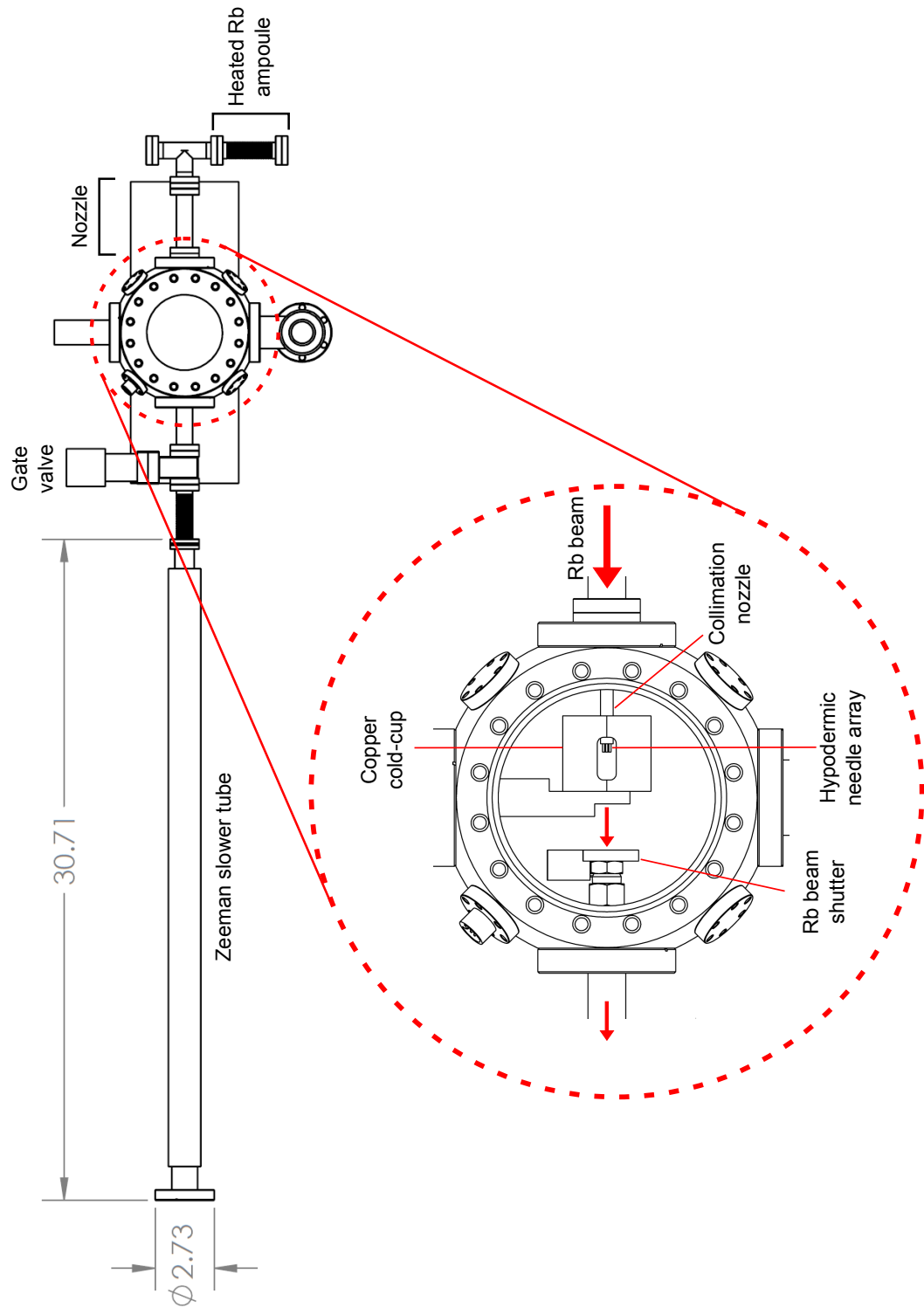
Figure 3.4: The rubidium atomic beam oven and Zeeman slower.
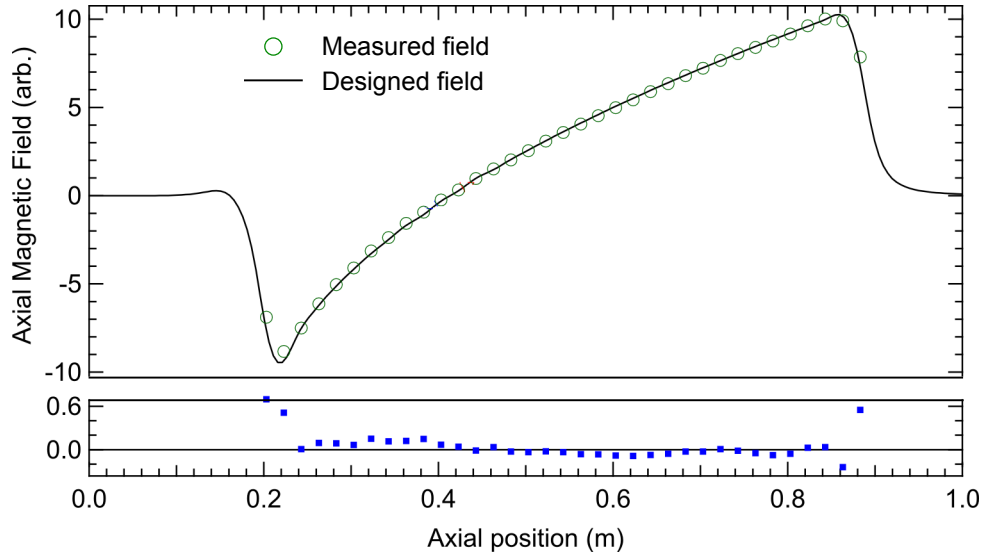
Figure 3.5: The designed and measured axial magnetic field profiles along the length of the slower for 2A running through the slower coils. The lower plot shows the residual between the designed and measured axial field strength.
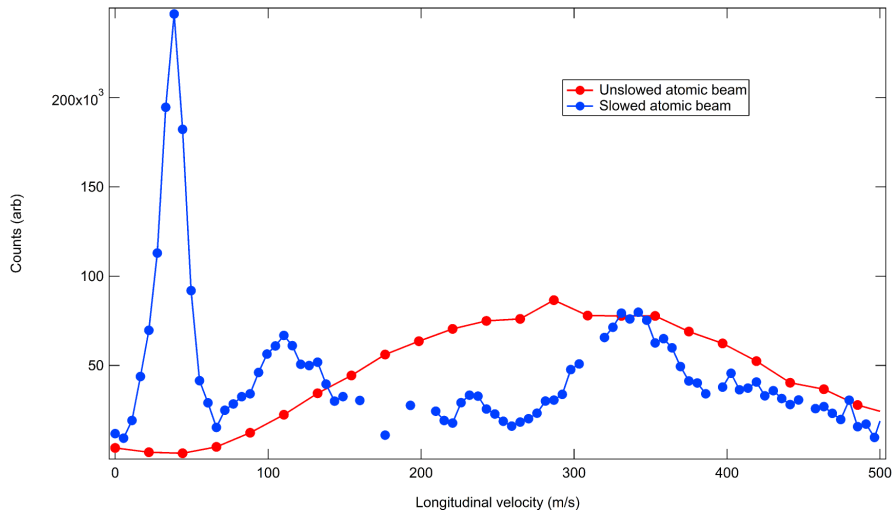
Figure 3.6: The performance of the slower during daily operation. Due to the design of the slower, atoms around 300m/s are decelerated by a factor of 10 to 30m/s while faster atoms are left largely unaffected. As a result the slower carves out a hole in the velocity distribution around 300m/s and creates a tall, low velocity peak at 20m/s which can be efficiently captured in the Rb MOT.

The velocity $\vec{v}$ of the fluorescing atoms along the probe beam's direction was inferred from the probe detuning via the Doppler effect, and a beam velocity distribution was constructed. As shown in Figure 3.6 in the absence of a slower beam, the beam has a peak longitudinal velocity of 300 m/s. With the slower beam on, atoms around 300 m/s are decelerated to 30 m/s resulting in the large, low velocity peak shown in the same figure. While atoms can be captured in a MOT directly from the low velocity tail of a thermal beam, the slower drastically improves the Rb MOT loading rate by a factor of 300 to around 3×10^8 s^{-1} allowing for larger MOTs and faster experimental cycles.

3.1.3   Experimental chamber

Both atomic beam sources feed their respective beams into the experiment chamber, where the MOTs are prepared and evaporative cooling to degeneracy takes place. This section of the vacuum system is maintained at a lower pressure of 10^{-11} Torr to extend BEC lifetimes. In order to accommodate the large number of MOT and dipole beams required for this experiment, this chamber is constructed from an 8-inch spherical square shown in Figure 3.7. The four 4.5" Conflat viewports provide optical access for the Rb MOT beams, Yb MOT beams, the probe beams and the Yb lattice, while a pair of 2.75" viewports are used for the bichromatic optical dipole trap. Each 4.5" viewport has four 1.33" conflat connections around it, one of which is connected to the Yb 2D-MOT chamber. A pair of recessed 8" viewports are used to enclose the top and bottom of the chamber. The quadrupole and vertical bias coils are placed and secured into this recessed viewport in order to get as close to the atoms as possible and achieve a high magnetic field gradient for a given current.

In addition, the front of the chamber has a 4.5" conflat connection to the pumping assembly (Figure 3.8) holding the ion and titanium-sublimation pumps required to maintain a low pressure. Manually operated shutters placed between the experiment chamber and pumping assembly prevent titanium from coating the chamber windows when the sublimation pump is activated. Finally, the Rb Zeeman slower is secured to a 2.75" conflat connection at the rear end of this chamber.
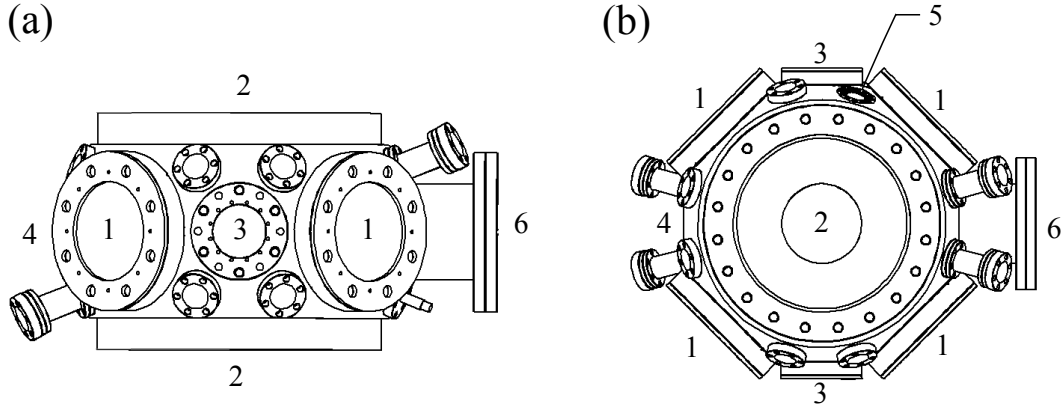
1	4.5" Confat viewports
2	8" recessed viewports
3	2.75" BIODT viewports
4	Connection to Rb Zeeman slower
5	Connection to Yb 2D-MOT
6	Connection to pump assembly

Figure 3.7: A side view (a) and top view (b) of the experiment chamber. All dimensions are in inches.

3.2   Experiment table optics

The optical setup near the experiment chamber (See Figure 3.9) consists of MOT beams for Rb and Yb (780 and 556 nm), imaging systems along the Y'Z and XY planes, mode-matching optics and intensity stabilization for the bichromatic optical dipole trap (BIODT) beams (1064 and 532 nm) and finally optics for the magic wavelength cross-dipole and lattice beams (423 nm). Due to the large number of wavelengths used in this experiment, special care had to be taken to ensure efficient usage of the limited optical access available on the experiment chamber.

In particular the MOT and recessed viewports needed to transmit the Rb MOT and probe beams at 780 nm, the Yb MOT beams at 556 nm, the Yb probe beam at 399 nm and the lattice beam at 423 nm. In addition, imaging of trapped Rb and Yb clouds with a resolution of 2 μm or better was required along two orthogonal directions
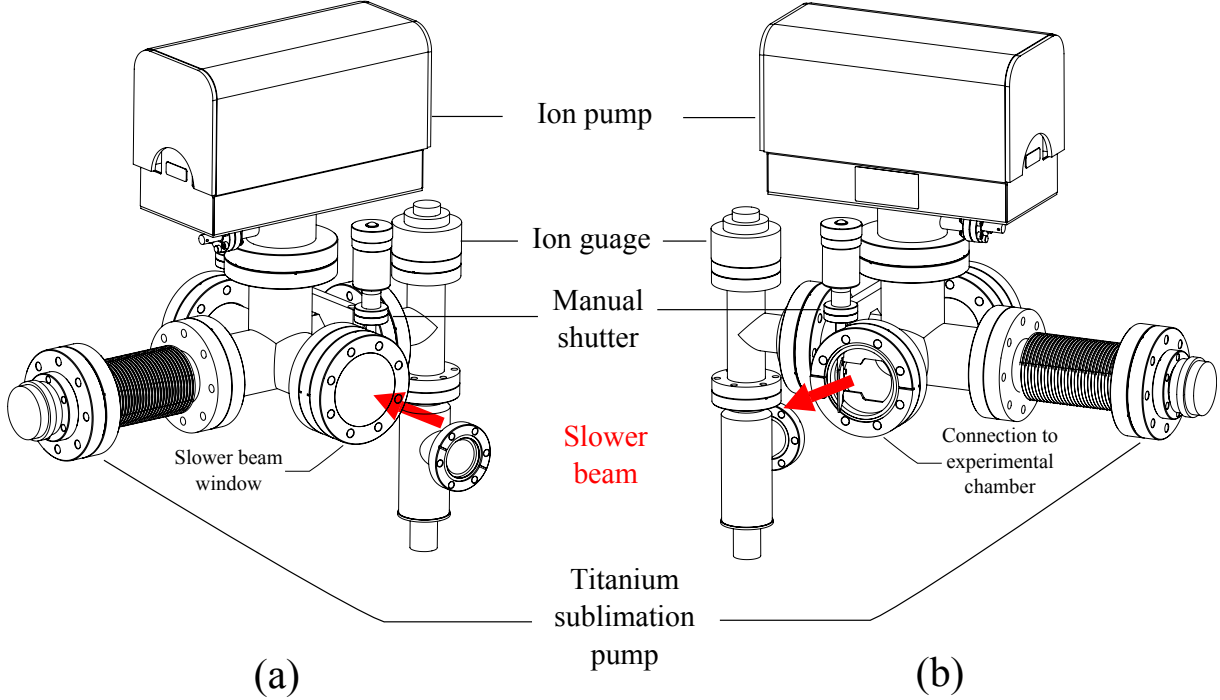
Figure 3.8: Front (a) and rear (b) views of the pumping assembly attached to the experiment chamber. A 60 L/s ion pump in conjunction with a titanium sublimation pump can maintain pressures as low as 3×10^{-11} Torr. The sublimation pump is mounted on bellows to allow the pump to be retracted from the line of slight of the slower beam, when not in use.

for precise and repeatable alignment of the 27 μm waist BIODT beams. The optical setup currently in use near the experiment chamber is illustrated in Figure 3.9. The remainder of this section will refer heavily to this illustration. The horizontal plane (XY in Fig. 3.9) holds the optics for the bichromatic trap, lattice and horizontal 3D-MOT beams as well as a lens system for imaging Rb and Yb atoms in the vertical (Y'Z) plane. The vertical plane (YZ) holds optics for the vertical MOT beams and imaging in the XY plane.

3.2.1   3D-MOT optics

The 780 nm MOT beams for Rb are fiber-coupled to the experiment table while the 556 nm beams for Yb are sent over free-space from the laser located on the experiment table. In order to increase the capture volume of the Rb and Yb 3D-MOTs, the 780 nm
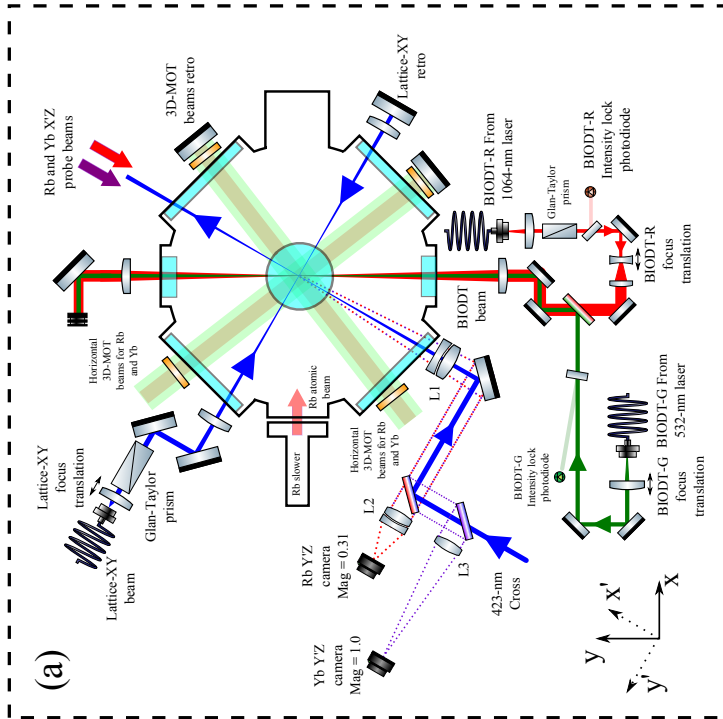
Figure 3.9: Schematic of the optical setup near the experiment chamber. The solid lines represent various MOT and trapping lasers while the dotted lines represent the imaging paths. The table in (d) shows the calculated resolution of each imaging system. The calculation was performed by raytracing in OSLO and takes into account all aberrations present in the imaging lenses.

40

and 556 nm 3D-MOT beams were designed to be 2" in diameter and are combined on the dichroic beamsplitter before being sent to the vacuum chamber. A dichroic quarter-waveplate (QWP) placed just before the chamber windows ensures that both MOT beams have the appropriate circular polarization before entering the vacuum chamber. The dichroic QWP performs a $\lambda/4$ rotation at 780 nm but a $3\lambda/4$ rotation at 556 nm. Hence the MOT beams need to have *orthogonal* linear polarizations prior to the QWP in order to have the same circular polarization inside the chamber.

In the horizontal plane, all MOT beams are retroreflected through a second dichroic QWP attached outside the opposite side of the chamber. The situation in the vertical plane is complicated by the fact that the beams need to propagate downwards through the XY imaging optics, some of which cause significant loss at 780 nm. As a result the 556 nm Yb MOT beam is retroreflected through the XY imaging setup while a separate upwards-propagating Rb MOT beam is used.

3.2.2   Imaging and data analysis

The Rb and Yb clouds are probed using the absorption imaging technique where the transmission of a probe beam through the atomic cloud is measured on a CCD. The intensity $I(x,y)$ of a probe beam passing through a cloud with a spatial density distribution $n(x,y,z)$, is given by the Beer-Lambert law,

$$I(x,y) = I_0(x,y) \exp\left(-\int \sigma(I,\delta)n(x,y,z)dz\right) \tag{3.3}$$

where I_0 is the probe intensity before the cloud and σ is the photon scattering cross-section for an atom, which in the general case is determined by the I_0 and the probe beam detuning δ,

$$\sigma(I,\delta) = \frac{3\lambda^2/2\pi}{1 + \frac{I_0}{I_s} + \frac{4\delta^2}{\Gamma^2}} \tag{3.4}$$

However in the limit of a weak ($I_0 \ll I_s$) resonant ($\delta = 0$) probe beam, the cross-section is independent of intensity and detuning. In this regime the probe transition is unsaturated and one can infer the column density $n_2(x,y)$ of the cloud along the

propagation direction of the probe beam,

$$n_2(x,y) = \int \sigma_0 n(x,y,z)dz = -\frac{1}{\sigma}\log\frac{I(x,y)}{I_0(x,y)} = -\frac{1}{\sigma_0}\log OD(x,y) \qquad (3.5)$$

where $OD(x,y)$ is the optical depth of the cloud and $\sigma_0 = 3\lambda^2/2\pi$ for a two-level atom with a transition wavelength λ. In practice $OD(x,y)$ is calculated by dividing an absorption image $I(x,y)$ containing the atomic cloud by a probe image $I_0(x,y)$ without an atomic cloud, and in the unsaturated regime $OD(x,y)$ is independent of the probe intensity.

The Rb cloud is probed on the $F = 2 \to F' = 3$ transition of the D2-line at 780 nm while the Yb cloud is probed on the 399 nm transition due to its larger saturation intensity compared to the 556 nm line. Simultaneous, diffraction limited imaging of both Rb and Yb clouds was required, but doing so with a single imaging system is a challenge as most lenses have very strong chromatic aberrations between 399 nm and 780 nm. Hence, four separate imaging systems were designed to image each cloud in two orthogonal directions (Y'Z and XY) as shown in Fig. 3.9. The Rb and Yb images along each direction share a common objective lens to collect light from the atoms, but have separate image lenses to form an image on the two CCDs. The two images in each direction are separated onto two separate cameras using longpass dichroic beamsplitters with an edge at 540 nm. The aberrations and resolutions of each of the four imaging systems were simulated by raytracing in OSLO and characterized offline using a USAF resolution test chart. A schematic of each imaging direction is illustrated by the dotted lines in Fig. 3.9(a) and Fig. 3.9(b) and a description of the lenses used, along with the measured imaging resolution is presented in 3.9(c)and 3.9(d).

3.2.2.1 Thermal gases

The number of atoms N in an absorption image may be obtained by numerically integrating over the column density distribution $n_2(x,y)$ of atoms in the image.

$$N = \int n_2(x,y)\mathrm{d}x\mathrm{d}y \qquad (3.6)$$

The temperature of a thermal cloud can be extracted using the time-of-flight (TOF) technique where a cloud, initially trapped at $t = 0$, is released from the trap and allowed

to undergo ballistic expansion for a long time t before an absorption image is taken. For a sufficiently large t, the fastest atoms travel to the edge of the cloud while the slowest ones remain in the center. As a result, the long TOF image $n_2(x, y, t)$ represents the velocity distribution of the cloud, from which one can extract a temperature. For a thermal gas, the velocity distribution is a Gaussian and the temperature may be extracted by fitting a two-dimensional Gaussian of the form,

$$n_2(x, y, t_{TOF}) = n_0 \exp\left(-\frac{(x-x_0)^2}{w_x^2} - \frac{(y-y_0)^2}{w_y^2}\right) \tag{3.7}$$

to the TOF image. The free-fit parameters are the peak density n_0, the centers (x_0, y_0) and the Gaussian waists (w_x, w_y). Comparing this to the Boltzmann velocity distribution for a thermal gas, we obtain expressions for the temperature in the x- and y-directions

$$T_i = \left(\frac{w_i}{t}\right)^2 \sqrt{\frac{m}{2k_B}} \tag{3.8}$$

which are then averaged to report a cloud temperature $T = (T_x + T_y)/2$. The long time-of-flight assumption holds on timescales much longer than a trap period and is almost always valid in all our measurements since our trap frequencies are large. Under typical conditions, our trap frequencies are $\omega = 2\pi 100$ Hz and time-of-flight larger than 15 ms are large enough to ensure that our images are always in the long TOF regime.

3.2.2.2 Fermi gases

The velocity distribution of a degenerate Fermi gas is given by Eqn. 2.6 and may be integrated along the imaging direction z, to obtain a two-dimensional velocity distribution that corresponds to the TOF image,

$$n_2(p_x, p_y) = -(2S+1)\left(\frac{\sigma_T}{h}\right)^2 \frac{\sigma_T}{\lambda_T} \mathrm{Li}_2\left\{e^{[\mu - (p_x^2 + p_y^2)/2m]/k_B T}\right\} \tag{3.9}$$

Unlike a classical thermal cloud, the peak density of this distribution is no longer temperature independent and cannot be used as an independent fit parameter. In order to overcome this issue, we fit a normalized Fermi-Dirac distribution of the form,

$$n_2(x, y) = n_0 \frac{\mathrm{Li}_2\left\{\mathcal{Z}e^{-(x-x_0)^2/w_x^2}e^{-(y-y_0)^2/w_y^2}\right\}}{\mathrm{Li}_2\left\{\mathcal{Z}\right\}} \tag{3.10}$$

43

with an additional fit parameter called the fugacity $\mathcal{Z} = e^{\mu/k_B T}$, which determines the deviation of a Fermi-Dirac distribution from a Gaussian, and is a measure of the degeneracy of Fermi gas. A comparison between a Gaussian and various Fermi-Dirac momentum distributions at the same temperature is illustrated in Fig. 3.10(a). For a fixed temperature, the Fermi-Dirac distributions with a larger $\mathcal{Z}$ correspond to a cloud with a larger number and lower effective temperature T/T_F.

Qualitatively, the momentum distributions for a deeply degenerate Fermi gas ($\mathcal{Z} \gg 1$) look almost identical to a Gaussian allowing us to use one dimensional Gaussian fits, along the horizontal and vertical slices of the image, to retrieve initial guesses for the fit parameters x_0, y_0, w_x, w_y and n_0. Performing a full two-dimensional fit of Eqn. 3.10 using these initial guesses leads to a reliable convergence of the "waists" w_i and fugacity $\mathcal{Z}$. We have implemented the two-dimensional Fermi-Dirac fit using a nonlinear least squares routine written in MATLAB. The absolute temperature of the Fermi-gas is inferred using Eqn. 3.8, where w_i are extracted from the Fermi-Dirac fit instead of a thermal fit. In the case of a deeply degenerate Fermi gas, the effective temperature may be extracted as $T/T_F = 1/\ln(\mathcal{Z})$ since $\mu(T = 0) = \epsilon_F$.

3.2.2.3 Bose gases

Extracting the temperature of a degenerate Bose gas is a more involved procedure since it undergoes a phase transition at the critical temperature T_c. Below this temperature, the equilibrium distribution consists of a degenerate thermal component described by the Bose-Einstein distribution and a condensate described by the Thomas-Fermi profile described in Chapter 2. While time-of-flight expansion of the thermal component is ballistic, repulsive interactions in the dense condensate cause it to expand hydrodynamically [43]. In an anisotropic harmonic trap, the tightly trapped directions expand faster than the weak ones resulting in a self-similar expansion of the Thomas-Fermi profile.

$$n_{TF}(x, y, z, t) = n_0 \left(1 - \frac{x^2}{(\lambda_x(t)R_x)^2} - \frac{y^2}{(\lambda_y(t)R_y)^2} - \frac{x^2}{(\lambda_z(t)R_z)^2} \right) \qquad (3.11)$$

The Thomas-Fermi radii R_i of the condensate are rescaled in time by a scale factor $\lambda_i(t)$ which depends on the trap frequency ω_i, condensate number N_0 and s-wave scattering
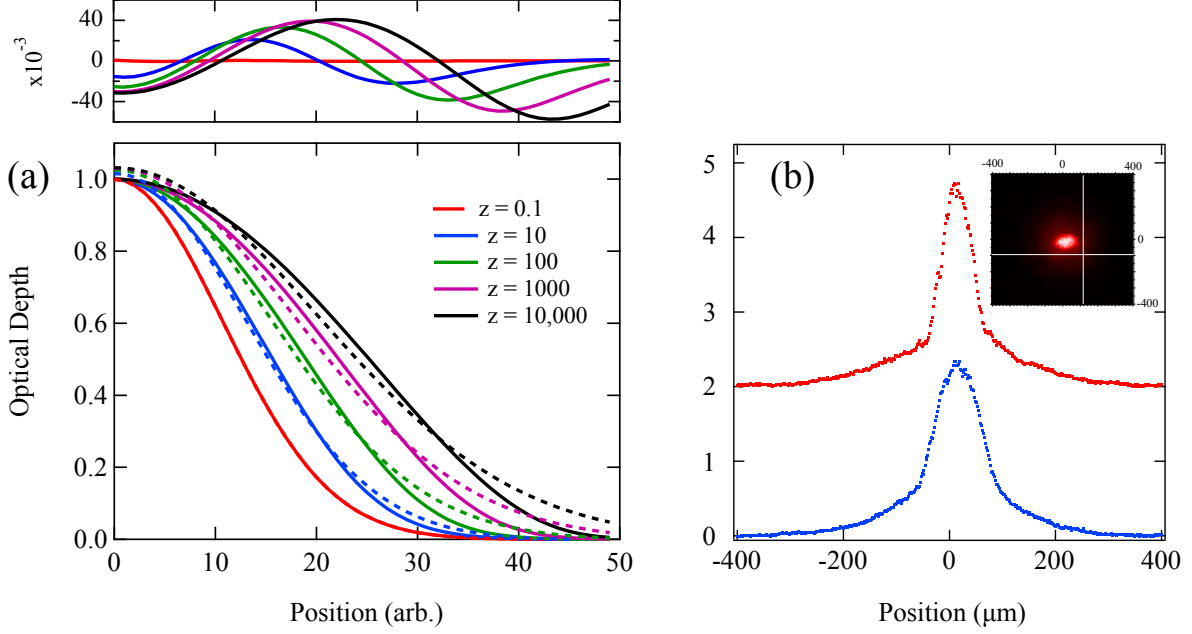
44

Figure 3.10: (a) Generated radial profiles of the TOF images of degenerate Fermi gases for various fugacities. The dotted lines show the result of fitting a Gaussian to the Fermi-Dirac distributions, and the fit residuals are displayed on the plot on top. For low fugacities (non-degenerate clouds), the Gaussian is indistinguishable from Fermi-Dirac distribution and starts to deviate for higher fugacities. (b) A sample TOF image of a ^{87}Rb BEC. The red and blue profiles are slices through the center of the cloud in the x- and y-directions, showing the bimodal distributions. The white lines in the inset indicate the location of the initial guesses.

length a_s. An image of the density distribution of a ^{87}Rb BEC in time-of-flight is shown in Fig. 3.10(b) with a slice along the x-direction in Fig. 3.10(c). The distribution is bimodal with the central feature displaying a Thomas-Fermi distribution, while the wings display the thermal Bose-Einstein distribution presented in Chapter 2. A temperature may be extracted by fitting a bimodal distribution of the form,

$$
n_2(x,y) = \begin{cases} n_0\left(1 - \dfrac{x^2}{R_x^2} - \dfrac{y^2}{R_y^2}\right) + n_{th}\mathrm{Li}_2\left\{-e^{-x^2/w_x^2}e^{-y^2/w_y^2}\right\} & \text{if } \dfrac{x^2}{R_x^2} + \dfrac{y^2}{R_y^2} < 1 \\ n_{th}\mathrm{Li}_2\left\{-e^{-x^2/w_x^2}e^{-y^2/w_y^2}\right\} & \text{if } \dfrac{x^2}{R_x^2} + \dfrac{y^2}{R_y^2} \geq 1 \end{cases} \quad (3.12)
$$

to the TOF image with w_i, R_i, n_0 and $n_t h$ as free fit parameters. Inside the Thomas-Fermi radii, the distribution is a sum of a Thomas-Fermi distribution for the condensed gas and a thermal Bose-Einstein distribution for the uncondensed gas.

The bimodal distribution of a BEC deviates strongly from a simple Gaussian and

45

a two-step fitting procedure is required. Initially a one-dimensional Gaussian fit is performed on slices of the thermal cloud, well outside the Thomas-Fermi radius (see Fig. Fig. 3.10(b)). The initial fit provides a guess for the cloud centers x_0, y_0, "waists" w_x, w_y and thermal cloud amplitude n_{th}. Using these as initial guesses, a two-dimensional fit of Eqn. 3.12 provides values for the condensate peak density n_0 and Thomas-Fermi radii R_i, as well as corrected values for the waists w_i and the thermal cloud density n_{th}. The number of BEC atoms is inferred from the Thomas-Fermi fit, while the temperature of the cloud is extracted from the parameters w_i of the Bose-Einstein fit.

3.2.3 BIODT beams

Light for the BIODT is fiber-coupled on seperate fibers, from the 532 nm and 1064 nm lasers to the experiment table. The outputs of both the 1064 nm and 532 nm fibers are overlapped using a dichroic beamsplitter and focused down to give a waist of 27 μm at the location of the atoms, as shown in Figure 3.9. Both beams are aligned at an angle of 4° with respect to the chamber windows in order to avoid weak backreflections creating a lattice at the location of the atoms. The final lens is a 250 mm plano-convex lens shared by both beams, with a strong chromatic focal shift of 2 mm between the two wavelengths. The chromatic shift can be eliminated to under 20 μm by slight defocusing of one of the two beams before the final 250 mm lens. The change in waist size from the 2 mm translation is negligible and therefore the defocusing method serves as a fine control of the relative longitudnal positions of the two waists. The power in each BIODT beam is monitored by photodiodes on the experiment table, and actively stabilized by feeding back to acousto-optic modulators (AOMs) placed before the fiber inputs.

While our first attempts at the bichromatic trap involved the 532 nm light sent to the chamber over free space, I soon realized that this configuration was not viable since the AOM used to control the beam intensity, alters the TEM_{00} spatial mode out of the laser and results in poor overlap between the red and green trap beams. The long path length from the Verdi to the chamber further complicated trap alignment as the position of 532 nm beam drifted significantly with thermal expansion of mirror mounts. Fiber-coupling the BIODT beams solves both these issues as the single-mode

fiber acts a mode filter to provide a clean TEM_{00} spatial mode and significantly shortens the free-space path length. Large mode-area photonic bandgap fibers (NKT photonics, LMA-PM-10) were used in order to handle the large powers typically used to create the dipole trap. Up to 5 W of light at each of the BIODT wavelengths is available at the output of each fiber.

We have also considered using a single photonic bandgap fiber to carry both wavelengths to the experiment table and using parabolic mirrors, instead of lenses, to focus the BIODT beams inside the chamber. The mode-diameter of the LMA-PM-10 fiber is wavelength-independent and achromatically imaging the tip of the fiber onto the atoms ensures that the waists of the 532 nm and 1064 nm beams are perfectly matched. Furthermore, since both BIODT beams share the same optical path between the fiber and the atoms, drift between the relative alignment of the two beams should be minimized in this configuration. While we were able to achieve stable, drift-free alignment using this method, an anomalous focal shift of 210 μm was consistently measured between the 532 nm and 1064 nm beams. While this focal shift was extremely small compared to the 250 mm focal length of the parabolic mirror, it would have been large enough to significantly reduce the thermal overlap between ^{87}Rb and ^{171}Yb and hence this method for creating the BIODT was not used.

3.2.4   Lattice beams

Light from a pair of 423 nm lasers (Toptica TA-SHGpro) is used to create a Rb-blind crossed dipole trap *and* a two-dimensional lattice for Yb in the XY-plane. Each of the 423 nm beams is focused to a waist of 50 μm near the atoms. During evaporation, the Lattice-XY beam is turned off and the cross beam provides confinement for Yb along the Y-direction. After evaporation a two-dimensional lattice for Yb, with basis vectors $\hat{\mathbf{x}}'$ and $\hat{\mathbf{y}}'$, may be created by increasing the power in the Lattice-XY beam. Alternatively, a one-dimensional lattice along Y can be created by blocking the retroreflection mirror for the Lattice-XY. Up to 90 mW of light is available out of the cross beam fiber and 40 mW out of the Lattice-XY fiber.

3.3   Lasers

3.3.1   780 nm lasers for rubidium

As described in the previous chapter, laser cooling of rubidium-87 requires lasers for both the $F = 2 \rightarrow 3'$ cycling and the $F = 1 \rightarrow 2'$ repumping transitions. The two transitions are separated by 6.835 GHz and have linewiths of around 6 MHz and therefore cannot be simultaneously addressed by a single laser. Light from our cooling laser (Toptica DLpro) drives the $F = 2 \rightarrow 3'$ cycling transition while the repumper laser (Toptica DLpro) drives the $F = 1 \rightarrow 2'$ transition. In addition, a third master laser (Newport Vortex II) locked to a Doppler-free ^{85}Rb absorption line serves as a stable frequency reference for stabilization of cooling and rempumper lasers. When stabilized, all our 780 nm lasers have linewidths under 300 kHz.

Beams from all three 780 nm lasers are combined on a single mode optical fiber splitter to obtain three beat frequencies: the master-cooling ($\approx$ 5.5 GHz), master-repump ($\approx$ 1.1 GHz) and cooling-repump ($\approx$ 6.6 GHz) beatnotes. The output of the splitter is incident on a fast photodetector (Hamamatsu G4176-03) with a bandwidth high enough to resolve the master-cooling and master-repumper beat frequencies. The two lasers are then locked to the master by stabilizing the two beat frequencies to the outputs of a low-noise direct digital synthesizer (DDS). This scheme allows us to tune the frequencies of the cooling and repumper in a controlled fashion by changing the frequency of the DDS output. Figure (3.11) shows a schematic of the locking scheme and gives an indication of the frequency of each laser beam with respect to the cooling and rempumper transitions of rubidium-87.

On the chamber table the Rb MOT beams are made by combining the cooling and repumper light from their respective fibers and splitting them equally into three beams using a fiber splitter. The slower beam and slower repumper are combined after their fibers using a polarizing beamsplitter. Enclosing the laser systems in black PVC cases and placing computer controlled shutters before the fibers prevents stray resonant photons from causing spin-flips in the quadrupole trap and drastically improves the trap

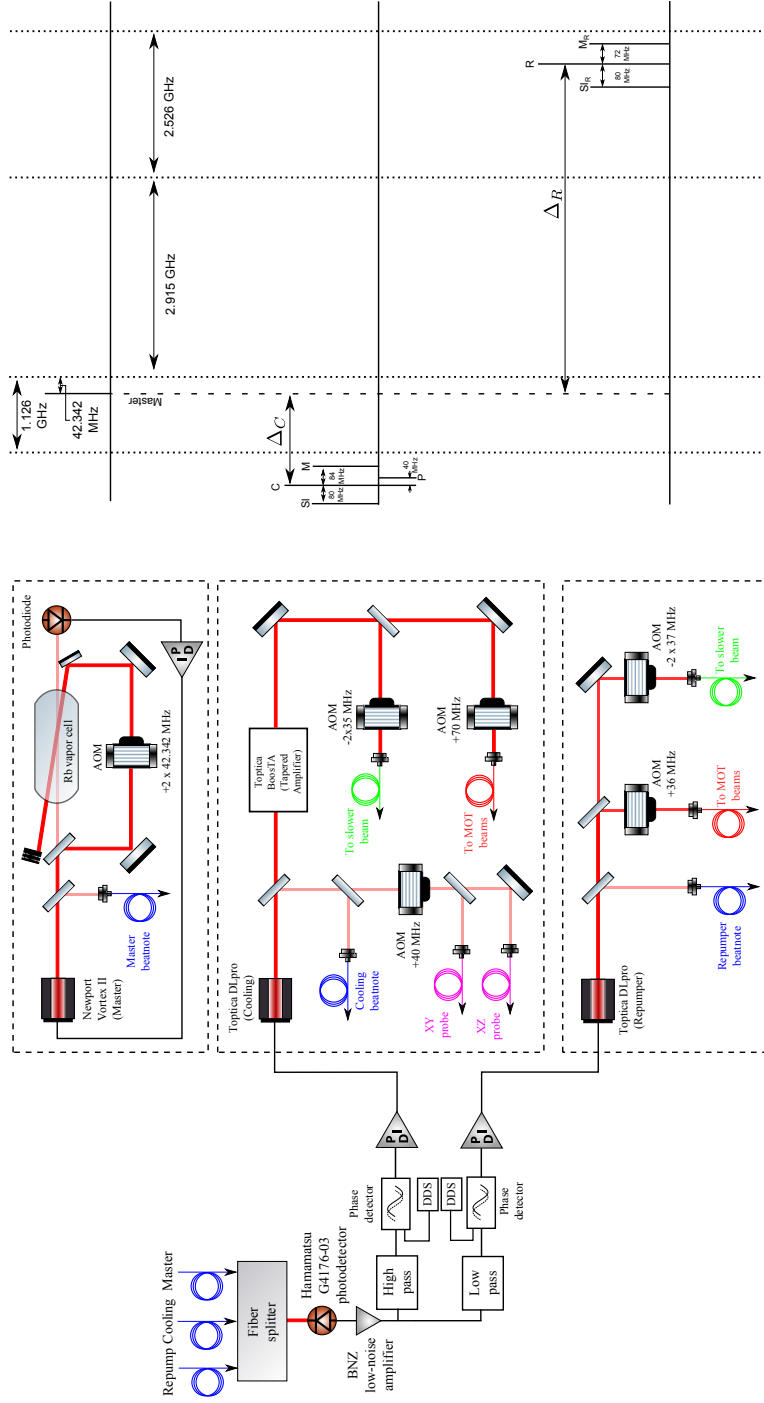Figure 3.11: Schematic of 780 nm laser setup. The cooling and repumper laser frequencies are labeled by C and R respectively. The frequency difference between the master and cooling (rempump) is labeled by $\Delta_{C(R)}$ and is controlled through the DDS. Sl, M and P denote the frequencies of the Slower, MOT and probe beams while Sl_R and M_R denote the frequencies of the slower and MOT repumpers.

49

lifetime.

3.3.2   399 nm laser for ytterbium

The broad linewidth of the $^1S_0 \rightarrow {}^1P_1$ transition provides an efficient way to slow and capture atoms from a high velocity thermal source into a 2D MOT. Up to 300 mW of light for this transition is generated by a frequency-doubled 798 nm diode laser (Toptica TA-SHG pro) and is stabilized to a Doppler-free absorption line in an Yb hollow cathode lamp running at 200 V. An error signal for locking the frequency of this laser is generated using a modulation-free method [44, 45] that relies the birefringence of a spin-polarized atomic gas. A schematic for the implementation of this lock is shown in Fig. 3.12(a) along with the error signal generated for locking to the atomic transitions in Fig. 3.12(c).

The circularly polarized (σ_+) pump beam saturates the $|^1S_0, m\rangle \rightarrow |^1P_1, m' = m + 1\rangle$ transition of Yb, in addition to polarizing the gas for the fermionic isotopes ^{171}Yb and ^{173}Yb in the direction of its propagation z. The horizontally polarized, counter-propagating probe beam may be expressed as a linear combination of the two circular polarizations σ_+ and σ_-.

$$\mathbf{E}_{probe}^{in} = \frac{1}{\sqrt{2}} \left(\mathbf{E}_+ + \mathbf{E}_- \right) \tag{3.13}$$

For the fermionic isotopes such as ^{171}Yb, the σ_+ and σ_- transitions do not have equal Clebsh-Gordon coefficients (see Fig. 3.12(b)) and the two components of the probe beam acquire different phases ϕ_+ and ϕ_-,

$$\phi_{+(-)} = (\text{CG}_{+(-)}) * \text{OD}_0 \frac{2\delta/\Gamma}{1 + \left(\frac{2\delta}{\Gamma}\right)^2} \tag{3.14}$$

as it traverses through the spin-polarized Yb vapor. $CG_{+/-}$ are the Clebsch-Gordon coefficients of their respective transitions, OD_0 is the resonant optical depth of the Yb vapor and δ is the detuning of the laser from resonance. The differential phase shift $\Delta\phi = \phi_+ - \phi_-$, changes its sign on resonance and it can therefore be used as an error signal to stabilize the 399 nm laser. $\Delta\phi$ is measured by analyzing the polarization of the probe beam using PBS and HWP3 shown in Fig. 3.12(d).

MOTs made on this transition require large amounts of optical power due to its high saturation intensity, which scales linearly with the linewidth as shown in Eqn. 3.2.

To eliminate fiber coupling losses, MOT light from the 399 nm laser is sent to the 2D-MOT chamber over free space, while light for the two probe beams is coupled over two fibers. A schematic of the 399 nm laser system is shown in Figure 3.12. While Yb does not suffer from spin-flip losses like Rb in a quadrupole trap, stray 399 nm photons hitting the dipole trap can still cause slow heating of the cloud, resulting in inefficient evaporation. Hence, a shutter is placed on the 2D-MOT beams to prevent any light from reaching the experiment chamber once the dipole trap is loaded and evaporation begins.

3.3.3   556 nm laser for ytterbium

The narrow $^1S_0 \rightarrow^3 P_1$ transition has a low Doppler cooling limit of 4 μK and allows for the creation of cold, high density MOTs which can be efficiently loaded into dipole traps. Laser light at 556 nm is provided by a doubling an 1112 nm fiber laser (Menlo Orange One) in a periodically-poled lithium-niobate waveguide. The frequency of this laser is stabilized to a homebuilt ytterbium vapor cell heated to 550C (see Fig. 3.13). The vapor cell is constructed from 12" long 1-1/3" tube with Conflat flange connectors at both ends. BK-7 windows are glued at Brewster's angle (55°) on both ends of the tube using Torr-seal. While the Brewester's angle maximizes transmission of light through the cell window (0.4% reflection), it is not necessary of proper operation of the cell. However, any small angle between the two windows prevents etaloning of a transmitted laser beam and improves the quality of the absorption signal. 3 grams of ytterbium are placed in the center of the cell and the cell is evacuated, before being filled with 10 mTorr of helium. The helium serves as an inert buffer gas to drastically reduce the mean free path of atoms in the ytterbium vapor and prevents them from migrating to and coating the cell windows.

The absorption signal of our first vapor cell disappeared after one continuous day of use, which we attributed to impurities from the helium buffer gas and the cell walls, reacting with the ytterbium to creating an oxide layer on its surface. During the construction of our second cell, we initially baked the cell at 150°C without ytterbium in order pump out impurities from the cell walls using a turbo pump. Following the bake,
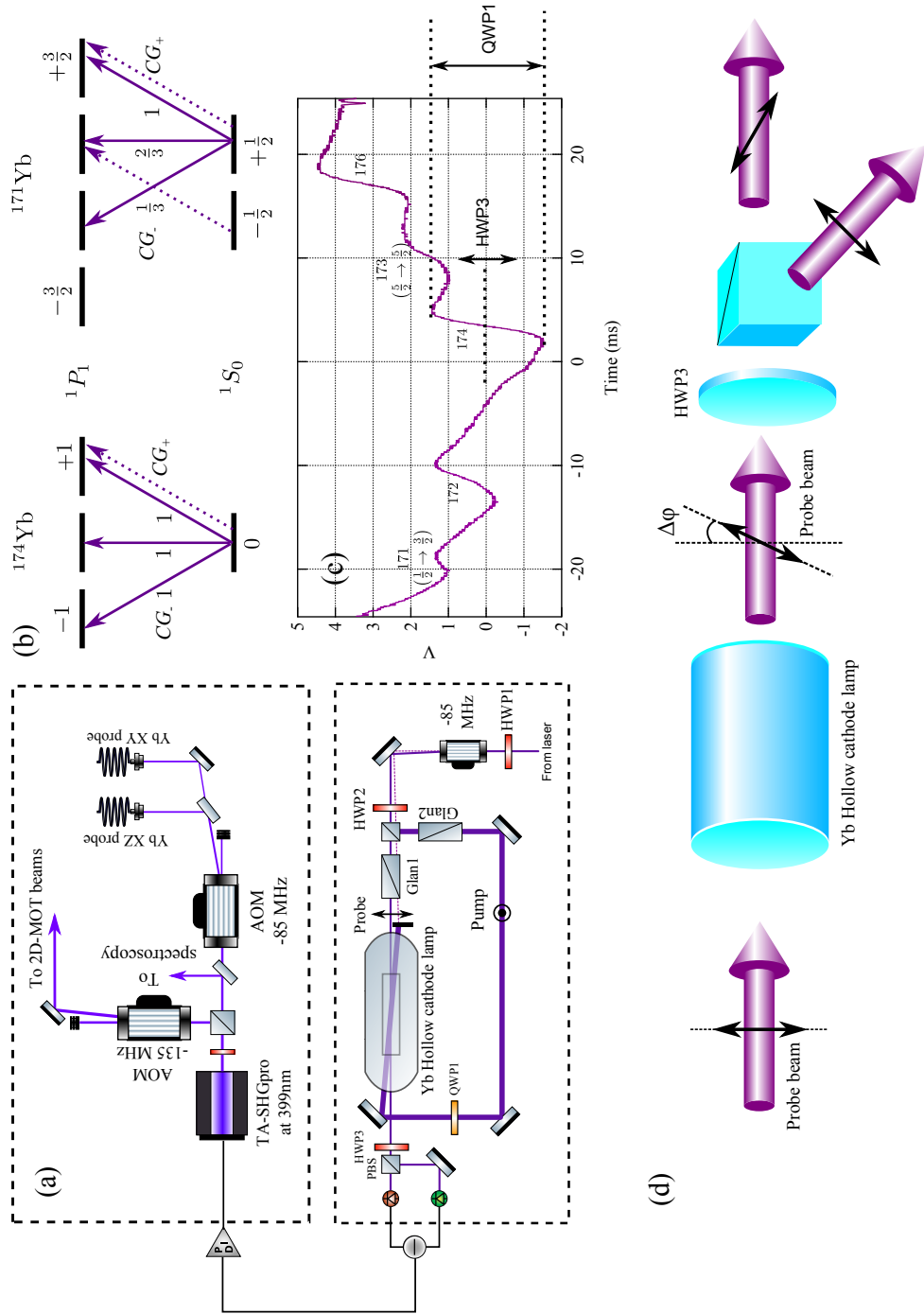
Figure 3.12: Schematic of 399 nm laser setup. The laser is locked 100 MHz above the $^1S_0 \rightarrow ^1P_1$ transition and downshifted to -35 MHz for the 2D-MOT beams and 0 MHz for the two probe beams. The 2D-MOT beams are sent over free space to the 2D-MOT chamber while both probe beams are fiber-coupled.
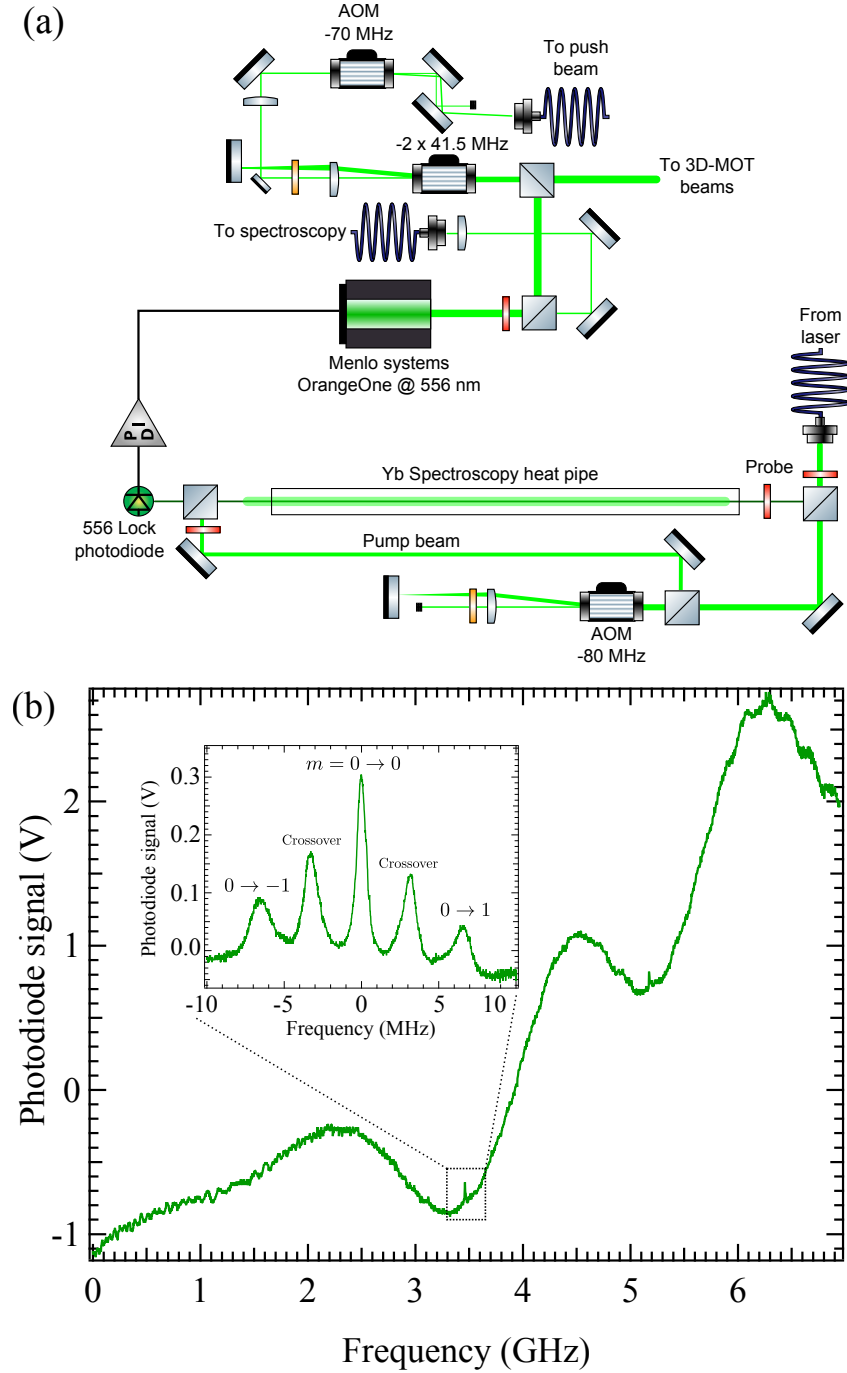
Figure 3.13: (a) Schematic of 556 nm laser setup. The laser is locked 80 MHz above the $^1S_0 \rightarrow{}^3 P_1$ transition and downshifted to -3 MHz for the 3D-MOT beams and $+10$ MHz for the push beam. The 3D-MOT beams are sent over free space to the experiment chamber while the push beam is fiber coupled. A Doppler broadened spectrum of ^{174}Yb is shown in (b), with the inset showing a saturated absorption spectrum, in the presence of a strong magnetic field. The $J = 0 \rightarrow 1$ transition displays a Zeeman splitting with the $0 \rightarrow 0$ and $0 \rightarrow \pm 1$ transitions clearly visible.

53

the cell was temporarily reopened to add the ytterbium before being evacuated again at room temperature. Once evacuated, the cell was filled with 99.99% helium to a pressure of 10 mTorr before being permanently sealed with a copper pinch-off. The new cell design has a much longer lifetime and can be operated for over a year before the ytterbium has to be replaced. During normal operation the cell is heated to a temperature of 450°C, although as the cell ages this temperature needs to be increased significantly in order to maintain an observable absorption signal.

A typical doppler-free absorption signal from the vapor cell is shown in Figure 3.13(b), and displays a full width at half maximum (FWHM) of 1 MHz, which is much broader than the natural linewidth of 182 kHz. Broadening from stray, inhomogeneous magnetic fields can be eliminated by using a strong bias magnetic field to split the $J = 0 \rightarrow 1$ peak into its three Zeeman sublevels, with the $m = 0 \rightarrow 0$ transition being field insensitive and having an FWHM of about 1 MHz. We attribute this to power broadening since we need 50 I_{sat} of power in the pump beam to see a visible doppler-free signal.

3.3.4 BIODT lasers

BIODT light at 1064 nm is generated from a fiber amplified laser (IPG photonics YAR-30K-1064-LP-SF) and 532 nm light is provided by a separate frequency doubled 1064 nm laser (Coherent Verdi V-18). Light out of both lasers is sent through AOMs for intensity control and the first order diffraction peaks from the AOMs are launched into photonic bandgap fibers (NKT photonics LMA-PM-10) and sent to the experiment. Up to 5 W of 1064 nm light (BIODT-R) and 8 W of 532 nm light (BIODT-G) can be coupled through these fibers with a large, wavelength independent mode diameter of 8.5 μm. A schematic of the 1064 nm and 532 nm laser setups is shown in Figure 3.14.

3.3.5 423 nm laser for the lattice

The 423 nm light for the magic-wavelength lattice is primarily provided by a TA-SHGpro system similar to the one used for the 399 nm transition in Yb. This laser can
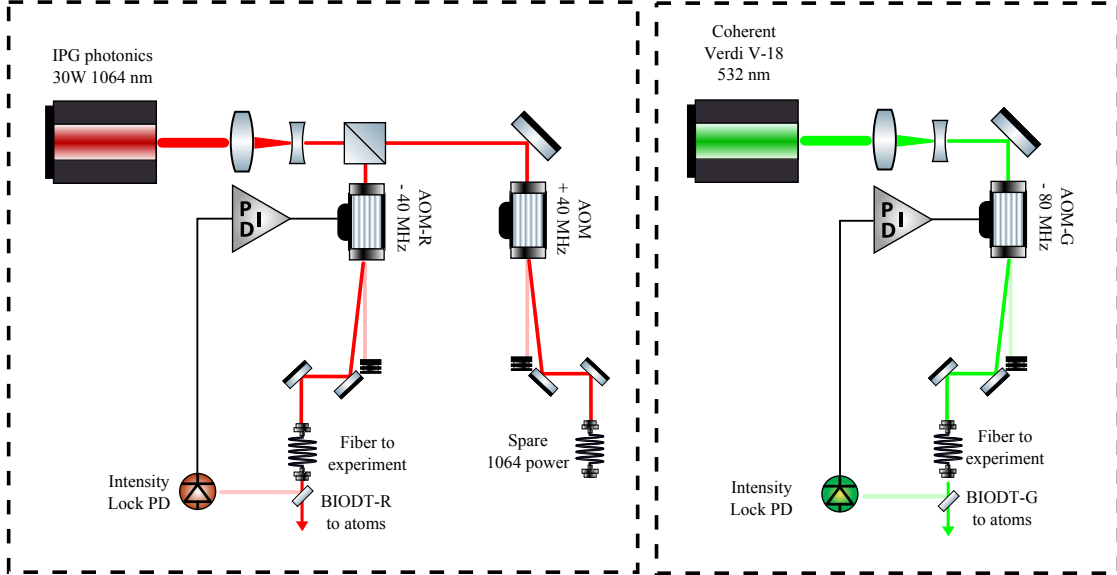
Figure 3.14: Schematic of the 1064 nm and 532 nm laser setups. Both dipole beams are fiber coupled to the experiment and intensity stabilized at the fiber output. The intensity of the BIODT-R(G) is controlled through AOM-R(G).

provide up to 200 mW of light which is sent through an AOM for intensity control and then over a fiber to the experiment table. Up to 100 mW of 423 nm light is available on the experiment table and we are currently in the process of constructing an injection-locked diode laser to provide additional power for more lattice beams. A schematic of the 423 nm laser system is shown in Figure 3.15.

3.4 Magnetic field control

Preparation of the two MOTs and Rb magnetic trap requires a quadrupole magnetic field with a field gradient that can be varied between 1 G/cm (for the Yb MOT) and 200 G/cm (for efficient RF evaporation of Rb). The quadrupole field is provided by a pair of magnetic coils running currents in opposite directions, placed in the recessed viewports of the experiment chamber. These coils are water cooled and capable of carrying up to 300 A of current in order to achieve field gradients up to 242 G/cm. In addition, three pairs of Helmholtz coils (the shim coils) oriented along three orthogonal
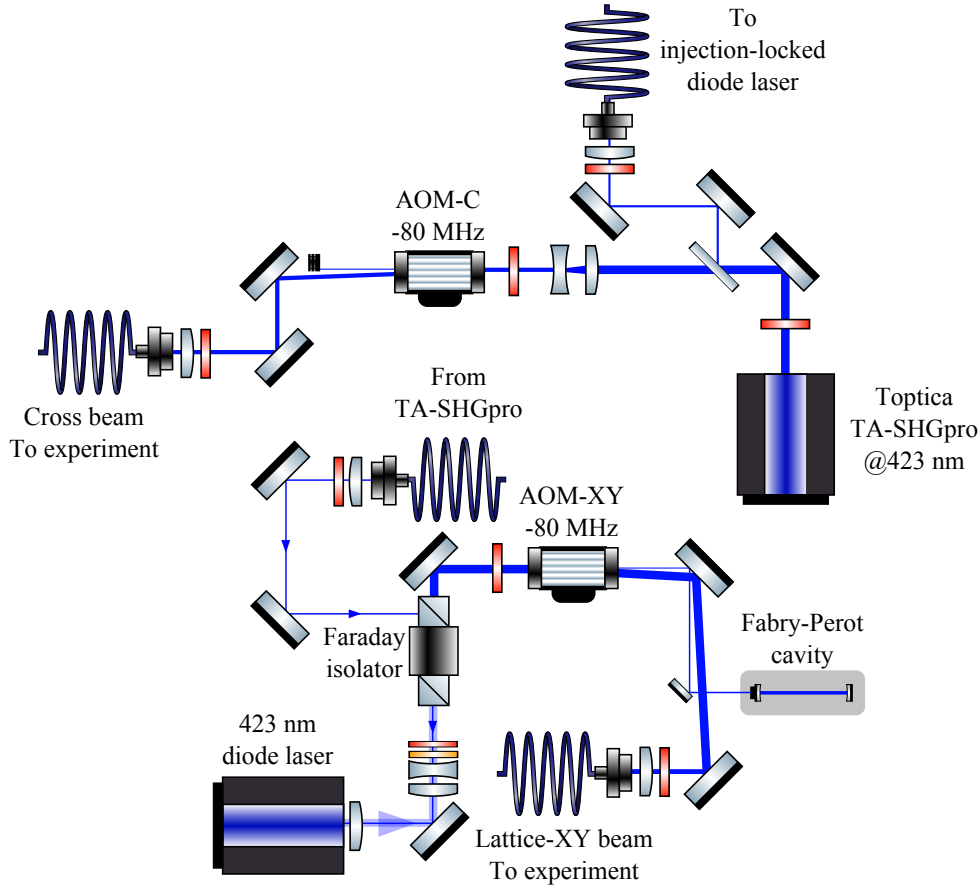
Figure 3.15: Setup of 423 nm laser and injection locked diode. The Toptica TA-SHGpro provides power to the cross-dipole beam, whose intensity is controlled through AOM-C. In addition 5 mW of power from the TA-SHGpro is used to seed a diode laser that provides power for the Lattice-XY beam, which is controlled through AOM-XY.

axes, can provide an arbitrary uniform magnetic field which is typically used to move the position of the quadrupole field zero (See Figure 3.16). The vertical shim (called the Bias coil) is also water cooled with the capacity to carry a up tp 300 A, although we typically never run more than 50 A through this coil, which provides a bias field of 62 G in the vertical direction.

The quadrupole and bias coils were constructed from insulated 0.158" square copper tubing to allow for water cooling. Each quadrupole coil was constructed as a two coils, connected in series. The first coil has two layers of six turns each, with an inner
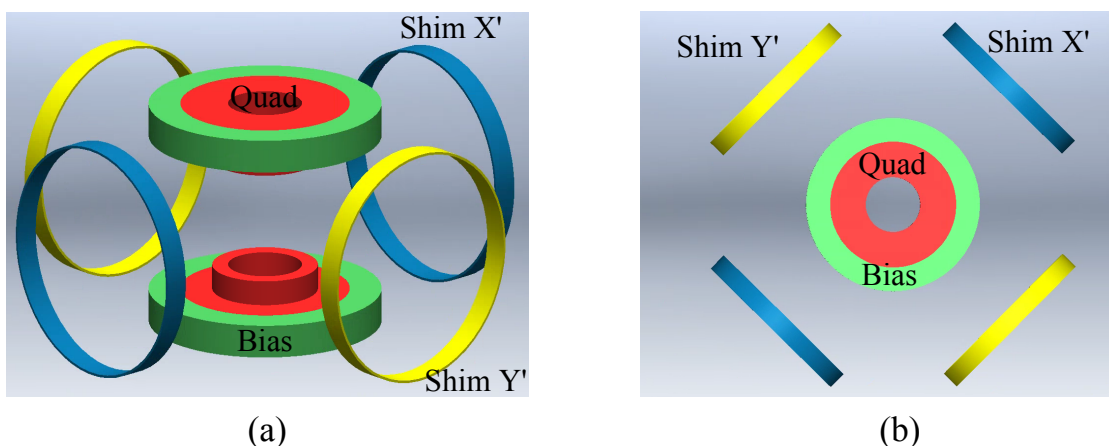
Figure 3.16: A 3D view (a) and a top view (b) of the magnetic field coils attached to the experiment chamber. The quadrupole (red) and bias (green) coils are placed in the recessed viewports of the chamber while the shim coils (blue and yellow) are wound around the 4.5" Conflat viewports.
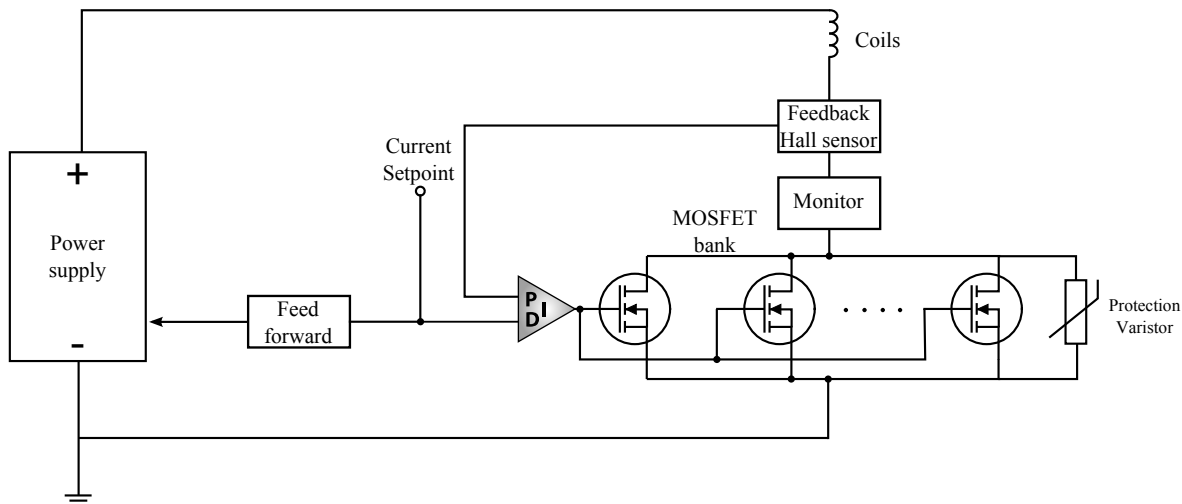
Figure 3.17: An overview of the current control system for the quad and bias coils. Two Hall sensors are used for each coil, with one being used for feedback while the second one is used simply as a current monitor. A varistor connected across the MOSFET bank protects the MOSFETs from large transient voltages created during fast switching of the coils.

layer having an inner diameter of 1.7". The second coil consists of four layers with three turns each, wound around the top of the first coil. The bias coil also created from the same square copper tubing has four, three-turn layers which are wound around the quadrupole coil. The horizontal shim coils are made from 10 turns 14 guage insulated magnet wire, wound around the 4.5" Conflat viewports shown in Fig. 3.7. The quadrupole coils generate a field gradient of 0.81 G cm^{-1} A^{-1}, the bias coil generates a magnetic field of 1.1 G A^{-1} and the horizontal shims generate fields of 0.3 G A^{-1}.

In order to achieve noiseless control of the quadrupole field over two orders of magnitude, the currents in the quadrupole coil and vertical shim are stabilized using the current servo shown in 3.17. The current flowing through the coils is measured using a Hall sensor (F.W. Bell) and stabilized to a programmable analog voltage (current setpoint), by controlling the gate voltage of a bank of six MOSFETs (ST-E250NS10) by means of a PI filter. The bandwidth of the PI filter for the quadrupole and bias coils is limited to around 200 Hz by their large inductances of 440 μH and 300 μH respectively. Since the quadrupole coil is required to run a significantly larger current than the rest, a "feed-forward" stage is added which increases the power supply voltage, in proportion to the coil current. This ensures that the voltage drop across the MOSFETs is not excessively large at low currents and reduces power dissipation in the MOSFETs, thus increasing their lifetime.

Chapter 4: Precision measurement of $5s \rightarrow 6p$ matrix elements in ^{87}Rb

The species-selective lattice for ytterbium is made possible due to a tune-out wavelength in ^{87}Rb where opposing light shifts from the $5s \rightarrow 5p$ and $5s \rightarrow 6p$ transitions cancel out, resulting in a vanishing light shift. The value of this tune-out wavelength is determined predominantly by the ratio of the two transitions matrix elements and a precise measurement of its position allowed us to extract the value of the $5s \rightarrow 6p$ matrix element. This chapter is focused on a new method we developed to measure the extremely weak light shifts near the tune-out wavelength and will present the data from our measurement.

While our interest in the tune-out wavelength stems from the implementation of a species-selective lattice, the ability to precisely measure matrix elements has far-reaching applications, especially in the context of atomic clocks [46, 47] and tests of fundamental symmetries [48, 49]. In atomic clocks, the largest contribution to the uncertainties arises from the blackbody radiation shift [50] caused by the non-zero temperature of the environment where the experiment is performed. Typically, the blackbody spectrum of a room temperature environment is spectrally broad and a precise knowledge of transition strengths to various excited states is necessary to calculate the AC Stark shift from this spectrum.

The conventional method of measuring dipole matrix elements involves either measuring lifetimes of an excited state [51] or performing photoassociation spectroscopy to calculate strength of the dipole-dipole interaction between two atoms [52]. The former method yields inaccurate results when the excited state branches to multiple lower-lying levels while the latter requires using purely long range excited molecular states, which do not always exist. Here we present a more general method, first proposed in [53], to

extract matrix elements using tune-out wavelengths. We demonstrate the measurement of $5s \to 6p$ matrix elements in ^{87}Rb to a precision of 0.3%.

4.1   Measuring matrix elements through multi-pulse diffraction

The wavelength where the light shift of $5s_{1/2}$ vanishes may be precisely determined by measuring the extremely weak light shifts near the region of the tune-out wavelength λ_0, as shown in Fig. 4.1. Near 420 nm, two tune-out wavelengths exist – one between the $6p_{1/2}$ and $6p_{3/2}$ states, and another between the $5p$ and $6p$ manifolds of ^{87}Rb. While a precise determination of the absolute light shift in this region would allow us to infer the $5s \to 6p$ matrix element, such measurements are notoriously difficult since they require detailed knowledge of the spatial profile and optical intensity of the laser beam providing the light shift. However by measuring the relative light shift as a function of wavelength near λ_0, one can infer the $6p$ matrix elements from the $5p$ matrix elements, which are known to a precision of 0.25% [54].

The light shift of $5s_{1/2}$ was measured through Kapitza-Dirac diffraction [55] of a ^{87}Rb BEC, from the Lattice-XY beam shown in Fig. 3.9. At $t = 0$, the lattice beam is pulsed on and the population in the diffracted order is measured as a function of pulse time t. The amplitude and oscillation frequencies of the diffracted orders are dependent on the lattice depth, and can be used to infer the size of the light shift as a function of the wavelength of the lattice light. Since the light shift is proportional to the atomic polarizibility, a measurement of the light shift is sufficient to precisely determine the positions of λ_0.

The time-evolution of the diffracted orders is governed by the lattice Hamiltonian,

$$\hat{H} = \frac{\hbar^2}{2m}\partial_x^2 + \frac{V_0}{2}\cos\left(2k_L x\right) \tag{4.1}$$

where the second term is the lattice potential formed by a retro-reflected lattice beam with wavevector $k_L\hat{\mathbf{x}}$. The time-dependent Schrodinger's equation may be solved by expanding the BEC wavefunction in the basis of plane waves, $\psi(x,t) = \sum_n c_n(t)e^{i2nk_L x}$ where $n = 0$ is the undiffracted BEC, and $n = \pm1, \pm2, \ldots$ correspond to the diffracted
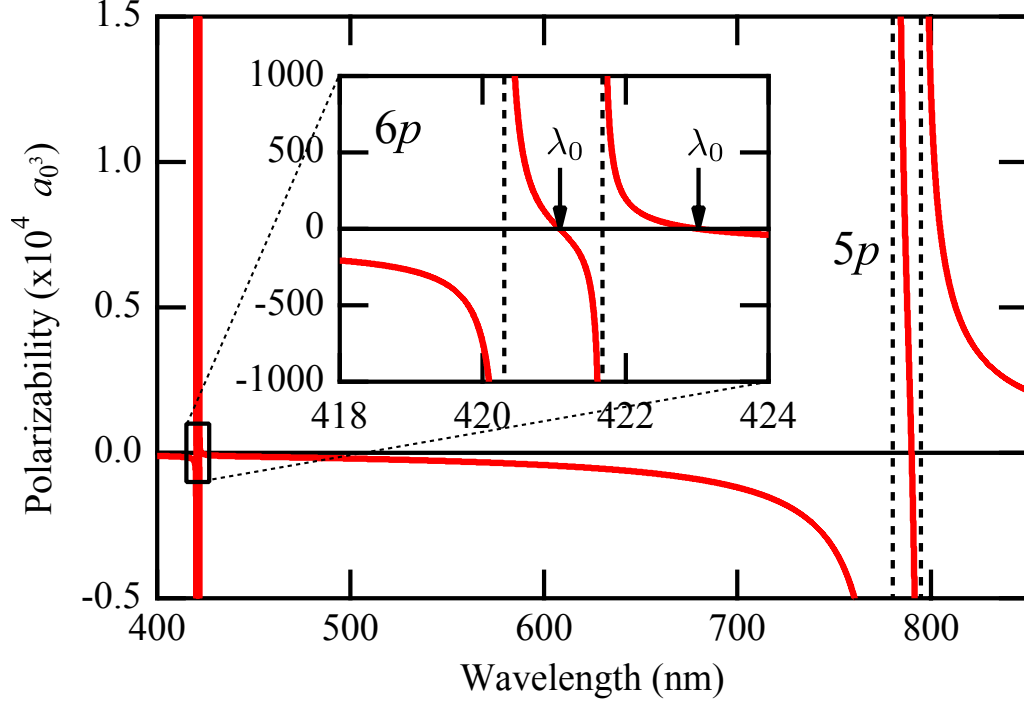
Figure 4.1: Calculated polarizability of ^{87}Rb. The vertical lines indicate electronic transitions of ^{87}Rb and the arrows mark the tune-out wavelengths λ_0. The polarizibilities were calculated as described in Appendix B. In order to extract an accurate value of the polarizibility, we included contributions from the $5s \rightarrow 7p$ and $5s \rightarrow 8p$ transitions, as well as a wavelength independent term to account for levels above $8p$ and excitations of the core electrons of ^{87}Rb.

momenta $2\hbar n k_L$. This expansion results in a set of linear, coupled differential equations,

$$i\hbar \frac{dc_n}{dt} = \left(4n^2 E_r\right) c_n + \frac{V_0}{4} \left(c_{n+1} + c_{n-1}\right) \tag{4.2}$$

where $E_r = \hbar^2 k_L^2 / 2m$ is the recoil energy from a single lattice photon. The solutions corresponding to Kapitza-Dirac diffraction of an initially stationary BEC are found by solving Equations 4.2 with the initial condition $c_n(0) = \delta_{n,0}$. The evolution of the diffracted populations $P_n(t) = |c_n(t)|^2 + |c_{-n}(t)|^2$ is shown in Fig. 4.2 for several lattice depths from $V_0 = 20E_r - 2E_r$.

The oscillation amplitude P_n, and frequency both increase with lattice depth V_0, as the population in first-order diffraction peaks becomes large for large lattice depths. For the weak lattices ($V_0 < E_r$) we were interested in measuring, the amplitude is under 1% and the diffracted signal is very weak, but the period of oscillation approaches the
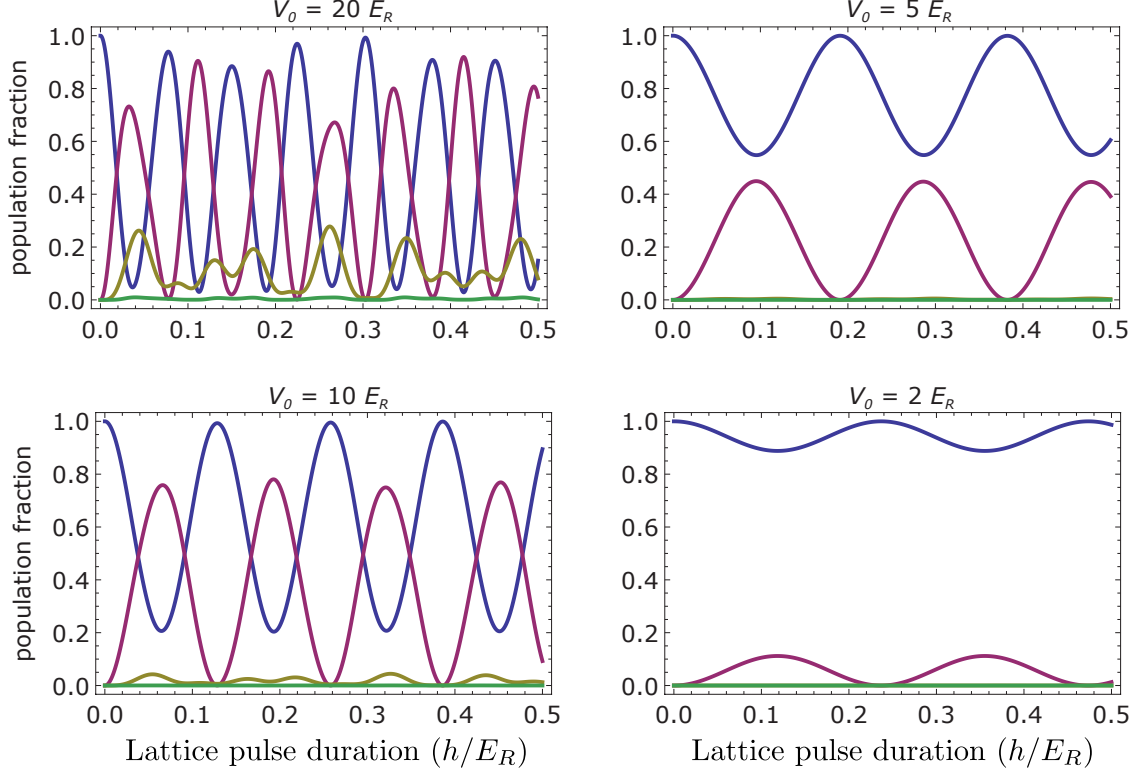
Figure 4.2: The evolution of the diffracted populations, P_0 (blue), P_1 (red), P_2 (yellow) and P_3 (green) for various lattice depths V_0. For weak lattices, the population oscillates between P_0 and P_1 and all higher orders are negligible. The period of oscillation also approaches the Talbot time τ.

Talbot time, $\tau = h/4E_r$. Hence, we developed a pulse sequence to amplify the diffracted population for weak lattices that allowed us to measure very weak light shifts near λ_0. The sequence illustrated in Fig. 4.3, involves a series of lattice pulses of length $\tau/2$, interleaved with $\tau/2$ long periods of free evolution. The effect of this sequence is most easily visualized by the Bloch spehere in Fig. 4.3(b). The first pulse (blue) is a π-pulse about a tilted axis of the Bloch sphere and the free evolution (red) of $\tau/2$ causes precession about the polar axis of the sphere with a period of τ. Consequently, a series of N_p pulses of a weak lattice results in an amplified population in the $\pm 2\hbar k_L$ diffracted orders allowing us to measure lattices created from light shifts as low as $0.09E_r$, where the single pulse diffracted population would have been 0.00025%, and well below our signal-to-noise ratio.
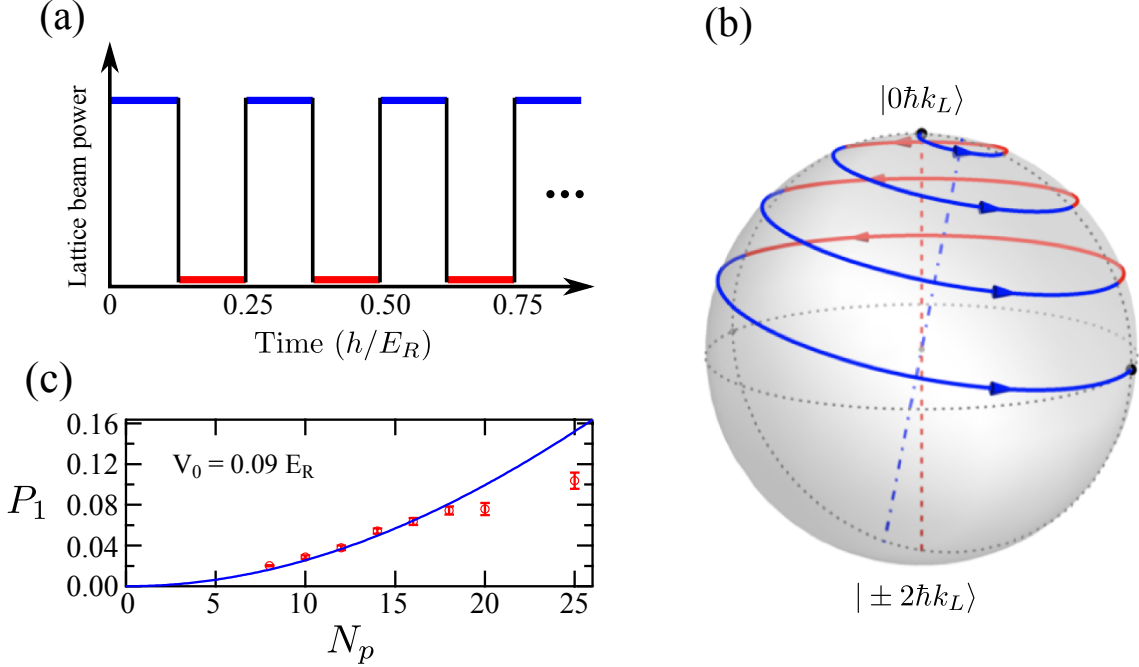
Figure 4.3: (a) Multi-pulse sequence for amplifying the diffracted amplitude from weak lattices. The evolution of the Bloch vector is illustrated in (b) and is shown for a $1E_R$ deep lattice. Typically, we measure lattice depths well under $1E_R$. The diffracted fraction as a function of pulse number N_p is shown in (d).

4.2 Experimental procedure

The experiment was performed with an ^{87}Rb BEC containing 3.5×10^4 atoms in the $|F = 1, m_F = -1\rangle$ state with a negligible thermal fraction. The BEC was trapped in the hybrid optical and magnetic trap described in Chapter 2, with a dipole beam waist of 50 μm. The small size of the BEC ensured that its chemical potential $\mu/h \sim 40$ Hz was small compared to the recoil energy $E_r \approx 12.8$ kHz of the lattice, and interactions between atoms did not significantly affect the diffraction dynamics. For this experiment, the Lattice-XY beam mentioned in Chapter 2 was focused down to a waist of 110 μm with its intensity varying by only a few percent over the Thomas-Fermi radius of the BEC.

The light shift was measured by applying a series of N_p pulses to the BEC and measuring the diffracted fraction $f = P_1/(P_0 + P_1)$ as a function of lattice wavelength between 419 and 424 nm. For the wavelengths we used, the lattice was weak enough

to ensure that the second-order diffraction peaks had no discernible population. The wavelength of the lattice light was monitored by a wavemeter to an accuracy of 18 fm and the intensity of each lattice pulse was monitored by a photodiode. The diffracted population as a function of N_p is shown in Fig. 4.3(c) and shows a quadratic dependence on N_p up to 18 pulses. The deviation from theory at larger N_p is caused the diffracted orders separating in the trap during the pulse sequence, leading to a reduced overlap. Therefore, in order to accurately measure the light shift we used fewer than 15 pulses for all our data.

While the lattice light used was linearly polarized to eliminate the vector light shift, we measured an ellipticity of $\approx 1\%$ in the polarization of our lattice beam after transmission through our chamber window. In order to account for a systematic shift of λ_0 from window birefringence, we repeated the diffraction measurements for S and P polarizations with respect to the chamber window. The induced ellipticity, and consequently vector light shift contributions have opposite signs for S and P polarizations and averaging the two measurements cancels the contribution of the vector shift to the measurement of the tune-out wavelength, down to 10 fm.

4.3 Analysis and results

In order to determine the lattice depth V_0 from a measurement of f, Equations 4.2 were numerically solved in Mathematica for our pulse sequence and the diffracted fraction $f(N_p, V_0)$ was calculated. This relation was inverted to find $V_0(f, N_p)$, allowing us to infer the lattice depth for a measured f and a known N_p. In order to remove the effects of intensity fluctuations between shots, the calculated lattice depth was normalized by the average measured intensity of N_p pulses to extract a value proportional to the polarizability α of ^{87}Rb. Finally, statistical uncertainties were reduced by averaging over 20 repetitions of the experiment at each wavelength and the resulting data are presented in Fig. 4.4.

Near each of the two tune-out wavelengths, the light shift was measured for both S- and P-polarizations in order to eliminate the effect of the vector light shift. The light
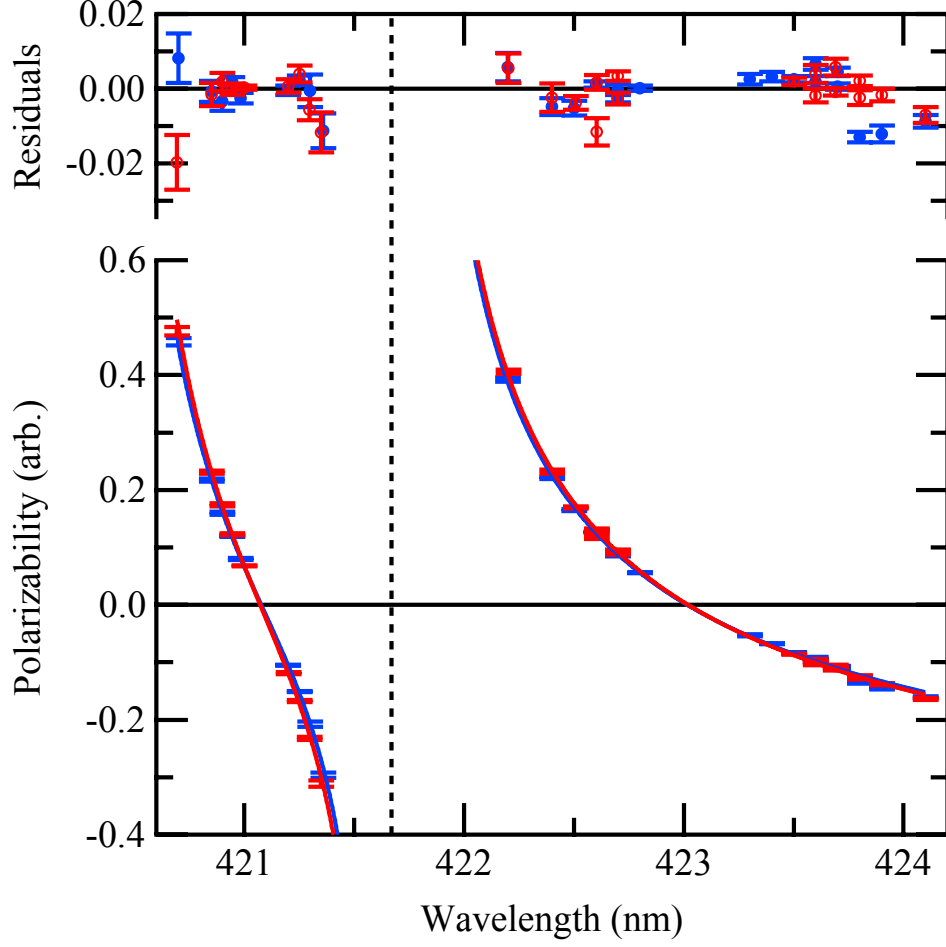
Figure 4.4: The measured polarizability as a function of wavelength for the S (red) and P-polarizations. Each data point is averaged over 20 measurements with the error bars representing 1σ statistical uncertainty. The solid lines are fits to Eqn. 4.3 with the $6p$ matrix elements as the only free parameters. Reduced χ^2 for S and P fits are 4 and 11 respectively.

shift near both tune-out wavelengths was simultaneously fit to a function of the form,

$$\alpha \propto \frac{1}{3} \sum_n \sum_j \frac{|d_{np_j}|^2 \omega_{np_j}}{\omega^2 - \omega_{np_j}^2} + C_{\text{tail}} + C_{\text{core}} \tag{4.3}$$

where d_{np_j} are the dipole matrix elements, ω_{np_j} are the frequencies of the $5s_{1/2} \to np_j$ transitions and ω is the frequency of the lattice light. The dipole matrix elements $d_{6p_{1/2}}$ and $d_{6p_{3/2}}$ were the only free fit parameters. The values of d_{5p_j} were set by accurate lifetime measurements [54] while the $7p$ and $8p$ matrix elements, along with C_{core} (the contribution of the core electrons of ^{87}Rb) are calculated in [53]. The C_{tail} term includes corrections to the polarizability from higher-lying states with $n > 8$ that add a frequency

independent contribution to the light shift. Fitting Eqn. 4.3 to the λ_0 near 421 nm constrains the ratio $R_{6p} = d_{6p_{3/2}}/d_{6p_{1/2}}$ since the position of this zero depends strongly on the relative size of the $6p$ matrix elements. Performing the same fit around the λ_0 near 423 nm constrains the average value of d_{6p_j}, with respect to the values of d_{5p_j} which are well-known.

The values of the matrix elements, and uncertainties in $d_{6p_{1/2}}$, $d_{6p_{3/2}}$ and R_{6p} are summarized in Table 4.1. The statistical uncertainties in all three values are approximately the same, at the level of 0.1%. The largest contribution to the uncertainties in $d_{6p_{1/2}}$ and $d_{6p_{3/2}}$ arises from the theoretical uncertainty in $np_{3/2}$ component of C_{tail} and an uncertainty in the experimentally measured value of $d_{5p_{3/2}}$. Contributions to the uncertainty of R_{6p} arising from sources other than statistical uncertainty are negligible since current atomic theory can more accurately predict ratios, rather than the absolute value of matrix elements. Finally in order to account for a possible drift in the alignment of the lattice beams, we simulated the effect of a 5% drift in the position of the lattice beams across a data set. This resulted in 0.2% uncertainty in $d_{6p_{1/2}}$ and a 0.1% in R_{6p} and $d_{6p_{3/2}}$.

Using our method we determine the ratio of the $6p$ matrix elements to be $R_{6p} = 1.617(2)$ and their absolute values to be $d_{6p_{1/2}} = 0.3235(9)ea_0$ and $d_{6p_{1/2}} = 0.5230(8)ea_0$, in excellent agreement with the theory presented in [53]. Using these values we determine the position of the λ_0 points to be 421.075(2) nm and 423.018(7) nm. Our uncertainties in the matrix element measurements are a significant improvement over the theory in [53], and provide a benchmark needed to test these calculations. Furthermore this measurement technique can by applied to optical clock states, such as the $^3P_0$ state in Yb and Sr, in order to precisely determine dipole matrix elements and account for blackbody radiation shifts in clocks.

Contribution	$\delta d_{6p_{1/2}}$	$\delta d_{6p_{3/2}}$	δR_{6p}
statistical	1.79	1.90	11.1
$d_{5p_{1/2}}$	0.84	1.34	0.004
$d_{7p_{1/2}}$	0.08	0.13	0.012
$d_{8p_{1/2}}$	0.02	0.04	0.003
$np_{1/2}$ tail	0.56	0.92	0.029
$d_{5p_{3/2}}$	1.77	2.87	0.007
$d_{7p_{3/2}}$	0.22	0.36	0.031
$d_{8p_{3/2}}$	0.06	0.10	0.007
$np_{3/2}$ tail	2.01	3.28	0.104
core	1.25	2.05	0.064
alignment drift	7.82	6.18	19.9
Total	8.62	8.24	22.8
theoretical value [53]	0.325(9)	0.528(13)	1.624(7)
our results	0.3235(9)	0.5230(8)	1.617(2)

Table 4.1: Absolute uncertainty contributions (in $ea_0 \times 10^{-4}$) for the $5s$-$6p$ matrix elements and their ratio ($\times 10^{-4}$). Note the insensitivity of R_{6p} to uncertainty in the fit parameters. Total uncertainty is summed in quadrature. Additionally, our $5s$-$6p$ matrix elements are compared to the theoretical values (in ea_0).

Chapter 5: Degenerate mixtures of rubidium and ytterbium

A degenerate mixture is a prerequisite to performing the studies presented in Chapter 1. While rubidium and ytterbium were initially considered promising choices, the collisional properties of most ytterbium isotopes with ^{87}Rb were later found to be unfavorable as explained in Chapter 2. As a result, we have pursued ^{171}Yb, the only remaining choice, and developed a procedure to sympathetically cool this isotope to degeneracy using ^{87}Rb. This isotope of ytterbium is frequently used as a reference for optical clocks [56, 57] due to its ultra-narrow $^1S_0 \rightarrow {}^3P_0$ transition at 578 nm, and is a prime choice to study ideal, non-interacting Fermi gases due to its vanishing s-wave scattering length.

While one other experiment has realized a degenerate ^{171}Yb gas [25], we have demonstrate a method to create larger, colder degenerate gases of ^{171}Yb which will allow us to realize the lattice cooling schemes presented in Chapter 1. Unlike [25], we use ^{87}Rb as a coolant instead of ^{173}Yb and our species-dependent trap provides a greater degree of control over the sympathetic cooling process. We increase the phase-space density of ytterbium over four orders of magnitude with minimal loss while simultaneously cooling the ^{87}Rb down to degeneracy. This chapter will discuss the details of the cycle we have developed for creating a degenerate mixture and demonstrate the species-selective control that our trap allows.

5.1   Cooling a mixture to degeneracy

Typically a dilute gas is said to be degenerate when its phase space density ρ approaches unity. The peak phase space density of a classical, harmonically trapped gas

is given by,

$$\rho_0 = n_0 \Lambda_T^3 = n_0 \left(\frac{\hbar}{\sqrt{2\pi m k_B T}} \right)^3 \tag{5.1}$$

where n_0 is the peak density of the gas and Λ_T is the thermal deBroglie wavelength, and for typical MOT temperatures and densities is around $10^{-7} - 10^{-8}$. Loading the gas into a tight harmonic trap increases its density, and evaporative cooling reduces its temperature until $\rho_0 \approx 1$ and we achieve degeneracy.

Our approach to create a degenerate mixture is outlined in Fig. 5.1(a). We first load laser-cooled nonmagnetic Yb atoms into the green dipole trap and hold them while a Rb magneto-optical trap (MOT) is prepared and transferred into the magnetic quadrupole trap for forced rf evaporation. The two MOTs have to be loaded sequentially since light-assisted collisions in a two-species MOT severely limit its lifetime and size. The repulsive potential created by the green (532-nm) BIODT beam prevents hot Rb atoms from heating the colder Yb atoms out of the dipole trap. After RF evaporation of the Rb to the temperature of the Yb cloud, the red (1064-nm) beam is turned on, changing the repulsive green potential into an attractive BIODT potential and initiating thermal contact between the two species. Evaporation of Rb in the BIODT is then performed to cool the rubidium and ytterbium clouds to degeneracy.

5.2   Rubidium and ytterbium MOTs

Since ground-state Yb atoms are insensitive to magnetic fields[1], we first transfer Yb into the dipole trap. An 8-s MOT loading stage loads 2×10^7 Yb atoms into the 3D-MOT with a field gradient of 2.4 G/cm. The loading rate of the Yb MOT is improved by spectrally broadening the 556-nm MOT beams from 20 kHz to 5 MHz in order to increase the MOT capture velocity. A 200-ms-long cooling and compression stage reduces the MOT beam linewidth to 20 kHz, reduces the intensity from $10I_s$ to $1.2I_s$, and increases the field gradient from 2.4 to 12 G/cm resulting in a cloud with a

---

[1]The ground state of Yb has no *electronic* magnetic moment.[171]Yb has a nuclear magnetic moment which is smaller than the electronic one by three orders of magnitude and therefore negligible for our purposes.
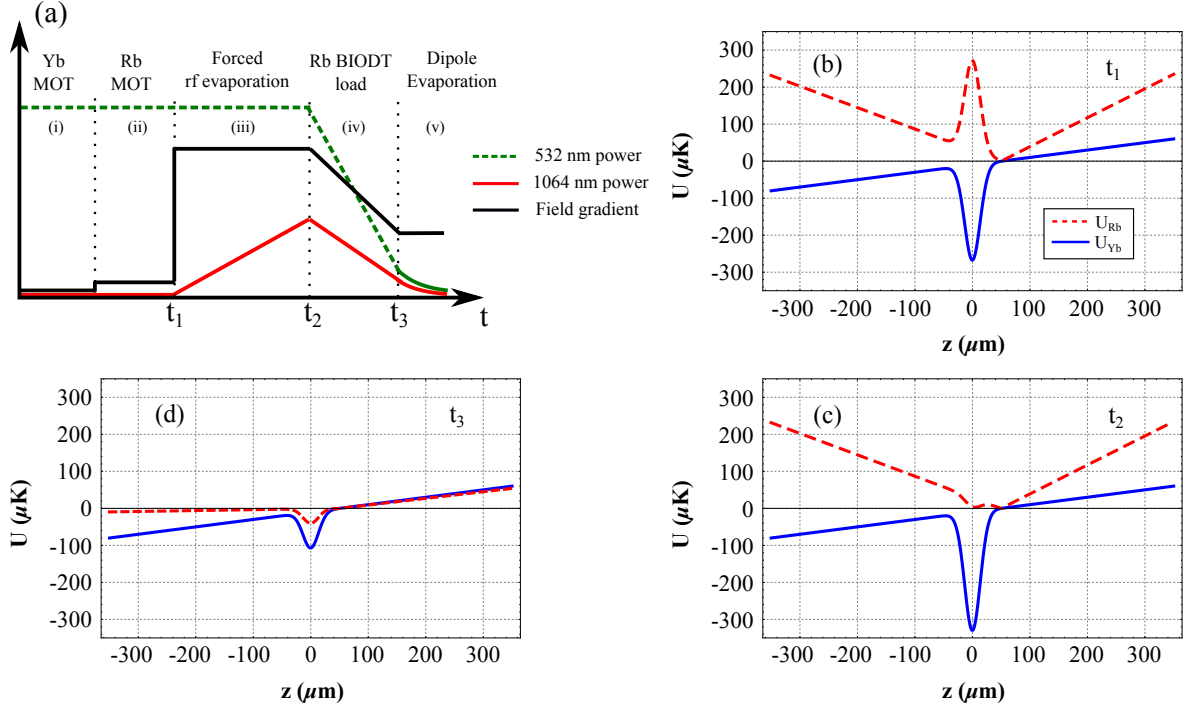
Figure 5.1: (Color online) (a) Experimental sequence for creating degenerate mixtures of ^{87}Rb and ^{171}Yb from steps (i) to (v). (i) ^{171}Yb MOT and transfer into BIODT, (ii) ^{87}Rb MOT and transfer into magnetic trap (iii) RF evaporation of ^{87}Rb in magnetic trap, (iv) transfer of ^{87}Rb into BIODT accompanied by sympathetic cooling of ^{171}Yb and (v) dipole evaporation of ^{87}Rb to degeneracy. (b)-(d) show plots of the full trapping potential for Rb and Yb during points t_1, t_2, and t_3 respectively.

density of 0.03 μm^{-3} and a temperature of 7 μK. We then move the compressed MOT, using uniform magnetic fields, onto the focus of the BIODT before the power in the MOT beams is ramped down, transferring 1.5×10^6 atoms into the trap at 45 μK. The rise in Yb temperature occurs since Doppler-cooling on the narrow 556 nm transition is inefficient in the dipole trap, where both the $^1S_0$ and $^3P_1$ states experience light shifts much larger than the 182 kHz linewidth of the intercombination transition. At this stage the Yb trapping potential of the BIODT is provided by the 532-nm beam at 5 W and the 423-nm beam at 72 mW, resulting in a 325 μK trap depth. The initial temperature of the Yb cloud is much larger than the 4 μK depth of the 423-nm crossed dipole beam, so its contribution at this stage is negligible.

We load the Rb MOT from a Zeeman-slowed atomic beam 2.5 mm above the BIODT to prevent light-assisted collisions from heating Yb atoms out of the trap. Fur-

thermore since the Rb MOT requires a field gradient of 13 G/cm, significantly higher than that for a Yb MOT, we find that sequential loading of the MOTs results in larger trapped clouds compared to simultaneous loading. Using our apparatus, we can only load a very small ^{171}Yb MOT of 1×10^5 atoms at the Rb MOT gradient. Conversely at the Yb MOT gradient of 2.4 G/cm, our Rb MOTs only contain 2×10^7 atoms.

After a 6-s Rb MOT loading stage and a compression and optical pumping stage, 3.5×10^8 atoms of Rb in the $|F = 1, m_F = -1\rangle$ state are transferred into the magnetic quadrupole trap at a field gradient of 192 G/cm. The field zero of the quadrupole trap is situated 50 μm above the BIODT and thermalization between the 105 μK Rb and the 45 μK Yb clouds is initially suppressed by the large repulsive potential of the green BIODT beam for Rb (See Fig.5.1(b)).

5.3   Trap calibration and alignment

Achieving optimal thermal contact between the rubidium and ytterbium clouds in the BIODT requires exceptional control over the overlap between the red and green BIODT beams. A comprehensive trap alignment and calibration procedure was developed to ensure repeatable alignment of of the two BIODT beams. All calibration and alignment procedures were performed with ^{87}Rb and ^{174}Yb due to its larger abundance and larger elastic cross-section compared to ^{171}Yb.

5.3.1   Characterization of BIODT waists

The waists of the beams were characterized through trap frequency measurements. The red beam was characterized through parametric heating measurements of ^{87}Rb and the green beam was characterized through similar measurements with ^{174}Yb. These measurements were performed by weakly modulating the trap depth with a frequency ω as illustrated in Fig. 5.2(a). The modulation couples harmonic oscillator states of the trap that differ by a quantum number of 2, resulting in heating and atom loss. The loss feature is resonant when $\omega = 2\omega_0$, where ω_0 is the trap frequency, and a Gaussian fit to the peak of the loss feature allows us to extract ω_0 as shown in Fig. 5.2(b). In

71

addition, dipole oscillation measurements of a ^{87}Rb BEC were performed at low 1064-nm powers by kicking the ^{87}Rb BEC in the harmonic trap using the quadrupole magnetic field. The resulting oscillation of the cloud velocity was measured by imaging the BEC in time-of-flight, and is shown Fig. 5.2(c). A sinusoidal fit to the oscillation yields the trap frequency ω_0. The parametric heating and dipole oscillation measurements for ^{87}Rb were performed at several different 1064-nm powers and the results are plotted in Fig. 5.2(d). Since ytterbium is non-magnetic, it cannot be kicked using a magnetic field, and dipole oscillation measurements could not be performed easily. As a result, the 532-nm trap frequency measurements for ^{174}Yb were performed solely using parametric heating.

The waist w_0 of the Gaussian BIODT beams may be inferred from fits to Fig. 5.2(d) by a Taylor expansion of the trap potential around the minimum. Expanding Eqn. 2.30 in the x-direction about $(0,0,0)$ yields,

$$U(x) = -U_0 e^{-x^2/w_0^2} \approx -\frac{2\alpha P}{\pi w_0^2}\left(1 - \frac{x^2}{w_0^2} + \ldots\right)$$

where P is the power in the dipole beam. The quadratic term allows us to extract a trap frequency,

$$f = \frac{1}{\pi w_0^2}\sqrt{\frac{\alpha P}{\pi m}} \tag{5.2}$$

Fitting Eqn. 5.2 to the data in Fig. 5.2, with w_0 as the only free fit parameter, allows us to infer the waists from trap frequency measurements at various powers. The polarizibilities α at each of the BIODT wavelengths, for ^{87}Rb and ^{174}Yb were calculated was calculated as outlined in Appendix B. Using this method, the waists were measured to be $w_0^{(1064)} = 27.0(2)$ μm and $w_0^{(532)} = 27.4(1.5)$ μm respectively. The uncertainty in these waists is dominated by astigmatism in BIODT optics, that result in a slight ellipticity in the shape of the Gaussian beam at its waist. This ellipticity breaks the degeneracy between trap-frequencies along the X- and Z-directions (See Fig. 3.9) resulting in broadened, asymmetric parametric heating peaks. The astigmatism is small in the 1064 nm beam resulting in the symmetric signals shown in Fig. 5.2(b). However The 532 nm beam experiences a larger astigmatism and the Yb heating signals display a significantly larger degree of asymmetry, resulting in a larger uncertainty in its waist. The waists
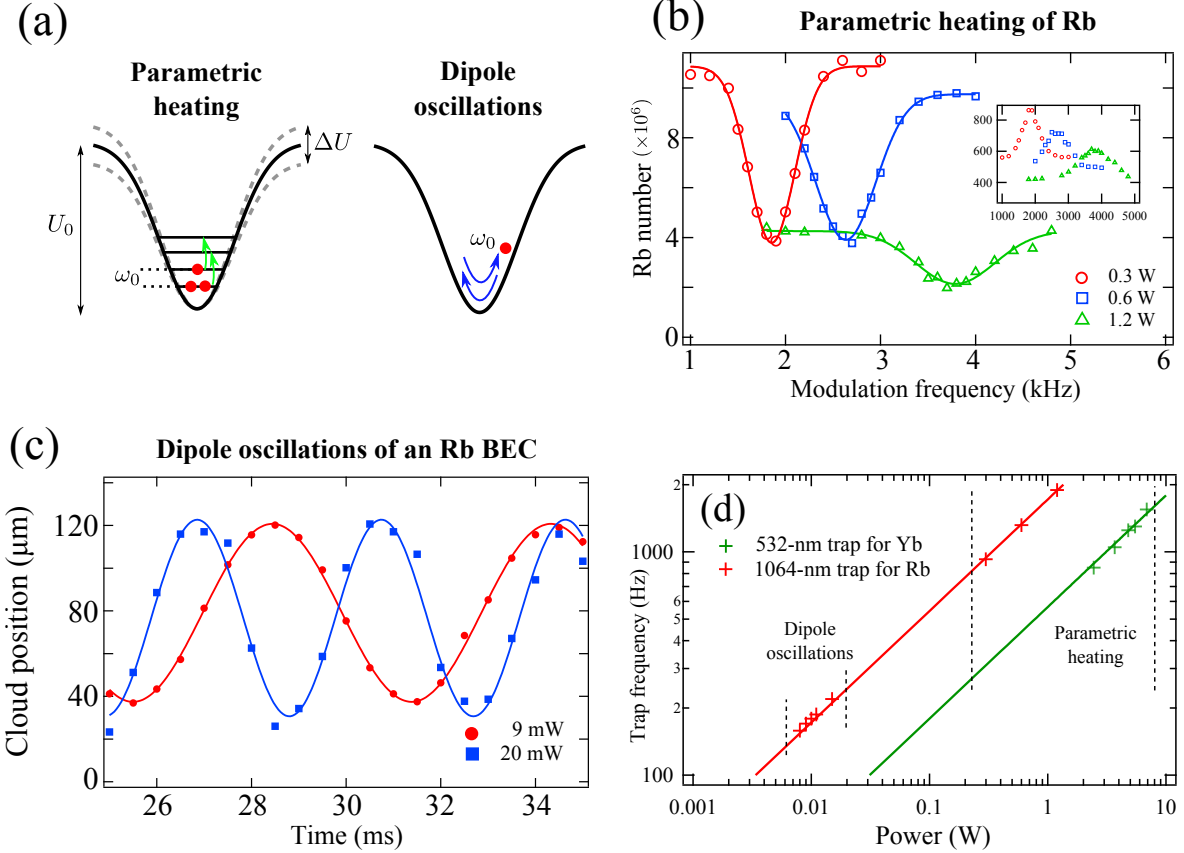
Figure 5.2: (a) Illustrations of performing parametric heating and dipole oscillation measurements. All parametric heating measurements were done with a modulation amplitude ($\Delta U/U_0$) between 0.07 and 0.15. (b) Resonant atom loss of ^{87}Rb in the 1064-nm trap, caused by parametric heating at the twice trap frequency. The inset shows the increase in cloud size in a TOF image which corresponds to an effective increase in temperature from resonant heating. The results for ^{174}Yb in a 532-nm trap are similar. (c) Dipole oscillations of a ^{87}Rb in a 1064-nm trap. (d) Scaling of trap frequencies with power for the red and green trap beams.

calculated from these measurements are used along with the light shift calculations to calculate the trap potentials presented in Fig. 5.1.

5.3.2 Thermalization and BIODT alignment

Measurements of the beam waists were confirmed through two-species cross thermalization experiments in the BIODT. A large (2×10^7 atoms) magnetically trapped cloud of ^{87}Rb at T_r was brought into thermal contact with a small (1×10^6 atoms) yt-

terbium cloud trapped in the BIODT at a temperature of T_y. The subsequent (lossless) thermalization of the ytterbium cloud to T_r was observed and is shown in Fig. 5.3(a) for ^{174}Yb. The time-evolution of the ^{174}Yb temperature can be modeled by a two-species rate equation,

$$\frac{d(T_y - T_r)}{dt} = \frac{\zeta}{\alpha} \bar{n}_o \sigma_{ry} \langle v_{ry} \rangle (T_y - T_r) \tag{5.3}$$

where $\bar{n}_o$ is the *overlap* density between the rubidium and ytterbium clouds, γ_{ry} is the inter-species scattering cross-section and $\langle v_{ry} \rangle$ is the thermally averaged relative velocity between a ^{87}Rb and an ytterbium atom. The constant $\zeta = 0.89$ accounts for the mass difference between the two atoms and $\alpha = 2.8$ is the average number of collisions required to reach thermal equilibrium [MonteCarlo]. The overlap density is a measure of thermal contact between the two trapped clouds with density profiles $n_R(\mathbf{r})$ for rubidium and $n_Y(\mathbf{r})$ for ytterbium,

$$\bar{n}_o = \left(\frac{1}{N_Y} + \frac{1}{N_R} \right) \int n_Y(\mathbf{r}) n_R(\mathbf{r}) \mathrm{d}^3\mathbf{r}$$

The value of n_o is strongly dependent on the trap parameters, particularly the balance between the red and green BIODT beams, as illustrated in Fig. 5.3(c). Since the rubidium cloud is much larger in size than the ytterbium cloud, we may treat it as a heat bath and assume T_r is approximately constant during the thermalization process and its density profile $n_R(\mathbf{r})$ does not change significantly. This allows to analytically solve 5.3 to obtain a solution of the form,

$$T_y(t) = T_y(\infty) + \Delta T e^{-\frac{t}{\tau}} \tag{5.4}$$

which can be fit to the data to extract the thermalization rate τ^{-1} and an equilibrium temperature $T_y(\infty)$.

In order to characterize the thermal contact between rubidium and ytterbium, we measure $T_y(\infty)$ as a function of the power ratio $R = P_{1064}/P_{532}$ between the red and green BIODT beams (See Fig. 5.3(b)). For any given value of P_{532}, we observe a minimum of $T_y(\infty)$ at $R_0 = 0.34$. This can be explained by examining the calculated trap potential at various values of P_{1064} as shown in Fig. 5.3(c). For equal beam waists, at $R = 0.36$, the repulsive potential from the 532-nm beam is exactly balanced by attractive contribution from the 1064-nm beam and the clouds have sufficient spatial overlap to
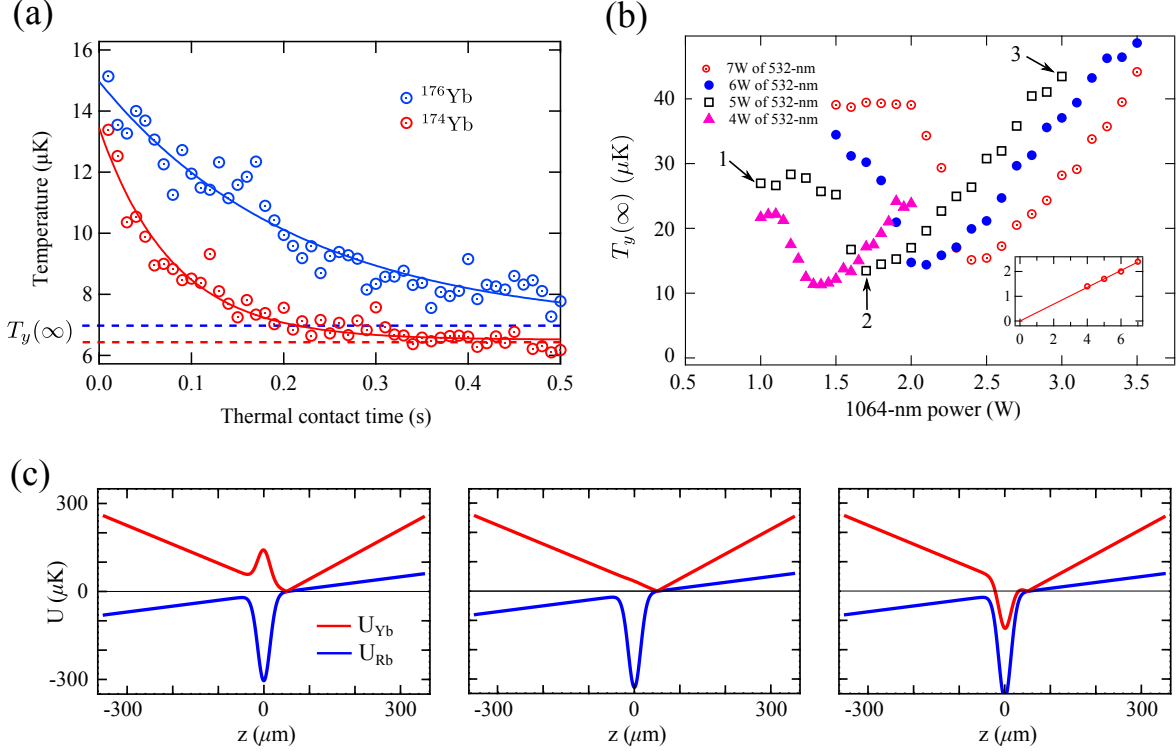
Figure 5.3: (a) Thermalization curves of Yb after it is brought into thermal contact with the Rb magnetic trap. In this dataset T_r was 6.1 μK. The value of $T_y(\infty)$ for a fixed P_{1064} is shown as a function of P_{532} in (b). The minimum of each curve corresponds to the point where the 532-nm and 1064-nm light shifts of [87]Rb should exactly balance each other. The inset shows the value of the minimum as a function of the 1064-nm power and a linear fit to the data yields $R_0 = 0.34(3)$, in excellent agreement with our light shift calculations with predict $R_0 = 0.36$. Plots of the calculated trap potentials for [87]Rb and [171]Yb are shown in (c). The plots correspond to the points 1,2 and 3 labeled in (b).

thermalize. At lower values of R, the repulsive 532-nm potential prevents rubidium from coming into thermal contact with ytterbium and its cooling in consequently suppressed. For significantly higher values of R, rubidium atoms accelerate into the deep, attractive BIODT potential, gaining kinetic energy and *heating* the ytterbium cloud in the process. The value of $T_y(\infty)$ at $R = 0.36$ is incredibly sensitive to the relative position of the red and green BIODT beam waists and is therefore used as a signal to align the two beams to each other. The alignment of the green beam is changed using a picomotor mirror mount, to minimize $T_y(\infty)$ and ensure optimal overlap. We find that we can achieve similar levels of overlap by monitoring the positions of ytterbium clouds, trapped in the
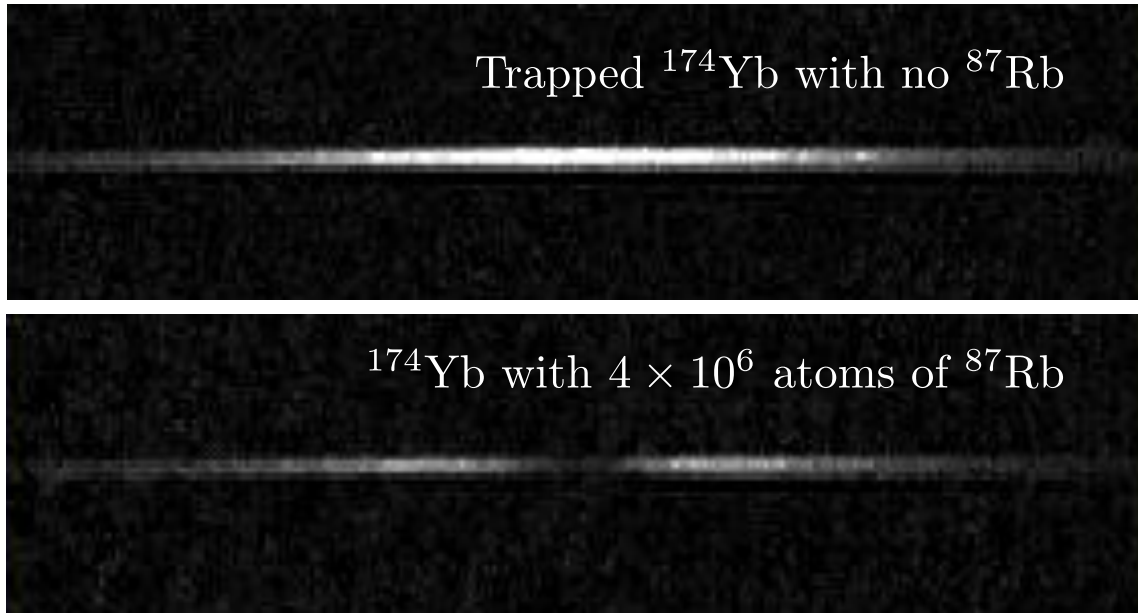
Figure 5.4: Phase separation between the ^{87}Rb and ^{174}Yb clouds trapped in the BIODT at 4 μK. The power in red beam was 1 W while the power in the green beam was 0.7 W.

1064-nm and 532-nm beams and overlapping the two positions in the $y'z$- and xy-imaging directions.

For temperatures below 5 μK, the large scattering length between ^{174}Yb and ^{87}Rb (see Table 2.1) leads to an unusual density distribution for the trapped ytterbium cloud as shown in Fig. 5.4. The center ^{87}Rb cloud creates a density "hole" in the middle of the trapped ^{174}Yb cloud [32], characteristic of phase separation discussed in Chapter 2. While the two clouds in Fig. 5.4 are far from degeneracy and uncondensed, the interspecies scattering length is still large enough to overcome the thermal kinetic energy and cause phase separation. Since the hole occurs at the location of ^{87}Rb, centering the hole along the ^{174}Yb cloud, guarantees alignment of the two BIODT beam waists.

5.4   Radiofrequency evaporation and Rb BIODT load

Once the rubidium and ytterbium clouds are transferred from the MOTs into their respective traps, the first stage of cooling involves forced RF evaporation of the Rb cloud in the magnetic trap. During this stage [stage (iii) in Fig. 5.1(a)], we evaporate the Rb

cloud using RF from 18 MHz to 5 MHz over 5 s, reducing its temperature to 27 μK and increasing its density from 7×10^{10} cm^{-3} to 1×10^{13} cm^{-3}. At the same time we linearly increase the power of the red BIODT beam to 2 W in order to gradually initiate thermal contact with the Yb cloud towards the end of this stage. Throughout this process, the Yb number and temperature remain constant at 1.5×10^6 and 45 μK (Fig. 5.5).

We then load the Rb cloud into the BIODT by decompressing the magnetic trap to 22 G/cm while further lowering the RF frequency from 5 MHz to 1 MHz over 2.5 s [stage (iv) in Fig. 5.1(a)]. The magnetic field gradient of 22 G/cm provides some levitation against gravity for Rb and confinement along the BIODT with a trap frequency of 8 Hz. A linear ramp of BIODT powers, as shown in stage (iv) of Fig. 5.1, increases the overlap between the two species and cools the Yb. Optimal loading of Rb into the BIODT occurs when the green power is reduced to 1.4 W and the red power to 0.8 W. We attribute this to a reduced capture volume at high powers, which stems from differing Rayleigh lengths of the 532- and 1064-nm BIODT beams when their waists are matched as shown in Fig. 5.6. The temperature of both species is reduced to 6 μK at the end of decompression as shown in Fig. 5.5(a) and the Yb cloud suffers minimal loss during this stage. At the end of stage (iv), a Rb cloud containing 7×10^6 atoms and a Yb cloud containing 8×10^5 atoms coexist in the BIODT at 6 μK.

A Ramsauer-Townsend scattering minimum at 50 μK [58] in the interspecies thermalization cross section causes the ^{171}Yb temperature to lag behind the ^{87}Rb temperature during stage (iv). At this temperature, the interspecies cross section drops to 1.2×10^3 a_0^2, well below its low energy s-wave value of 4.4×10^4 a_0^2. However, the thermal distribution of velocities allows us to cool the Yb cloud despite the existence of a scattering minimum, and the two cloud temperatures converge to the same value towards the end of stage (iv).

5.5 BIODT evaporation to degeneracy

We perform the final stage of evaporation [stage (v) in Figs. 5.1 and 5.5] with an exponential ramp of both BIODT powers with a time constant $\tau = 0.5$ s over a
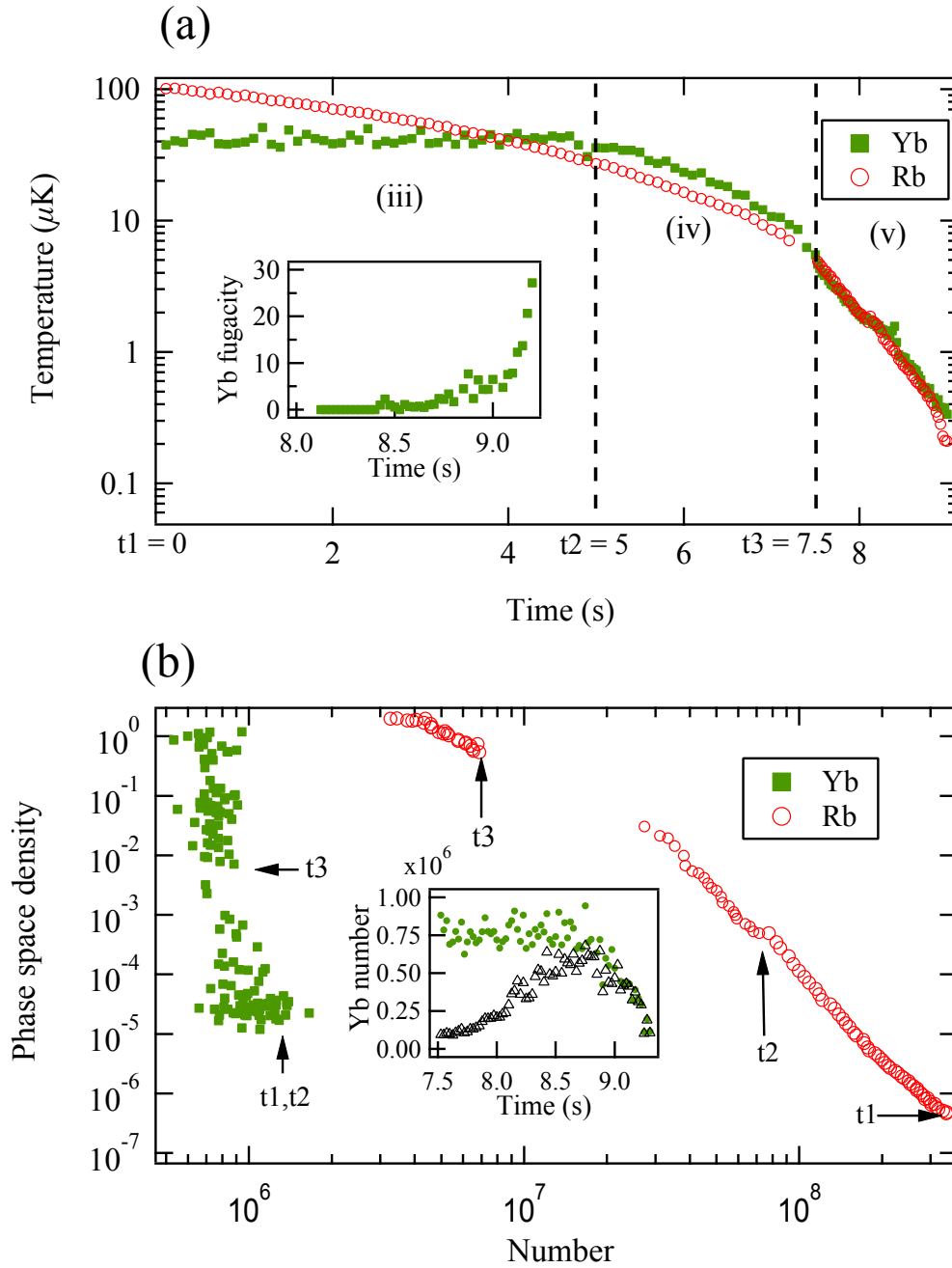
Figure 5.5: (Color online) (a) Temperature evolution of Rb and Yb clouds throughout the evaporation procedure. The labeled steps and times correspond to the ones shown in Fig 5.1. The evolution of the Yb fugacity is shown in the inset. (b) The evolution of the phase space density and number during the evaporation procedure. The steep slope of the Yb data is indicative of efficient sympathetic cooling by Rb. The inset shows the evolution of the Yb number over time during the BIODT evaporation. The total number is given by green circles while the number in the crossed dipole trap is represented by black triangles.

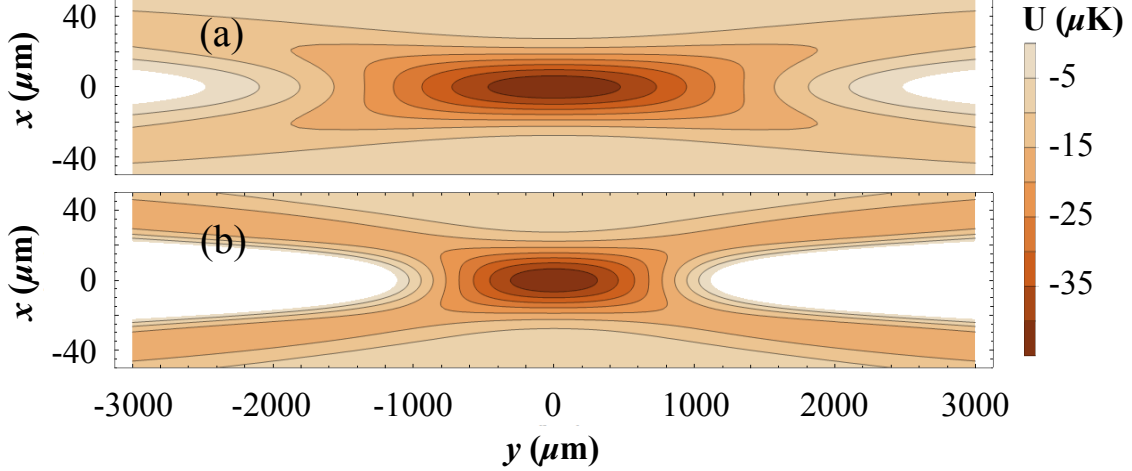Figure 5.6: (Color online) The BIODT potential for a 45 μK deep Rb trap created using two different powers. The white regions are repulsive. (a) Rb BIODT potential for 0.8 W and 1.4 W in the 1064-nm and 532-nm beams respectively. (b) Rb BIODT potential for 2.1 W and 5 W in the 1064- and 532-nm beams respectively.

period of 2 s. Towards the end of this stage the Rb cloud condenses to form a BEC while Yb reaches Fermi degeneracy. The Rb images show a strong bimodal distribution characteristic of a BEC, while the Yb cloud shows significant deviations from a Gaussian distribution (Fig. 5.7). After 1.7 s of evaporation in the BIODT, the Yb cloud reaches a temperature of $T = 0.62(8)T_F = 220$ nK with 4.2×10^5 atoms while the Rb cloud condenses to form a BEC of 3.5×10^5 atoms. Evaporating for 2 s cools the Yb cloud to $T = 0.16(2)T_F = 90$ nK with 2.4×10^5 atoms, at the cost of reducing the Rb BEC number to 1.1×10^5. This is over an order of magnitude improvement over previous methods to cool ^{171}Yb [25] which resulted in 8×10^3 atoms at $T = 0.46T_F$. The uncertainties in our values for T/T_F are dominated by noise in the number of Yb atoms and not by our temperature measurement.

Near degeneracy, we extract the number and temperature of the ^{171}Yb cloud from a two-dimensional fit of a Fermi-Dirac distribution,

$$n(x,y) = B - A\frac{\mathrm{Li}_2\left[-z\exp\left(\frac{x^2}{w_x^2} + \frac{y^2}{w_y^2}\right)\right]}{\mathrm{Li}_2\left(-z\right)} \tag{5.5}$$

to the absorption image, with fit parameters A, B, z, w_x, and w_y. Li_2 is a polylogarithm of order 2 and $z = e^{\mu/k_B T}$ is the fugacity that determines the deviation of the Fermi-Dirac
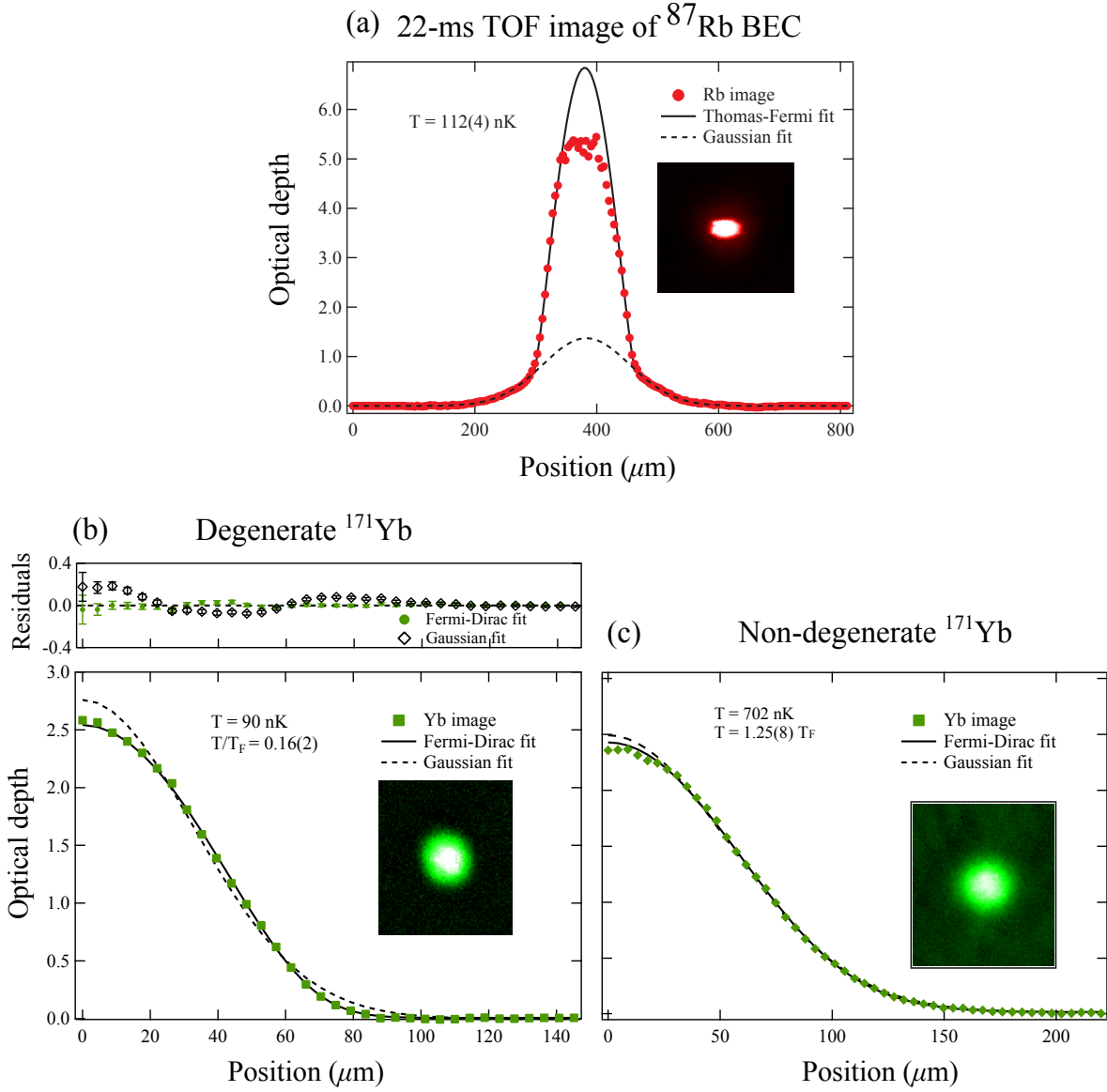
Figure 5.7: (Color online) (a) A 22-ms time-of-flight (TOF) image of a condensed Rb cloud of 5×10^5 atoms at 112 nK, as extracted from a Gaussian fit to the wings of the image. The plot shows a slice of the image across 10 pixels, along with the fits. The bimodal fit is performed only on points with an OD below 3 in order to avoid artifacts from saturation of the probe beam. (b) A 12-ms TOF image of a degenerate Yb cloud at 90 nK with 2.4×10^5 atoms. The plot shows azimuthal averages of the image along with the 2D fits performed on the image. At this temperature the Rb cloud forms a nearly pure BEC, without any discernible thermal wings. (c) For comparison, the momentum distribution of a non-degenerate Fermi gas of ^{171} Yb is shown at $1.25T_F$.

distribution from a thermal Gaussian. For a thermal gas at $T \gg T_F$, $z = 0$ while in the limit $T \ll T_F$ the fugacity diverges. We extract the temperature of the degenerate Fermi gas from w_x and w_y. The number of atoms is determined using two methods: through direct integration of the column density, and indirectly from the fugacity and temperature using the relation

$$\frac{T}{T_F(\omega, N)} = \frac{1}{\ln(z)}, \tag{5.6}$$

which holds in the limit $T \ll T_F$. The former method gives a value of 2.4×10^5 atoms while the latter gives a value of 3.1×10^5, using calculated Yb trap frequencies, $(\omega_x, \omega_y, \omega_z) = (150, 140, 75)$ Hz and assuming an unpolarized Fermi gas[2].

The inset in Fig. 5.5(a) shows the fugacity while the inset in Fig. 5.5(b) shows the evolution Yb number during the final stage of evaporation. The fugacity rises rapidly during the last second of the evaporation as the cloud becomes degenerate but the number, which does not change significantly during the early stages of evaporation, drops as the trap becomes too shallow to support Yb against gravity.

5.6   Trap lifetimes

The lifetime of the degenerate mixture is limited by photon scattering of Yb atoms from the 423 nm beam with calculated rate of 0.4 s^{-1}. We measure the lifetimes of both degenerate clouds under three different conditions shown in Fig. 5.8: Rb in the absence of Yb, Yb in the absence of Rb, and a degenerate mixture. Scattering of 423-nm photons heats the Yb cloud in the absence of Rb, as shown in the inset in Fig. 5.8(b). In the presence of the Rb BEC, this heating rate is reduced and the Rb lifetime is reduced from 2.8 s to 1.5 s [Fig. 5.8(a)] as the Rb cloud evaporates to keep the Yb temperature fixed. The Rb cloud has a peak density of $2.8(5) \times 10^{14}$ cm^{-3} and its lifetime in the absence of Yb is limited by three-body recombination. Using a ^{87}Rb three-body rate constant of $K_3 = 5.8 \times 10^{-30}$ cm^{6}s^{-1} [29], we calculate a three body rate of 0.45 s^{-1}, in approximate agreement with our measured lifetime.

---

[2]The extremely small energy difference between the $m = 1/2$ and $m = -1/2$ sublevels of ^{171}Yb guarantees our magnetic field variations will be non-adiabatic, leading to an unpolarized gas.
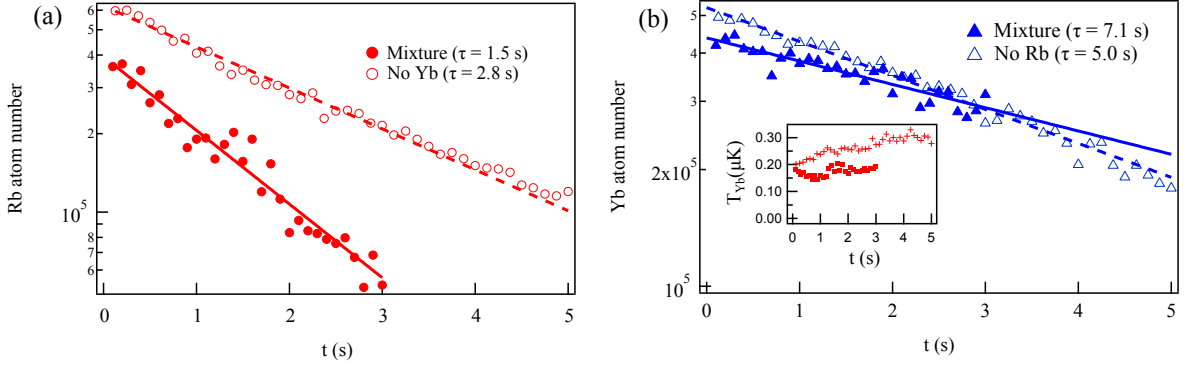
Figure 5.8: (Color online) (a) Lifetime of the Rb BEC with and without the degenerate Yb gas present. (b) Lifetime of the Yb gas with and without the Rb BEC present. The inset in (b) shows the evolution of the Yb temperature in the presence (circles) and absence (crosses) of the Rb BEC. The lines in both plots are fits of an exponential decay to the data.

5.7 Independent control of Rb and Yb clouds

The flexible nature of our trap allows us to control overlap between the two species, and independently address either Rb or Yb atoms. The nonmagnetic Yb atoms are unaffected by the magnetic trap used to confine the Rb cloud along the BIODT beam. Similarly the Rb cloud does not see the 423-nm crossed dipole beam that provides longitudinal confinement for the Yb gas.

The overlap between the two clouds can be controlled by adding a uniform magnetic field to the quadrupole magnetic trap, to shift the position of the magnetic trap along the BIODT. Before BIODT evaporation, the magnetic Rb atoms are moved along the dipole trap while the position of the nonmagnetic Yb atoms is left unchanged. We use the Yb temperature after 0.5 s of BIODT evaporation as an indicator of overlap between the two species, as the noninteracting Yb atoms cannot be efficiently evaporated. This temperature is shown in Fig. 5.9 as a function of the Rb cloud position, with a clear minimum in the Yb temperature indicating optimal longitudinal overlap of the two clouds.

Independent manipulation of the Yb cloud can be achieved through the 423-nm crossed dipole beam. To demonstrate this, we resonantly heat the Yb by modulating
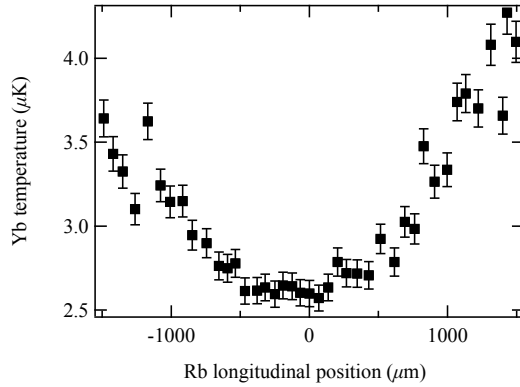
Figure 5.9: Yb temperature after BIODT evaporation, as a function of the position of the Rb cloud. A minimum is observed at 2.5 μK corresponding to the optimal longitudinal overlap between the two clouds.
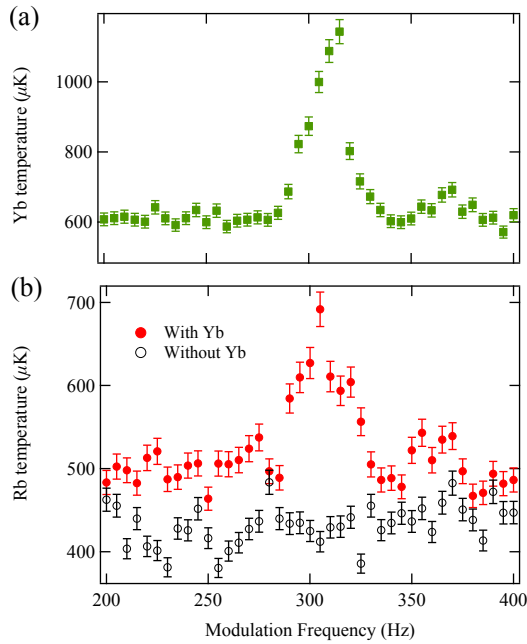
Figure 5.10: (Color online) (a) Yb temperature as a function of 423 nm modulation frequency, showing a resonance at 310 Hz. (b) Rb temperature as a function of modulation frequency in the presence, (red filled circles) and absence (black empty circles) of Yb. The Rb cloud is heated only in the presence of Yb confirming that both species are overlapped and that the 423 nm beam does not affect Rb.

the intensity of the crossed dipole beam at the trap frequency (Fig. 5.10(a)). This in turn heats up the Rb, resulting in a rise in its temperature as shown in Fig. 5.10(b). When this experiment is repeated in the absence of Yb, we observe no heating of the Rb cloud, confirming that the two clouds are overlapped and that the crossed dipole beam only affects Yb.

5.8   Other isotopes of Yb

While ^{171}Yb is the only isotope that can be brought to degeneracy with ^{87}Rb, we also have the capability to create BECs of ^{174}Yb and ^{170}Yb without the use of ^{87}Rb. Due to their favorable scattering lengths (see Table 2.1), sympathetic cooling with ^{87}Rb is not necessary. The evaporation of these isotopes is performed in a combination of the 532-nm BIODT and 423-nm crossed dipole beams and involves a simple exponential ramp of the 532-nm power in time. We can create BECs of 2×10^5 atoms of ^{174}Yb using a 9 s long ramp with time constant of 2 s. A longer, slower exponential ramp is required for ^{170}Yb due to its smaller scattering length and produces condensates of 3×10^4 atoms.

5.9   Outlook

Over the last six years we have built an apparatus to trap and cool mixtures of rubidium and ytterbium to degeneracy. Unfortunately, while the scattering properties of most isotopes made them unfeasible for degenerate mixture experiments we have found that ^{171}Yb behaves extremely well with ^{87}Rb, allowing us to create a large degenerate Fermi gas of this isotope, by sympathetic cooling. In the immediate future a two-dimensional species-selective lattice for ^{171}Yb will be implemented, with the ability to shake the lattice in both directions, and explore the dynamics of excited bands of the lattice in the presence of a BEC bath. This is the first step to realizing several proposals, including new lattice-cooling schemes [7] and methods to generate many-body entangled states [10]. Finally, the ability to create degenerate mixtures also allows us to perform photoassociation experiments between the two species, with the possibility of finding optical Feshbach resonances to tune the interspecies interactions.

Chapter A: Bose and Fermi gases in a harmonic trap

A.1   Density distributions

The energy distribution functions for a unpolarized Fermi (Bose) gas is given by,

$$n(\epsilon) = \frac{2S+1}{e^{(\epsilon-\mu)/k_BT} \pm 1} \tag{A.1}$$

where ϵ is the single particle energy. Typically, the temperature and chemical potential for trapped, degenerate gases is much larger than the harmonic trap frequency $\bar{\omega}$ and in this regime, one can forego the quantized description of the harmonic oscillator energy levels in favor of a continuous energy spectrum.

$$\epsilon(\mathbf{p}, \mathbf{r}) = \frac{\mathbf{p}^2}{2m} + \frac{1}{2}m(\omega_x^2 x^2 + \omega_y^2 y^2 + \omega_z^2 z^2) = \frac{\mathbf{p}^2}{2m} + U(\mathbf{r})$$

The density distribution of a degenerate Bose (Fermi) may be calculated by integrating Eqn. A.1 over all momentum states, which is most conveniently performed in spherical co-ordinates.

$$n(\mathbf{r}) = \frac{1}{h^3} \int \frac{(2S+1)\mathrm{d}^3\mathbf{p}}{e^{(\epsilon-\mu)/k_BT} \pm 1} = \frac{2S+1}{h^3} \int_0^\infty \frac{4\pi p^2 \mathrm{d}p}{e^{(p^2/2m+U(\mathbf{r})-\mu)/k_BT} \pm 1}$$

The above expression may be evaluated making the substitutions $k = p^2/2m$, $Z = \exp\left[(\mu - U(\mathbf{r}))/k_BT\right]$ and using the integral representation of a polylogarithm,

$$\mp \mathrm{Li}_{s+1}(\mp Z) = \Gamma(s) \int_0^\infty \frac{k^s \mathrm{d}k}{e^k/Z \pm 1} \tag{A.2}$$

where the polylogarithm $Li_s(x)$ is defined through the series expansion,

$$\mathrm{Li}_s(x) = \sum_{n=1}^{\infty} \frac{x^n}{n^s}$$

The result of integrating over momentum space is the density distribution of a trapped degenerate gas given by,

$$n(\mathbf{r}) = \mp(2S+1)\left(\frac{2\pi}{\lambda_T^2}\right)^{\frac{3}{2}}\Gamma\left(\frac{3}{2}\right)\mathrm{Li}_{3/2}\left\{\mp\exp\left[\frac{\mu - U(\mathbf{r})}{k_BT}\right]\right\} \quad (A.3)$$

A.2   Momentum distributions

Similarly, the momentum distributions of degenerate gases in a harmonic trap may be evaluated by integrating Eqn. A.1 over $\mathbf{r}$.

$$n(\mathbf{p}) = \frac{2S+1}{h^3}\int_{-\infty}^{\infty}\frac{1}{e^{(p^2/2m+U(\mathbf{r})-\mu)/k_BT}\pm 1}\mathrm{d}x\mathrm{d}y\mathrm{d}z \quad (A.4)$$

The first integral over x may be performed by using Eqn.A.2 with the substitutions,

$$k = \frac{m\omega_x^2 x^2}{2k_BT}$$

$$A = \frac{1}{k_BT}\left(\mu - \frac{p^2}{2m} - \frac{1}{2}m\omega_y^2 y^2 - \frac{1}{2}m\omega_z^2 z^2\right)$$

which results in,

$$n(\mathbf{p}) = \mp\frac{2S+1}{h^3}\Gamma\left(\frac{1}{2}\right)\sqrt{\frac{k_BT}{m\omega_x^2}}\int\mathrm{Li}_{1/2}\left\{\mp\exp\left[\frac{\mu - p^2/2m - U(y,z)}{k_BT}\right]\right\}\mathrm{d}y\mathrm{d}z$$

The intergral over y and z may be performed using the indentity,

$$\int_{-\infty}^{\infty}\mathrm{Li}_n\left(Ae^{-x^2}\right)\mathrm{d}x = \mathrm{Li}_{n+1/2}(A)\sqrt{\pi} \quad (A.5)$$

and the resulting three-dimensional momentum distributions are given by,

$$n_3(p_x, p_y, p_z) = \mp(2S+1)\left(\frac{\sigma}{h}\right)^3\mathrm{Li}_{3/2}\left\{\mp\exp\left[\frac{\mu}{k_BT} - \frac{p^2}{2mk_BT}\right]\right\} \quad (A.6)$$

where $\sigma = \sqrt{k_BT/m\bar{\omega}^2}$ is the size of a non-degenerate thermal cloud in a harmonic trap with frequency $\bar{\omega} = (\omega_x\omega_y\omega_z)^{1/3}$, and λ_T is the thermal deBroglie wavelength. Eqn. A.5 may be further used to evaluate the integrated momentum distributions in one- and two-dimensions,

$$n_2(p_x, p_y) = \mp(2S+1)\left(\frac{\sigma^3}{h^2\lambda_T}\right)\mathrm{Li}_2\left\{\mp\exp\left[\frac{\mu}{k_BT} - \frac{p_x^2 + p_y^2}{2mk_BT}\right]\right\} \quad (A.7)$$

$$n_1(p_x) = \mp(2S+1)\left(\frac{\sigma^3}{h\lambda_T^2}\right)\mathrm{Li}_{5/2}\left\{\mp\exp\left[\frac{\mu}{k_BT} - \frac{p_x^2}{2mk_BT}\right]\right\} \quad (A.8)$$

Finally integrating over the momentum co-ordinates using the same substitution method, one can obtain expressions for the total number of atoms in a Fermi (Bose) gas.

$$N = \mp(2S + 1)\left(\frac{\sigma}{\lambda_T}\right)^3 \mathrm{Li}_3\left\{\mp e^{\frac{\mu}{k_B T}}\right\} \tag{A.9}$$

In the case of a non-degenerate Fermi or Bose gas, $\mu \ll k_B T$ and the fugacity $\mathcal{Z} = e^{\mu/k_B T}$ is much smaller than 1. In the limit of a small argument $\mathrm{Li}_n(x) \sim x$ and the momentum distributions reduce to the gaussian Boltzmann distributions. Near degeneracy, $\mathcal{Z} \geq 1$ and the momentum distributions begin to deviate from a Gaussian. The polylogaritm $\mathrm{Li}_n(x)$ is real in the range $-\infty < x < 1$ allowing the Fermi-Dirac momentum distribution, which scales as $\mathrm{Li}_n(-\mathcal{Z})$, to be evaluated at all momenta. Hence all images of degenerate Fermi gases are fit to a two-dimensional Fermi-Dirac distribution, using a fast MATLAB algorithm for evaluating $\mathrm{Li}_2(x)$.

However the Bose-Einstein distribution, which instead scales with $\mathrm{Li}_n(\mathcal{Z})$, becomes complex at $\mathcal{Z} = 1$, which corresponds to the critical point for Bose-Einstein condensation. For a polarized Bose gas, the relation between critical number and temperature for condensation in a harmonic trap can be found using Eqn. A.9,

$$N_c = \left(\frac{k_B T_c}{\hbar\bar{\omega}}\right)^3 \mathrm{Li}_3\{1\} \tag{A.10}$$

Above the critical temperature T_c, a fit to a two-dimensional Bose-Einstein distribution with $\mathcal{Z}$ as a free fit parameter yields accurate results. Below the critical point, the bimodal distribution described in Chapter 2 is used with a Thomas-Fermi distribution to describe the BEC and the Bose-Einstein momentum distribution from Eqn. A.8, with $\mathcal{Z}$ held fixed at 1 to describe the uncondensed cloud.

Chapter B: Scalar light shifts of rubidium and ytterbium

The interaction between the induced dipole moment $\mathbf{d}$ of a two-level atom (states $|g\rangle$ and $|e\rangle$ seperated by ω_0) and the oscillating electric field $\mathbf{E}$ of a laser beam can be described by,

$$\hat{H}_I = -\mathbf{d} \cdot \mathbf{E}(\mathbf{r}, t) \tag{B.1}$$

with $\mathbf{k}$ and ω being the wavector and frequency of the laser. In the dipole approximation, we may assume that the electric field is uniform over the size of the atom and $\mathbf{E}(\mathbf{r}, t) \approx \mathbf{E}(t)$. Furthermore, since we are using a laser beam with a single wavevector $\mathbf{k}$ and frequency $\omega(\mathbf{k}) = ck$, we may consider only a single mode of the electromagnetic field,

$$\mathbf{E}(t) = \epsilon_{\mathbf{k}} \left(\hat{a}_{\mathbf{k}} e^{i\omega(\mathbf{k})t} + \hat{a}_{\mathbf{k}}^{\dagger} e^{-i\omega(\mathbf{k})t} \right) \tag{B.2}$$

where $\epsilon_{\mathbf{k}}$ is the electric field of a single photon. We can use perturbation theory to calculate the energy shifts of the atomic states in the presence of H_I. The first-order correction vanishes since $\langle g| \mathbf{d} |g\rangle$ is always 0. Using the notation $|g, n_1\rangle$ to represent an atom in the ground state with n_1 photons at frequency ω, we can calculate the light shift ΔU_l of $|g, n_1\rangle$ in second order perturbation theory,

$$\Delta U_l = \sum_{n_2} \frac{\langle g, n_1| \hat{H}_I |e, n_2\rangle \langle e, n_2| \hat{H}_I |g, n_1\rangle}{E_{g,n_1} - E_{e,n_2}} \tag{B.3}$$

In general for an N-level atom with many excited states $|e_i\rangle$ the sum in Eqn. B.3 runs over all intermediate states $|e_i\rangle$ as well. In what follows we will assume assume the laser beam is linearly polarized along $\hat{\mathbf{z}}$, allowing us to make the simplification $\mathbf{d} \cdot \mathbf{E} = d_z E_z$. With the application of the operator in Eqn. B.2 to Eqn. B.3, the expression for the light shift reduces to,

$$\Delta U_l = |\langle g| \mathbf{d} |e\rangle|^2 \left(\frac{(n_1 - 1)\epsilon_{\mathbf{k}}^2}{\omega - \omega_0} + \frac{(n_1 + 1)\epsilon_{\mathbf{k}}^2}{\omega + \omega_0} \right) \tag{B.4}$$

where $n_1 \epsilon_{\mathbf{k}}^2$ is the electric field amplitude E_z^2 of laser beam with a mean number of photons $n_1 \gg 1$. Consequently, the light shift may be written in terms of the electric field,

$$\Delta U_l = |\langle g| d_z |e\rangle|^2 \, \mathbf{E}^2 \left(\frac{1}{\omega - \omega_0} + \frac{1}{\omega + \omega_0} \right) \tag{B.5}$$

For a multi-level atom with excited states $|e_i\rangle$ at energies $\omega_{0,i}$, one may define a decay rate $\Gamma_{i \to g}$ for the $|e_i\rangle \to |g\rangle$ transition,

$$\Gamma_{i \to g} = \frac{\omega_{0,i}^3}{3\pi \epsilon_0 \hbar c^3} |\langle g| d_z |e_i\rangle|^2 \tag{B.6}$$

and a saturation intensity,

$$I_{i \to g} = \frac{\pi h c \Gamma_{i \to g}}{3\lambda_{i \to g}^3} \tag{B.7}$$

This allows Eqn. B.5 to be written as,

$$\Delta U_l = \hbar I \sum_i \frac{\Gamma_{i \to g}^2}{8 I_{i \to g}} \left(\frac{1}{\omega - \omega_{0,i}} + \frac{1}{\omega + \omega_{0,i}} \right) \tag{B.8}$$

which is the convention used in Chapter 2. Alternatively one may write the light shift in terms of the atomic polarizibility α,

$$\Delta U_l = \frac{1}{2} \alpha \mathbf{E}^2 = \sum_i |\langle g| d_z |e_i\rangle|^2 \left(\frac{1}{\omega - \omega_{0,1}} + \frac{1}{\omega + \omega_{0,i}} \right) \mathbf{E}^2 \tag{B.9}$$

which is the convention used to describe the polarizibility in Chapter 4. The decay rates $\Gamma_{i \to g}$ and wavelengths λ_i of transitions used to calculate light shifts in rubidium and ytterbium are listed in Table B.1.

89

	Transitions	λ_i (nm)	$\Gamma_{i \to g}$ ($\times 10^6$ s^{-1})	$|\langle e_i| \mathbf{d} |g \rangle|$ (ea_0)
Yb	$6s^2\ ^1S_0 \to 6s6p\ ^1P_1$	398.9114	192	4.244(44)
	$6s^2\ ^1S_0 \to 6s6p\ ^3P_1$	555.8036	1.15	0.5394(6)
	$6s^2\ ^1S_0 \to 6s7p\ ^1P_1$	246.450	100	1.491(91)
	Core excitation 1	346.437	68.3	2.052(125)
	Core excitation 2	269.169	14.3	0.636(82)
Rb	$5s_{1/2} \to 5p_{1/2}$	794.9789	36.1	4.231(5)
	$5s_{1/2} \to 5p_{3/2}$	780.2412	38.0	5.978(5)
	$5s_{1/2} \to 6p_{1/2}$	421.6726		0.3235(9)
	$5s_{1/2} \to 6p_{3/2}$	420.2989		0.5230(8)

Table B.1: Transitions out of the ground states of rubidium ($5s_{1/2}$) and ytterbium ($6s^2$ $^1S_0$). For the fits performed in Chapter 4, transitions upto $8p_j$ were included and higher lying levels ($n > 8$) were also taken into account through the addition of a frequency independent offset on α.

Bibliography

[1] M. Takamoto, F. Hong, R. Higashi, and H. Katori. An optical lattice clock. *Nature*, 435(7040):321, 2005.

[2] D. Jaksch and P. Zoller. The cold atom hubbard toolbox. *Annals of physics*, 315(1):52, 2005.

[3] M. Lewenstein, A. Sanpera, V. Ahufinger, B. Damski, A. Sen, and U. Sen. Ultracold atomic gases in optical lattices: mimicking condensed matter physics and beyond. *Advances in Physics*, 56(2):243, 2007.

[4] J.V. Porto, S.L. Rolston, B. Laburthe-Tolra, C.J. Williams, and W.D. Phillips. Quantum information with neutral atoms as qubits. *Philosophical Transactions of the Royal Society of London A: Mathematical, Physical and Engineering Sciences*, 361(1808):1417, 2003.

[5] B.J. Bloom, T.L. Nicholson, J.R. Williams, S.L. Campbell, M. Bishof, X. Zhang, W. Zhang, S.L. Bromley, and J. Ye. An optical lattice clock with accuracy and stability at the 10-18 level. *Nature*, 506(7486):71, 2014.

[6] K. Baumann, C. Guerlin, F. Brennecke, and T. Esslinger. Dicke quantum phase transition with a superfluid gas in an optical cavity. *Nature*, 464(7293):1301, 2010.

[7] A. Griessner, A. J. Daley, S. R. Clark, D. Jaksch, and P. Zoller. Dark-State Cooling of Atoms by Superfluid Immersion. *Phys. Rev. Lett.*, 97(22):220403, 2006.

[8] S. Diehl, A. Micheli, A. Kantian, B. Kraus, H. P. Büchler, and P. Zoller. Quantum states and phases in driven open quantum systems with cold atoms. *Nat. Phys.*, 4(11):878, 2008.

[9] M. Müller, S. Diehl, G. Pupillo, and P. Zoller. Engineered Open Systems and Quantum Simulations with Atoms and Ions. *Adv. At. Mol. Opt. Phys.*, 61:1–80, 2012.

[10] T. Ramos, H. Pichler, A.J. Daley, and P. Zoller. Quantum spin dimers from chiral dissipation in cold-atom chains. *Phys. Rev. Lett.*, 113:237203, 2014.

[11] C.N. Yang. η pairing and off-diagonal long-range order in a hubbard model. *Phys. Rev. Lett.*, 63:2144, 1989.

[12] J.R. Ensher, D.S. Jin, M.R. Matthews, C.E. Wieman, and E.A. Cornell. Bose-einstein condensation in a dilute gas: Measurement of energy and ground-state occupation. *Phys. Rev. Lett.*, 77:4984, 1996.

[13] K. B. Davis, M.O. Mewes, M. R. Andrews, N. J. van Druten, D. S. Durfee, D. M. Kurn, and W. Ketterle. Bose-einstein condensation in a gas of sodium atoms. *Phys. Rev. Lett.*, 75:3969, 1995.

[14] C.C. Bradley, C.A. Sackett, and R.G. Hulet. Bose-einstein condensation of lithium: Observation of limited condensate number. *Phys. Rev. Lett.*, 78:985, 1997.

[15] S. Stellmer, M.K. Tey, B. Huang, R. Grimm, and F. Schreck. Bose-einstein condensation of strontium. *Phys. Rev. Lett.*, 103:200401, 2009.

[16] T. Fukuhara, S. Sugawa, and Y. Takahashi. Bose-einstein condensation of an ytterbium isotope. *Phys. Rev. A*, 76:051604, 2007.

[17] T. Fukuhara, Y. Takasu, M. Kumakura, and Y. Takahashi. Degenerate fermi gases of ytterbium. *Phys. Rev. Lett.*, 98:030401, 2007.

[18] A. Griesmaier, J. Werner, S. Hensler, J. Stuhler, and T. Pfau. Bose-einstein condensation of chromium. *Phys. Rev. Lett.*, 94:160401, 2005.

[19] M. Lu, N.Q. Burdick, S.H. Youn, and B.L. Lev. Strongly dipolar bose-einstein condensate of dysprosium. *Phys. Rev. Lett.*, 107:190401, 2011.

[20] K. Aikawa, A. Frisch, M. Mark, S. Baier, A. Rietzler, R. Grimm, and F. Ferlaino. Bose-einstein condensation of erbium. *Phys. Rev. Lett.*, 108:210401, 2012.

[21] T.D. Cumby, R.A. Shewmon, M.G. Hu, J.D. Perreault, and D.S. Jin. Feshbach-molecule formation in a bose-fermi mixture. *Phys. Rev. A*, 87:012703, 2013.

[22] C.H. Wu, J.W. Park, P. Ahmadi, S. Will, and M.W. Zwierlein. Ultracold fermionic feshbach molecules of ^{23}Na^{40}**K**. *Phys. Rev. Lett.*, 109:085301, 2012.

[23] Y.-J. Lin, A R Perry, R L Compton, I B Spielman, and J V Porto. Rapid production of ^{87} Rb Bose-Einstein condensates in a combined magnetic and optical potential. *Phys. Rev. A*, 79(6):063631, 2009.

[24] T. Fukuhara, S. Sugawa, Y. Takasu, and Y. Takahashi. All-optical formation of quantum degenerate mixtures. *Phys. Rev. A*, 79:021601, 2009.

[25] S. Taie, Y. Takasu, S. Sugawa, R. Yamazaki, T. Tsujimoto, R. Murakami, and Y. Takahashi. Realization of a SU(2)×SU(6) system of fermions in a cold atomic gas. *Phys. Rev. Lett.*, 105(19):190401, 2010.

[26] S. Sugawa, K. Inaba, S. Taie, R. Yamazaki, M. Yamashita, and Y. Takahashi. Interaction and filling-induced quantum phases of dual mott insulators of bosons and fermions. *Nature Physics*, 7(8):642, 2011.

[27] M. Borkowski, P.S. Zuchowski, R. Ciurylo, P.S. Julienne, D. Kedziera, L. Mentel, P. Tecmer, F. Münchow, C. Bruni, and A. Görlitz. Scattering lengths in isotopologues of the RbYb system. *Phys. Rev. A*, 88:052708, 2013.

[28] M. Kitagawa, K. Enomoto, K. Kasa, Y. Takahashi, R. Ciuryło, P. Naidon, and P.S. Julienne. Two-color photoassociation spectroscopy of ytterbium atoms and the precise determinations of s-wave scattering lengths. *Phys. Rev. A*, 77:012719, 2008.

[29] E. A. Burt, R. W. Ghrist, C. J. Myatt, M. J. Holland, E. A. Cornell, and C. E. Wieman. Coherence, correlations, and collisions: What one learns about bose-einstein condensates from their decay. *Phys. Rev. Lett.*, 79:337, 1997.

[30] J. Söding, D. Guéry-Odelin, P. Desbiolles, F. Chevy, H. Inamori, and J. Dalibard. Three-body decay of a rubidium bose–einstein condensate. *Applied physics B*, 69(4):257, 1999.

[31] P.F. Bedaque, E. Braaten, and H.-W. Hammer. Three-body recombination in bose gases with large scattering length. *Phys. Rev. Lett.*, 85:908, 2000.

[32] F. Baumer, F. Münchow, A. Görlitz, S. E. Maxwell, P. S. Julienne, and E. Tiesinga. Spatial separation in a thermal mixture of ultracold ^{174}Yb and ^{87}Rb atoms. *Phys. Rev. A*, 83(4):040702, 2011.

[33] S.L. Cornish, N.R. Claussen, J.L. Roberts, E.A. Cornell, and C.E. Wieman. Stable ^{85}Rb bose-einstein condensates with widely tunable interactions. *Phys. Rev. Lett.*, 85:1795, 2000.

[34] P. Ao and S. T. Chui. Binary bose-einstein condensate mixtures in weakly and strongly segregated phases. *Phys. Rev. A*, 58:4836, 1998.

[35] John L. Bohn and P. S. Julienne. Semianalytic theory of laser-assisted resonant cold collisions. *Phys. Rev. A*, 60:414, 1999.

[36] M. Borkowski, R. Ciuryło, P. S. Julienne, S. Tojo, K. Enomoto, and Y. Takahashi. Line shapes of optical feshbach resonances near the intercombination transition of bosonic ytterbium. *Phys. Rev. A*, 80:012715, 2009.

[37] L. Viverit, C.J. Pethick, and H. Smith. Zero-temperature phase diagram of binary boson-fermion mixtures. *Phys. Rev. A*, 61:053605, 2000.

[38] R. Grimm, M. Weidemüller, and Y. B. Ovchinnikov. Optical dipole traps for neutral atoms. *Adv. At. Mol. Opt. Phys*, page 95, 1999.

[39] S. Chu, J.E. Bjorkholm, A. Ashkin, and A. Cable. Experimental observation of optically trapped atoms. *Phys. Rev. Lett.*, 57:314, 1986.

[40] T.G. Tiecke, S.D. Gensemer, A. Ludewig, and J.T.M. Walraven. High-flux two-dimensional magneto-optical-trap source for cold lithium atoms. *Phys. Rev. A*, 80(1):013409, 2009.

[41] S. Dörscher, A. Thobe, B. Hundt, A. Kochanke, R. Le Targat, P. Windpassinger, C. Becker, and K. Sengstock. Creation of quantum-degenerate gases of ytterbium in a compact 2D-/3D-magneto-optical trap setup. *Rev. Sci. Instrum.*, 84(4):043109, 2013.

[42] H.J. Metcalf and P. van der Straten. *Laser Cooling and Trapping*. 1999.

[43] Y. Castin and R. Dum. Bose-einstein condensates in time dependent traps. *Phys. Rev. Lett.*, 77:5315, 1996.

[44] C. Javaux, I.G. Hughes, G. Lochead, J. Millen, and M.P.A. Jones. Modulation-free pump-probe spectroscopy of strontium atoms. *The European Physical Journal D*, 57(2):151, 2010.

[45] C. Wieman and T.W. Hänsch. Doppler-free laser polarization spectroscopy. *Phys. Rev. Lett.*, 36:1170, 1976.

[46] J.A. Sherman, N.D. Lemke, N. Hinkley, M. Pizzocaro, R.W. Fox, A.D. Ludlow, and C.W. Oates. High-accuracy measurement of atomic polarizability in an optical lattice clock. *Phys. Rev. Lett.*, 108:153002, 2012.

[47] S.G. Porsev, A.D. Ludlow, M.M. Boyd, and J. Ye. Determination of sr properties for a high-accuracy optical clock. *Phys. Rev. A*, 78:032508, 2008.

[48] S.G. Porsev, K. Beloy, and A. Derevianko. Precision determination of electroweak coupling from atomic parity violation and implications for particle physics. *Phys. Rev. Lett.*, 102:181601, 2009.

[49] A. A. Vasilyev, I. M. Savukov, M. S. Safronova, and H. G. Berry. Measurement of the $6s - 7p$ transition probabilities in atomic cesium and a revised value for the weak charge Q_W. *Phys. Rev. A*, 66:020101, 2002.

[50] M. S. Safronova, M. G. Kozlov, and Charles W. Clark. Precision calculation of blackbody radiation shifts for optical frequency metrology. *Phys. Rev. Lett.*, 107:143006, 2011.

[51] E. Gomez, S. Aubin, L.A. Orozco, and G.D. Sprouse. Lifetime and hyperfine splitting measurements on the 7s and 6p levels in rubidium. *JOSA B*, 21(11):2058, 2004.

[52] N. Bouloufa, A. Crubellier, and O. Dulieu. Photoassociative molecular spectroscopy for atomic radiative lifetimes. *Physica Scripta*, 2009(T134):014014, 2009.

[53] B. Arora, M.S. Safronova, and Charles W. Clark. Tune-out wavelengths of alkali-metal atoms and their applications. *Phys. Rev. A*, 84:043401, 2011.

[54] U Volz and H Schmoranzer. Precision lifetime measurements on alkali atoms and on helium by beam–gas–laser spectroscopy. *Physica Scripta*, 1996(T65):48, 1996.

[55] P.L. Gould, G.A. Ruff, and David E. Pritchard. Diffraction of atoms by light: The near-resonant kapitza-dirac effect. *Phys. Rev. Lett.*, 56:827, 1986.

[56] N. Hinkley, J.A. Sherman, N.B. Phillips, M. Schioppo, N.D. Lemke, K. Beloy, M. Pizzocaro, C.W. Oates, and A.D. Ludlow. An atomic clock with 10^{-18} instability. *Science*, 341(6151):1215, 2013.

[57] G. Mura, T. Franzen, C.A. Jaoudeh, A. Görlitz, H. Luckmann, I. Ernsting, A. Nevsky, and S. Schiller. A transportable optical lattice clock using 171 yb. In *European Frequency and Time Forum & International Frequency Control Symposium (EFTF/IFC), 2013 Joint, 2013, p. 376-378.*, volume 1, page 376, 2013.

[58] M.D. Frye and J.M. Hutson. Collision cross sections for the thermalization of cold gases. *Phys. Rev. A*, 89(5):052705, 2014.